Detection of Earthflow Using a GPS and LiDAR Integrated Survey: A Case Study from the Slumgullion Landslide, Lake City, Colorado

---

A Thesis Presented to

The Faculty of the Department of Earth and Atmospheric Sciences

University of Houston

In Partial Fulfillment

of the Requirements for the Degree

Master of Science

By

Xinxiang Zhu

May 2017

Detection of Earthflow Using a GPS and LiDAR Integrated Survey:

A Case Study from the Slumgullion Landslide, Lake City, Colorado

---

Xinxiang Zhu

APPROVED:

Dr. Guoquan Wang, Chairman

Dr. Shuhab D. Khan

Dr. Hyongki Lee

Dean, College of Natural Sciences and Mathematics

Acknowledgements

I would like to express my greatest gratitude to my advisor, Dr. Guoquan Wang. Without your trust and belief in my abilities, I would not have been able to go this far as a graduate student. Thank you for giving me the opportunity to step into the world of geodesy and leading me into an interesting and valuable field. Two years of studying under your supervision have been a life changing experience for me as a graduate student. Your integrity, work ethic, and dedication will continuously motivate me throughout my life.

I also want to thank the other members of my research committee, Dr. Shuhab D. Khan, and Dr. Hyongki Lee for your patience and mentoring on me. You are the inspiration for me as a young scientist and helping me expand my knowledge and skills for geophysical studies.

Thanks to all the crew members involved in our survey at the Slumgullion landslide. Without your help, it would not have been possible for me to obtain such high-quality data for my thesis. Thanks for the support from the National Center for Airborne Laser Mapping for providing the airborne laser scanning data.

Finally, I would like to thank my parents in China. You helped me realize my dream of studying abroad and starting a new chapter of my life.

Detection of Earthflow Using a GPS and LiDAR Integrated Survey:

A Case Study from the Slumgullion Landslide, Lake City, Colorado

---

A Thesis Presented to

The Faculty of the Department of Earth and Atmospheric Sciences

University of Houston

In Partial Fulfillment

of the Requirements for the Degree

Master of Science

By

Xinxiang Zhu

May 2017

Abstract

The Slumgullion landslide in the San Juan Mountains near Lake City, Colorado has been a natural laboratory for landslide and environmental studies since the early 1900s. The landslide site covers 4.6 square kilometers and consists of an active part which has been moving continuously for about 300 years over an older, much larger, inactive part. We conducted an integrated GPS and LiDAR survey at the landslide site in one-week period from July 3rd to July 10th, 2015, with the primary purpose of delineating short-term ground deformation associated with the earthflow using advanced GPS and LiDAR techniques.

A GPS network with twelve semi-permanent stations was set up, including seven stations on the sliding mass and five stations outside the sliding mass. A RIEGL VZ-2000 terrestrial laser scanner was used to collect data in the field. Airborne laser scanning data were collected by the National Center for Airborne Laser Mapping. We compared different registration methods for datasets acquired by the terrestrial laser scanner. A rapid workflow for field surveying and data processing was developed to generate high-resolution digital terrain models. The movement of the Slumgullion landslide was derived from semi-permanent GPS observations, and two repeated terrestrial laser scanning surveys conducted during the one-week period. A 1.47 cm horizontal daily movement was detected from the GPS observations. We compared different change detection strategies for the LiDAR point clouds measurements. Lateral landslide movements were detected from cloud-to-cloud comparison using the data from terrestrial laser scanning; the accumulated motion ranged from 3 cm to 10 cm during the survey week. The movement measurements derived from GPS and the terrestrial laser scanner agreed well. Our study demonstrates a method of identifying slow earth mass movement using the integration of GPS, terrestrial, and airborne laser scanning datasets. We developed a workflow for

terrestrial laser-scanning data processing. Our method could be applied to study landslides in other regions. It is expected that our results will promote the application of GPS and LiDAR techniques in the practice of landslide hazards mitigation.

Table of Contents

List of Figures

List of Tables

1 Introduction

1.1 Geological Settings and Previous Studies

The Slumgullion landslide is located within the San Juan Mountains in southwestern Colorado (Figure 1-1). The entire landslide is 6.8 km long and has an estimated volume of 170×10^6 m^3 (Parise and Guzzi, 1992). The major portion of the landslide was formed from hydrothermally altered volcanic materials that originate at the rim of Lake City Caldera at the southern end of Mesa Seco (Lipman, 1976). The volcanic materials are from the Tertiary period. The earliest movement is estimated to be about 1,300 years ago (Madole, 1996). Approximately 700 years ago, the landslide formed a natural dam in the Gunnison River at Lake Fork, which resulted in the formation of the second largest lake in Colorado: Lake San Cristobal. The landslide has a complex history of movement and currently consists of a large area of inactive landslide deposits and a smaller area that is active. Radiocarbon ages determined on wood fragments exposed at the toe of the inactive landslide have provided an estimate of about 700 years for the overall age of movement. The active part of the landslide, based on analysis of tree rings, has an estimated age of about 300 years (Crandell and Varnes, 1960, 1961).

Fleming et al. (1999) suggested that the active part of the Slumgullion landslide had been moving at a nearly constant rate for at least 30 years. The currently active part was triggered by a collapse, which extended the preexisting head scarp toward the north, as pointed by the red arrow in Figure 1-2. In general, the upper part of the landslide is characterized by stretching features, like normal faults, and tension cracks; the lower part of the landslide is characterized by shortening and spreading features, like thrust faults; in between features are a result of widening, bending or narrowing of the landslide (Fleming et al., 1999).

The active part of the Slumgullion landslide consists of heterogeneous, yellow, sandy-silty-clay with scattered patches of bouldery debris, reddish-brown and purple clay, and pond and stream sediments (Chleborad et al., 1996). The average slope of the active part of the landslide (not including the head scarp) is about eight degrees. Streams and ponds can be found perennially or intermittently in the active part located on the surface of the landslide. Spruce and aspen trees are tilted or broken due to the activity of the landslide. It is evident that the active part contains less vegetation compared with the inactive part or the flank of the landslide, as shown in Figure 1-3. The boundary of the active landslide toe can be clearly identified from the hill shade map derived from ALS datasets, as pointed by the blue arrow in Figure 1-2. Highway 149 crosses the inactive part of the landslide, which is only 250 meters away from the lower edge of the active landslide.

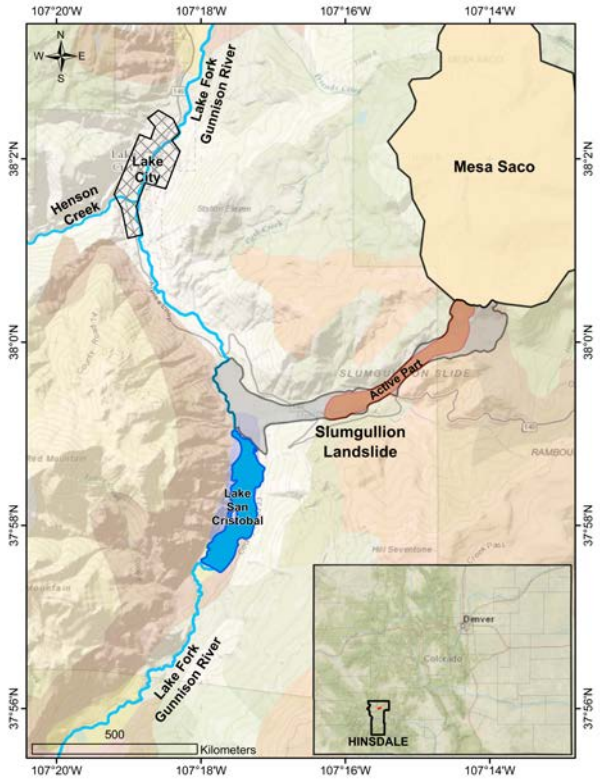

Figure 1-1 Geographic map of the Slumgullion landslide area.

Based on the categorization of the United States Geological Survey (USGS) (Fleming et al., 1999), the active part of the landslide is divided into seven zones: Zone 1 is the landslide head and the zone numbering proceeds downslope to Zone 7 as the toe of the landslide. The flanks of the landslide are defined as looking downslope to the left or right. The left flank is the south side of the landslide near the adjacent Highway 149. The airborne LiDAR data used in this study cover all parts of the active landslide, while the GPS and Terrestrial Laser Scanning (TLS) integrated survey covers the Hopper and Neck (Zone 3) and the Pull-Apart Basin along both flanks (Zone 4).

Studies of the Slumgullion landslide started in the late 1800s and continued throughout the twentieth century (e.g., Endlich, 1876; Atwood and Mather, 1932; Crandell and Varnes, 1961; Varnes and Savage, 1996b; Savage and Fleming, 1996). Modern survey technologies like GPS started in the 1990s (e.g., Jackson et al., 1993; Savage and Fleming, 1996). In 1998, the USGS began to work on the measurement of the landslide using Synthetic Aperture Radar (InSAR).

Previous studies have indicated that the most active part of the landslide is moving at 6 m annually. The velocity reaches its peak during the spring and summer, due to snow melt or summer rain; it reaches its lowest during the winter, due to low water content, which is the result of reduced precipitation and frozen soil. The correlation between surface water and landslide movement velocity is supported by long-term GPS observations (Coe et al., 2003). Note that temperature is a secondary factor that causes movement of the landslide.

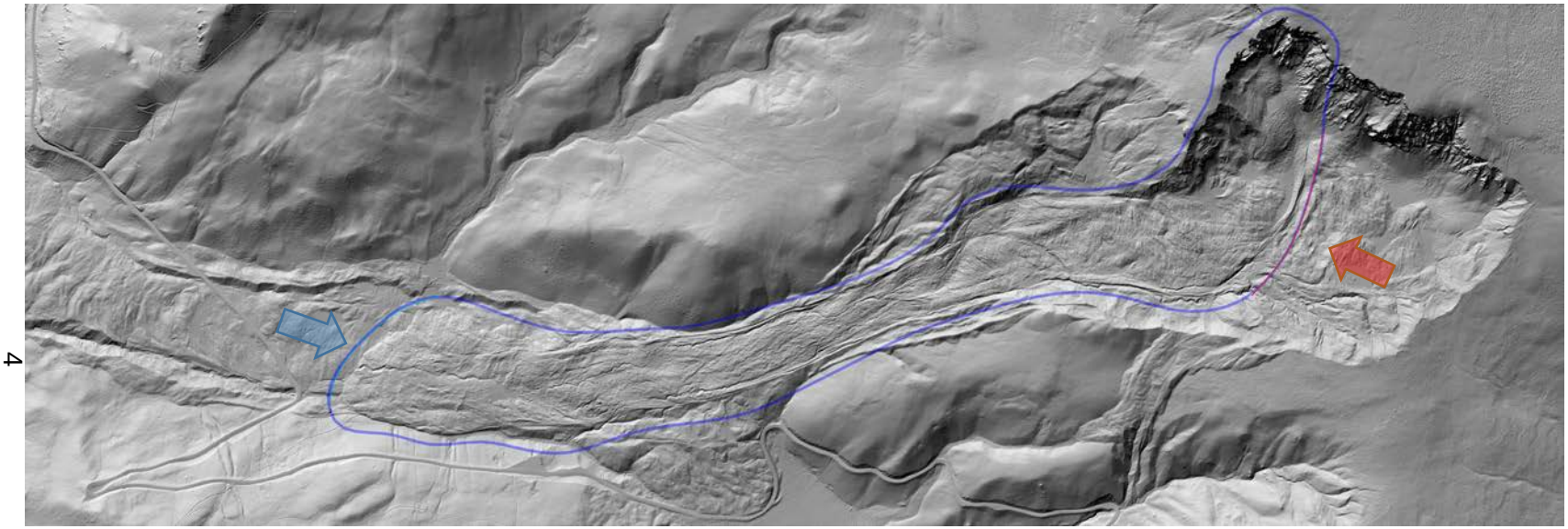

Figure 1-2 Airborne Laser Scanning (ALS) data collected from the National Center for Airborne Laser Mapping (NCALM) on July 3rd, 7th, and 10th 2015. Hill shade map taken on July 3rd shows a bird's eye view of the landslide. The meandering stripe at the bottom is Colorado State Highway 149. The detached materials slid and flowed downhill and formed a clear boundary at the active landslide toe, as pointed by the blue arrow. The blue line circles the active part that has been continuously moving for more than 30 years. A clear boundary caused by the collapse of the active head scarp can be seen, as pointed by the red arrow.

Figure 1-3 Panorama of the active part of the Slumgullion landslide. The image was taken in the middle part of the landslide, looking downwards to the landslide toe.

Previous studies of topographic changes of landslides started from 1-D grid marker surveying and progressed to using 2-D aerial photography in the twentieth century. Currently, 3-D surveying technologies such as Light Detection and Ranging (LiDAR) and Interferometric synthetic aperture radar (InSAR) are used to generate high-resolution georeferenced models for landslide studies. Equipment used includes total station, wire extensometer, GNSS system, LiDAR, Radar. Measurements can be discrete or continuous, and data can be collected from a short-term campaign or a long-term monitoring (e.g., Coe et al., 2003; Glenn et al., 2006; Wang et al., 2013).

1.2 Research Objectives and Thesis Layout

We conducted a GPS and LiDAR integrated survey for the purpose of delineating the short-term topographic changes of the Slumgullion landslide. The surveying crew members are shown in Figure 1-4.

The thesis is organized into three parts. The first part introduces the instruments and the integrated surveying we conducted at the Slumgullion landslide from July 3rd to July 10th, 2015. The second part presents our unique workflow for TLS data processing in order to generate high-resolution digital terrain models (DTMs) for the landslide area. The third part presents how we acquired the slow-landsliding motion at the active part of the Slumgullion landslide using data collected from our one-week survey.

1.3 Introduction of Surveying Instruments

This section introduces the primary surveying instruments that are used in our study including twelve Trimble GPS units, a RIEGL VZ-2000 terrestrial laser scanner, and an Optech Titan airborne laser scanner.

Figure 1-4 A group photo of crew members for the Slumgullion landslide survey.

1.3.1 GPS instruments

We used two types of Global Navigation System (GPS) units during the survey, including Trimble NetR9 GPS units and Trimble R10 GPS units. A Trimble NetR9 GPS unit has a separate receiver and antenna design. The NetR9 GNSS reference receiver is a multiple-frequency GNSS receiver. It can track all GPS (L1/L2/L5) as well as GLONASS (L1/L2) signals. As a common geodetic reference receiver, it can be used as the key component of the Continuously Operating Reference Station (CORS) or as other types of campaign receivers. Due to its internal battery, it also works well as a portable RTK base station; the built-in Lithium-ion battery can operate continuously for more than 10 hours after charging overnight. A simple screen interface is equipped at the front of the receiver for information

concerning satellite signal status, IP information and battery life. The receiver is intended for using with the Zephyr Geodetic Model 2 antenna series.

The antenna types utilized in our survey were TRM5597.00 NONE with the lead-based solder and TRM57971.00 NONE with the RoHS compliant solder. For a static GNSS survey, the precision for the NetR9 GPS unit was as is listed in Table 1-1.

Table 1-1 Positioning performance for NetR9 GPS unit (Trimble, 2010).

Static GNSS Surveying (24-hours) with baseline <30 km
Horizontal……..3 mm + 1 ppm RMS
Vertical…….4 mm + 0.4 ppm RMS
Initialization time……..Typically < 10 seconds
Initialization reliability…….Typically > 99.9%

In Table 1-1, given errors for a NetR9 GPS are 3 mm horizontally and 4 mm vertically. The reason that horizontal precision is better than vertical is that the GNSS receiver cannot receive satellite signals below the horizon; thus, there was always better satellite geometry for the horizontal than the vertical plane. One Part Per Million (PPM) means that there is a one-millimeter additional giver error for every kilometer baseline length increase. Precision or repeatability of a GPS measurement may be subject to degradation by reasons such as multipath interference, obstructions, satellite geometry, and atmospheric conditions; the accuracy of such measurements is also influenced by variables such as satellite status, reference frame, and processing method.

A Trimble R10 GPS unit has a compact design: the GNSS antenna, radio, and battery are integrated into a rugged light-weight receiver. Similar to NetR9 GPS, it can track all GPS

(L1/L2/L5) as well as GLONASS (L1/L2) signals. With its light-weight design, a pair of R10s is ideal for an RTK GPS survey. However, in this study, we used Trimble R10 GPS units as static GPS stations, with the same function as the NetR9. The performance of the Trimble R10 GPS unit for a static survey is listed in Table 1-2.

Table 1-2 Positioning performance for R10 GPS unit (Trimble, 2012).

Static GNSS Surveying (24-hours) with baseline <30 km
Horizontal……..3 mm + 0.1 ppm RMS Vertical…….3.5 mm + 0.4 ppm RMS Initialization time……..Typically < 8 seconds Initialization reliability…….Typically > 99.9%

Compared with the NetR9, the R10 GPS unit has slightly better performance in vertical direction and had a shorter initialization time. However, for our purposes, it was not necessary to distinguish one from the other, since sub-millimeter differences are negligible compared to the overall survey scale at the landslide area. Thus, for this study, we used the NetR9 and R10 GPS units interchangeably.

1.3.2 GPS satellite positioning

Various methods are used to collect high-precision GPS data, and the choice depends on the GPS specifications and the survey environment. Here we introduce the core principles of GPS satellite positioing, in order to justify our choice of the best survey strategies for our GPS survey at the Slumgullion landslide.

A basic model to determine the range from a ground receiver to a satellite will be

$$r = c \times t, \tag{1-1}$$

where r is the range measurement to the satellite, c the signal velocity, and t the elapsed time for the signal to travel from the satellite to the receiver. In order to determine the elapsed time, both the ranging signal and the navigation message are needed. For both the NetR9 and R10 systems, the ranging signal is stored in a TO2 file, which can be converted to a Receiver Independent Exchange Format (RINEX), called an Observation data file (O file). The navigation message includes the almanac data which records the status of the entire satellite constellation, and the ephemeris data which is the unique orbital information for each satellite. For the NetR9 and R10 systems, the ephemeris data is stored in the RINEX navigation data file (N file), which updates every hour or every day, depending on the post-processing requirement. Both the O file and N files are needed to calculate the range. For some positioning services, only the O file is needed, since the N file can be preloaded online.

There are two fundamental methods to determine the range from a GPS unit to a satellite: Code Ranging method, and Carrier Phase Shift method. For the Code Ranging method, the range (also called the pseudorange) measured by Receiver A is

$$\begin{aligned} R_A^j(t) &= \rho_A^j(t) + c\left[\delta^j(t) - \delta_A(t)\right] \\ \rho_A^j &= \sqrt{(X^j - X_A)^2 + (Y^j - Y_A)^2 + (Z^j - Z_A)^2}, \end{aligned} \tag{1-2}$$

where the pseudorange is $R_A^j(t)$, which is the observed distance from Receiver A to the jth satellite at the time or epoch t; and ρ_A^j is the geocentric range, which is the idea range from the satellite to the receiver under the geocentric coordinate system. The position for the jth satellite is $\left(X^j, Y^j, Z^j\right)$, which is transformed from the original satellite reference coordinate system. δ^j is the satellite-clock bias, and δ_A is the receiver-clock bias. With

four satellites $(j = 1, 2, 3, 4)$, four equations can be solved simultaneously, yielding the receiver position of A (X_A, Y_A, Z_A) and its receiver-clock bias.

For the Carrier Phase Shift method, the receiver records the phase lag between the transmitted and the received signal,

$$\Phi_A^j(t) = \frac{1}{\lambda}\rho_A^j(t) + N_A^j + f^j\left[\delta^j(t) - \delta_A^j(t)\right]$$
$$\frac{1}{\lambda}\rho_A^j(t) = \alpha + \beta, \tag{1-3}$$

where $\Phi_A^j(t)$ is the phase shift between the satellite j and Receiver A. An ideal phase shift consists of three parts: the fractional initial cycle α, the observation cycle count β, and the carrier phase ambiguity N. From the moment the receiver locks onto a satellite, α and N are constant until the receiver loses the track of that satellite. A cycle slip may cause an unstable α and N. The observation cycle count β records the consecutive full phase cycle changes throughout the observation, until the receiver loses track of the satellite. In Formula (1-3), $\frac{1}{\lambda}\rho_A^j(t)$ shows the contribution from α and β; $f^j\left[\delta^j(t) - \delta_A^j(t)\right]$ shows the phase change caused by the clock bias from the satellite and receiver; and f^j is the frequency of the broadcast signal generated from the satellite.

Typical errors of satellite positioning stem from the following: (1) satellite and receiver clock biases; (2) ionospheric and tropospheric refraction; (3) satellite ephemeris error; (4) signal multipathing; (5) antenna miscentered; (6) antenna height measurement error; and (7) satellite geometric dilution of precision. Differential GPS positioning methods are used to mitigate some of these errors.

In differential GPS positioning (DGPS), ranging errors determined from one GPS were able to be used to correct ranging errors of another GPS located nearby. The objective of

relative positioning is to obtain the baseline vector which describes the coordinates of one point relative to another. For example, the baseline vector Δ from Receiver A to Receiver B can be expressed as

$$\begin{aligned} X_B &= X_A + \Delta X \\ Y_B &= Y_A + \Delta Y \\ Z_B &= Z_A + \Delta Z, \end{aligned} \tag{1-4}$$

where (X_A, Y_A, Z_A) is the geocentric coordinate at Station A, (X_B, Y_B, Z_B) the geocentric coordinate at Station B, and $(\Delta X, \Delta Y, \Delta Z)$ the baseline vector. Differential GPS positioning requires GPS units collecting data simultaneously. Common recording intervals (also called epoch rates) are 1, 5, and 15 seconds. Differential GPS positioning can be subdivided into single differencing, double differencing, and triple differencing, depending on the number of satellites and the epochs of observations involved (Hofmann et al., 2001).

For single differencing, one satellite is tracked by two GPS units simultaneously at different locations. The distance between them is called a baseline. The phase shift measurements of Station A and Station B can be expressed as

$$\begin{aligned} \Phi_A^j(t) &= \frac{1}{\lambda}\rho_A^j(t) + N_A^j + f^j\left[\delta^j(t) - \delta_A^j(t)\right] \\ \Phi_B^j(t) &= \tfrac{1}{\lambda}\rho_B^j(t) + N_B^j + f^j\left[\delta^j(t) - \delta_B^j(t)\right]. \end{aligned} \tag{1-5}$$

The difference of Equation (1-5) yields

$$\begin{aligned} &\Phi_{AB}^j(t) = \tfrac{1}{\lambda}\rho_{AB}^j(t) + N_{AB}^j - f^j\delta_{AB}^j(t), \\ &\text{where } \Phi_{AB}^j(t) = \Phi_B^j(t) - \Phi_A^j(t), \qquad \rho_{AB}^j(t) = \rho_B^j(t) - \rho_A^j(t), \\ &N_{AB}^j = N_B^j - N_A^j,\ \delta_{AB}^j(t) = \delta_B^j(t) - \delta_A^j(t). \end{aligned} \tag{1-6}$$

Equation (1-6 proofs that single differencing method eliminates the error caused by the satellite-clock bias.

For double differencing, two single differencing results from two satellites, j and k, are used, which can be expressed as

$$\begin{aligned}\Phi_{AB}^{j}(t) &= \frac{1}{\lambda}\rho_{AB}^{j}(t) + N_{AB}^{j} - f^{j}\delta_{AB}^{j}(t) \\ \Phi_{AB}^{k}(t) &= \frac{1}{\lambda}\rho_{AB}^{k}(t) + N_{AB}^{k} - f^{k}\delta_{AB}^{k}(t).\end{aligned} \tag{1-7}$$

The difference of Equation (1-7 yields

$$\begin{aligned}&\Phi_{AB}^{jk}(t) = \frac{1}{\lambda}\rho_{AB}^{jk}(t) + N_{AB}^{jk}, \\ &\text{where } \Phi_{AB}^{jk}(t) = \Phi_{AB}^{k}(t) - \Phi_{AB}^{j}(t),\ \rho_{AB}^{jk}(t) = \rho_{AB}^{k}(t) - \rho_{AB}^{j}(t), \\ &N_{AB}^{jk} = N_{AB}^{k} - N_{AB}^{j}.\end{aligned} \tag{1-8}$$

Equation (1-8 proofs that double differencing method eliminates the error caused by the satellite-clock bias and the receiver-clock bias.

Similar to double differencing, triple differencing takes two double differencing results acquired at different observation times; these can be expressed as

$$\begin{aligned}\Phi_{AB}^{jk}(t_1) &= \frac{1}{\lambda}\rho_{AB}^{jk}(t_1) + N_{AB}^{jk} \\ \Phi_{AB}^{jk}(t_2) &= \frac{1}{\lambda}\rho_{AB}^{jk}(t_2) + N_{AB}^{jk}.\end{aligned} \tag{1-9}$$

The difference of Equation (1-9 yields

$$\Phi_{AB}^{jk}(t_{12}) = \Phi_{AB}^{jk}(t_2) - \Phi_{AB}^{jk}(t_1) = \frac{1}{\lambda}\rho_{AB}^{jk}(t_2) - \frac{1}{\lambda}\rho_{AB}^{jk}(t_1). \tag{1-10}$$

Here only the difference of α and β are left. The ambiguities are eliminated; thus, this method is immune to cycle slips.

Double differencing method is used by the Online Positioning User Service (OPUS) and Topcon Tools which are two of the GPS processing software packages that we utilized for this study.

1.3.3 LiDAR instruments

Both terrestrial laser scanning and airborne laser scanning were utilized in this study to delineate the movement of the Slumgullion landslide. Here we present two common ranging method used by modern LiDAR systems and several platforms that can be used to equip a LiDAR system.

The terrestrial laser scanner (TLS) used in our survey is a V-Line 3D TLS RIEGL VZ-2000 from RIEGL company. The TLS is characterized by an extremely highly effective measurement rate, offering up to 400k measurements per second and up to 240 scan line measurements per second. The scanner provides extremely long-range measurements of more than two thousand meters to the natural surface, while still maintaining completely eye safe operation (RIEGL, 2015). The airborne laser scanner used in our study was an Optech Titan ALS. The Optech Titan model is capable of providing laser pulse rates up to 300 kHz. The ALS survey is performed by the National Center for Airborne Laser Mapping (NCALM, http://ncalm.cive.uh.edu).

The history of using laser range measurements can be traced back to the mid to late 1960s. With the development of eye-safe low power laser, the ground-based laser profiler was invented. Together with the progress in data processing and GPS/IMU systems, modern terrestrial laser scanners have been developed and are being used for topographic mapping applications (Figure 1-5).

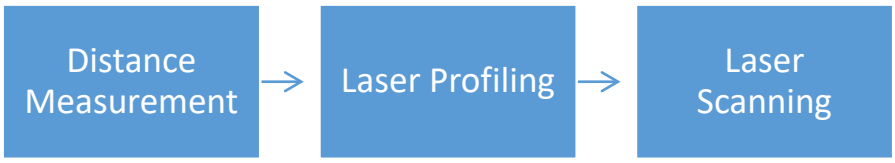

Figure 1-5 Development of Laser Scanning.

There are two major types of methods that are used to measure the distance within a LiDAR system. The first method measures the Time-of-Flight (ToF) of an intense laser pulse that travels from the transmitter to the target and then returns back to the instrument. Both the TLS and ALS used in our study belong to this ToF model. Each returned laser pulse is called an echo of the laser source. With a constant speed of light, the precision of the LiDAR system is determined by the precision of the time measurement. The range calculated from a ToF model is shown in Equation 1-11:

$$R = v \times t/2. \tag{1-11}$$

The second method of LiDAR ranging determines the distance by a phase-shift measurement. Similar to phase-shift GPS ranging, a continuous laser beam is generated, and the distance is determined by comparing the phase-shift between the transmitted and received laser signals. The total range is the solution to the simultaneous equations with at least two different carrier frequencies:

$$R = \frac{[M_n + (\varphi_n/2\pi)] \times \lambda_n}{2}, n = 1, 2, \ldots, \tag{1-12}$$

where n is the number of different carrier frequencies, M the ambiguity, φ the fractional part of phase-shift, and λ the wavelength of the modulated laser signal.

Parallel to ranging methods, another classification of LiDAR lies in the platform that carries the LiDAR instrument. Generally speaking, a LiDAR system can be equipped on a ground platform, in an aircraft, or collocated with a satellite. Both ground-based LiDAR and airborne LiDAR were used for our survey. The difference between the two is discussed below.

Ground-based LiDAR can be subdivided into tripod-based LiDAR and mobile LiDAR. The tripod-based LiDAR is unique for its static scanning mode that the platform is fixed while the LiDAR performs a scan. A stable tripod was set up to hold the LiDAR while it collected the data during our survey. The position of the LiDAR and part of its triaxial rotation are fixed (e.g., for a leveled mount the row and pitch are fixed, and for a tilted mount the yaw is fixed). A mobile LiDAR is a laser system equipped on a car; it is utilized for navigation, collision avoidance, and vehicle-based mapping.

Airborne LiDAR can be subdivided into UAV-based LiDAR, helicopter-based LiDAR, and airplane-based LiDAR. They have similar navigation systems, recording a platform's position, its triaxial rotation, and acceleration. The mobility of the platform decreases while the flight height increases. The most common scan pattern used by an airborne LiDAR is the cross-track pattern, where the scan line is perpendicular to the flight direction. Other scan patterns include the elliptical scan pattern and the parallel line pattern.

The satellite-based LiDAR system is rarely used for mapping purposes. The exception is the Ice, Cloud, and Land Elevation Satellite (ICESat). ICESat 1 and 2 are designed for the purpose of measuring the changes in ice-sheet elevation, sea-ice freeboard, and vegetation height. Most satellite-based laser systems are atmospheric LiDAR, which can be used for atmospheric profiling (Shan and Toth, 2008).

Unlike radar systems, LiDAR uses a single measure cycle. This means a traditional LiDAR system waits for the echo of the previous pulse being received before it emits a new pulse. Because of this single measure cycle, lower laser-pulse repetition frequency is used for further targets. However, if the target is too far, yet with intense reflection, it will cause aliasing, in which a fake illusion will be recorded near the scanner floating in the air. The

fake illusion is the echo of the previous pulse that comes after the transmitter fires a new pulse.

Modern LiDAR systems allows multiple pulses transmitting in the air simultaneously, and this condition is called multiple time around or MTA. Novel technologies are being developed to correlate echoes with the correctly transmitted pulse under the MTA condition (e.g., the RIEGL MTA Tool). Such techniques can mitigate the problem, but MTA aliasing still exists, especially for the long-distance and high-speed LiDAR system.

For the TLS survey conducted at the Slumgullion landslide, a 1800 m scan program was used to collect laser echoes from targets as far as 1800 m from the scanner. Targets that were more than 1800 m away might generate MTA aliasing in the TLS datasets. Figure 1-6 shows the MTA aliasing in a TLS scan acquired on July 3rd, 2015.

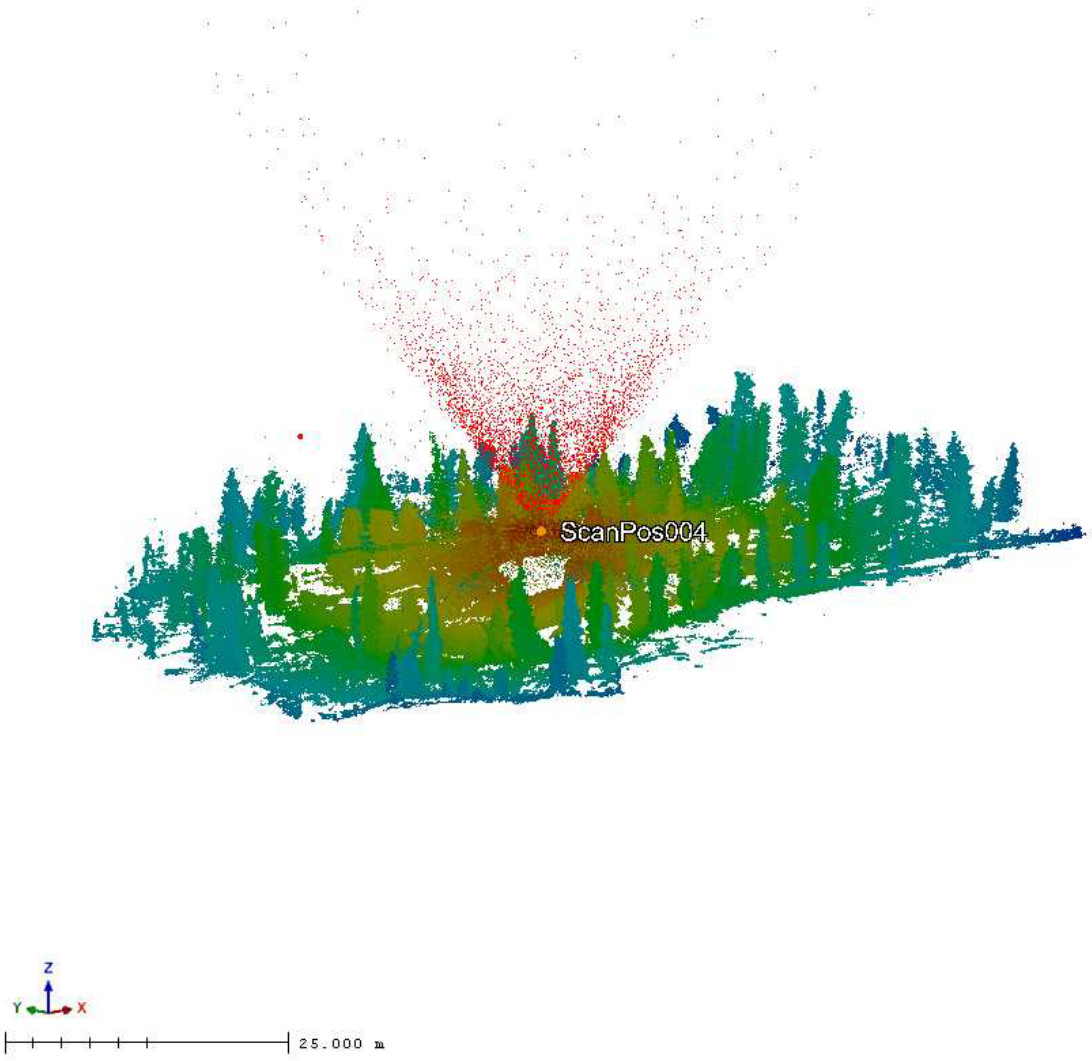

Figure 1-6 Multi Time Around (MTA) aliasing looks like an upside-down cone floating above the TLS scanner.

The laser output power for different LiDAR systems varies significantly. The energy or power levels encountered depend on the ranging methods and the platform that carries the system. The ToF LiDAR system requires a laser signal to behave like a laser pulse, whereas the phase-shift LiDAR system requires a Continuous Wave (CW) signal. Generally speaking, CW laser or phase measurement LiDAR has a lower power output,

which also limits its detection range. The ToF laser system emits a pulse with higher output power and shorter pulse duration in order to get a stronger detectable pulse peak. With higher output energy, the ToF laser can detect distant targets; thus, it is commonly used on aircraft or spacecraft-based laser systems. For ground-based LiDAR, both the ToF system and the CW system are applicable.

Based on the output power, lasers are divided into four categories based on their dangers to human eyes and skin. For most of the ground-based LiDAR, Class 1 Laser was used, as it does not emit radiation at known hazard levels. There are two spectrum bands used for LiDAR: the near infrared band is the most common one, and the green band is used for bathymetric mapping. The TLS and ALS scanner employed in our study had a Class 1 near infrared laser transmitter.

1.3.4 Scan mechanism of ALS and TLS

In this subsection, we present the scan mechanism of ALS and TLS systems which help us conduct further processing of LiDAR datasets. The general setup of a topographical ALS consists of two parts: the airborne segment and the ground segment. The airborne segment includes the airplane, the LiDAR instrument and the Position and Orientation System (POS); the ground segment includes the ground Global Navigation Satellite System (GNSS) reference stations, and the processing hardware and software for data synchronization and registration.

General topographical TLS is set up on the ground. The laser scanner is set up on a leveled tripod with the internal Position and Orientation System (POS); a collocated camera and an external GNSS are optional, equipped coaxially on top of the scanner. As part of the TLS framework, big cylinders with high-laser reflection are set up on leveled tripods around the scanner between different scanning locations; the collocated GNSS

unit is optional for each cylinder. Such cylinders have extreme high-laser backscattering, called reflectors. They are used to ‘montage’ scan results taken from adjacent locations. Most of the reflectors are captured by the scans taken at multiple locations; thus, they earn the name tie points or common points between the scan positions. The process of montaging is called registration.

Both the ALS and TLS used in our study had similar LiDAR scan mechanisms, in which the laser pulse was generated by the transmitter and spread by a continuously spinning optical polygon. The difference lay in the platform that carried the LiDAR system. For the ALS, an airplane carried the LiDAR; the laser pulses were spread out across the flight direction, forming a series of parallel lines measured over the ground. Such a scanning mechanism is called a cross-track scan. For the TLS, the optical head rotates in a horizontal plane, while the rotating polygon inside the optical head spreads the laser pulses in the vertical direction. The combination of a wide-angle vertical scan and a 360-degree horizontal scan is called a TLS panorama scan.

The speed at which laser pulses spread is determined by the angular speed of the rotating polygon and the platform moving speed, which, for ALS, is the airplane speed, and for TLS, is the optical head rotation speed. Both the polygon rotating speed and the platform moving speed contribute to the scan frequency. The scanning speed is determined by the laser’s transmitted speed and the range to the object. For the purpose of avoiding MTA aliasing, we chose lower-scan frequency for long-range scanning. In our study, the ALS had a 70-kHz scan frequency, with an average fly height of 1000 m for the Optech Titan scanner; the TLS had a 100-kHz scan frequency, with the longest detection range of 1800 m for the RIEGL VZ-2000 scanner.

A V-Line 3D-Terrestrial Laser Scanner RIEGL VZ-2000 was used for our study. The TLS scanner stores its raw data in its Scanner's Own Coordinate System (SOCS). Usually, two data sets are contained including the geometry information and the additional descriptions for every laser measurement. The geometry information is collected from the scanner and determined by the scan mechanism. The scan mechanism comprises a fast rotation polygon mirror which guides the laser beam as it moves up and down, and a slower rotating optical head which guides the laser beam as it moves on a leveled plane. The rotating polygon mirror deflects the laser beam in different directions, where consecutive measurements are collected. Measurements collected from a single mirror facet are called a scan line.

The scan line is characterized by the polar angle θ with up as zenith direction in a standard spherical coordinate located concentrically with the scanner. Only part of the mirror facets can be used for measurement ($\theta \in (30°, 130°)$), where the measurements made at the edges of the facets are ignored. While the mirror is rotating, the optical head carries and moves the whole line scan mechanism horizontally; this is called the frame scan. The frame angle is recorded as azimuthal angle φ, where the scanner's connector field is the referenced origin vector. This formed a right-handed coordinate system with counterclockwise direction as positive. A full frame scan is called a panorama scan with the frame angle covering a full circle ($\varphi \in (0°, 360°)$). Together with the range measurement r, calculated from the travel time for the ToF system, the geometric information of an echo is recorded by its scan line angle θ and frame angle φ. The scanner records the slant range by the laser rangefinder; two associated angles are recorded by two angular encoders.

Range and angle measurements are recorded in a spherical coordinate system and can be transformed into a Cartesian coordinate. For the Cartesian SOCS, the x-axis is always towards the scanner's connector field; the z-axis is the vertical rotation axis of the frame scan with up as positive direction; all X-, Y- and Z- axes are fixed with the stationary part of the scanner. The accuracy and resolution of the range and angle measurement provided by our VZ-2000 scanner is listed in Table 1-3.

Table 1-3 Range and angular measurement resolution for VZ-2000 TLS (RIEGL, 2015).

Line scan resolution (θ)	0.0015˚
Frame scan resolution (φ)	0.0005˚
Range measurement accuracy① (r)	8 mm
① One sigma at 150-meter range, under RIEGL test conditions.	

The transformation between the spherical coordinates and Cartesian coordinates is shown below:

$$\begin{aligned} x &= r \sin\theta \cos\varphi \\ y &= r \sin\theta \sin\varphi \\ z &= r \cos\theta . \end{aligned} \tag{1-13}$$

The inclination sensors were able to measure the tilt angles between the scanner's plane and a horizontal plane. A compass was integrated within the scanner so that scanner coordinate could be transformed into a east-north-up (ENU) coordinate. For ALS, EN-down (END) coordinate was used originally, resulting in a positive z-coordinate.

1.4 Survey Strategies for the Landslide Area

During the summer months of 2015, we conducted a GPS and LiDAR integrated survey at the Slumgullion landslide. The whole survey lasted from July 3rd to 10th. TLS, ALS and airborne-SAR data were collected simultaneously on July 3rd, 7th and 10th. GPS data were collected on July 3rd, 5th, 7th, 8th, and 10th. In this section, we present the GPS and LiDAR integrated survey that we conducted at the Slumgullion landslide area, including survey planning and survey method for each instrument. Such surveying methods can be used to study similar landslide at other regions.

1.4.1 GPS survey planning

A GPS network with twelve semi-permanent stations was set up, including seven stations on the sliding mass, called rover stations, and five stations outside the sliding mass, called reference stations. The goals of the GPS survey were 1) georeferencing point clouds from the TLS survey; and 2) monitoring the short-term movement of the Slumgullion landslide.

For the purpose of delineating landslide movements, we were able to conduct two types of GPS survey, considering our limited equipment. Firstly, in order to get the position of the reference stations located outside the landslide, a static GPS survey was carried out. During the static GPS survey, positions of GPS units located outside the landslide were caculated referring to the Continuously Operating Reference Stations (CORS) setup by the National Geodetic Survey (NGS). CORS achieve a higher level of accuracy ephemerides data; thus, they were used as the control stations for our project. Processed by PAGES static software, the position of a GPS unit was averaged from three independent, single-baseline solutions, each computed by double-differenced, carrier-phase measurements from one of three nearby CORS. The static survey for the reference stations required a continuous measurement that lasted for more than 2 h. Post-processed

by OPUS, a standard NGS OPUS Solution Report was generated. The initial coordinate was in IGS08 geocentric coordinates, and it was transformed into NAD83 datum by OPUS to minimize the plate motions associated with the North American Plate.

Secondly, a relative positioning was performed to determine the rovers' positions relative to the reference station. The Topcon Tools software package was used to calculate the rovers' relative coordinates. Relative positioning was able to provide a baseline vector accuracy under 5 mm horizontally and 15 mm vertically for an observation over one-hour, with a baseline of a few kilometers (Wang, 2011). With the well-known reference station's position and navigation files, the geocentric coordinates could be calculated. However, the accuracy of the coordinates was no better than the static solution relying on the NGS CORS. Figure 1-7 shows how our GPS network monitors the landslide movement.

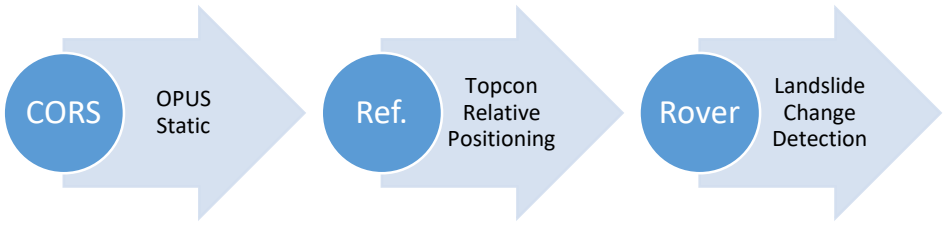

Figure 1-7 Monitoring landslide movements using a GPS network.

Many factors affect the ultimate success of a GPS survey. Factors to consider when planning a survey include: (1) required accuracy of the positioning; (2) intended use of the survey; (3) GPS equipment type and amount; (4) survey project size; (5) survey environment especially canopy conditions; and (6) available software or processing methods. Field reconnaissance is always optional but preferred when conducting a GPS survey. There should be a field reconnaissance before the survey; however, due to our limited schedule, our pre-survey site visit was combined with the first day's data collection.

1.4.2 In situ GPS units setup

General set up of an in situ tripod based GPS station consisted of a GPS antenna, a receiver, a Threaded Neil-Concelman (TNC) antenna cable, and a two-meter high survey tripod. A reflector and its adapter were optional for each GPS station that worked as a tie point for the TLS survey. Because of R10's compact design, the antenna and receiver were combined, so no external cable was needed. For the Trimble NetR9 GPS unit, shown in Figure 1-8 (a), an Ethernet cable was required to connect the receiver to the fieldwork laptop which enabled/disabled the receiver and downloaded the data. For the Trimble R10 GPS unit, shown in Figure 1-8 (b), Bluetooth connection was supported, so any cell phone or iPad that had a Bluetooth connection could be used to enable/disable the receiver; data were downloaded via Bluetooth directly to the laptop.

The GPS network we set up consisted of twelve semi-permanent stations, including seven stations on the sliding mass and five stations outside the sliding mass. There were seven rovers set up on the landslide to monitor its different parts. The GPS units were spread out along the active part of the landslide, parallel to its left flank ridge. Seven GPS units were labeled as Landslide 0 to 6 (L0-L6), going from lower to higher elevation. Five reference GPS stations were set up outside the landslide on its boundary. Three of these were located on the left flank at the stable side of the shear zones. The other two were located on the right side of the landslide on the mountain Mesa Seco. Labeling for each station corresponded to its location and height. Stations were named Ridge Low and High (RL, RH), Mountain Low and High (ML, MH), and Base Station (BA). All reference stations worked as tie points for the TLS survey. The baseline between the reference and the rover stations was extremely short, less than one kilometer.

Reference stations and rovers collected data simultaneously for more than 4 h every day. Each GPS unit was tied to a particular tripod to minimize instrument difference error. Shown in Figure 1-8 (c, d), the tripods and GPS adapters were left on the landslide with fixed locations, while the GPS units were brought back to the hotel for data downloading and battery charging after each survey day.

Figure 1-8 Field setup of GPS units. (a) a Trimble NetR9 GPS unit associated with a TLS big cylinder reflector; (b) a Trimble R10 GPS unit associated with a TLS small cylinder reflector; (c) a Trimble NetR9 GPS unit associated with a TLS small cylinder; the plastic bag on the ground contains the receiver and the yellow cable is the TNC antenna cable; (d) the adapter between the antenna and reflector.

Based on the GPS survey planning mentioned in subsection 1.4.1, the location of each GPS station was carefully selected to avoid canopy occlusion and multi-signal reflectance. All tripods were extended to their maximum height to minimize signal blocking from vegetation and to maximize visibility from each TLS scan location. There were no strong reflecting surfaces that could cause GPS signal multipathing or any manmade electrical installations that could cause signal interference. The R10 GPS units were occupied if the TLS survey was being performed simultaneously. Because our survey results were also used for georeferencing the TLS survey, locations of the GPS units were carefully selected to maximize their visibility from the nearby TLS scan positions. Figure 1-9 shows the rough location of each station located at the landslide area.

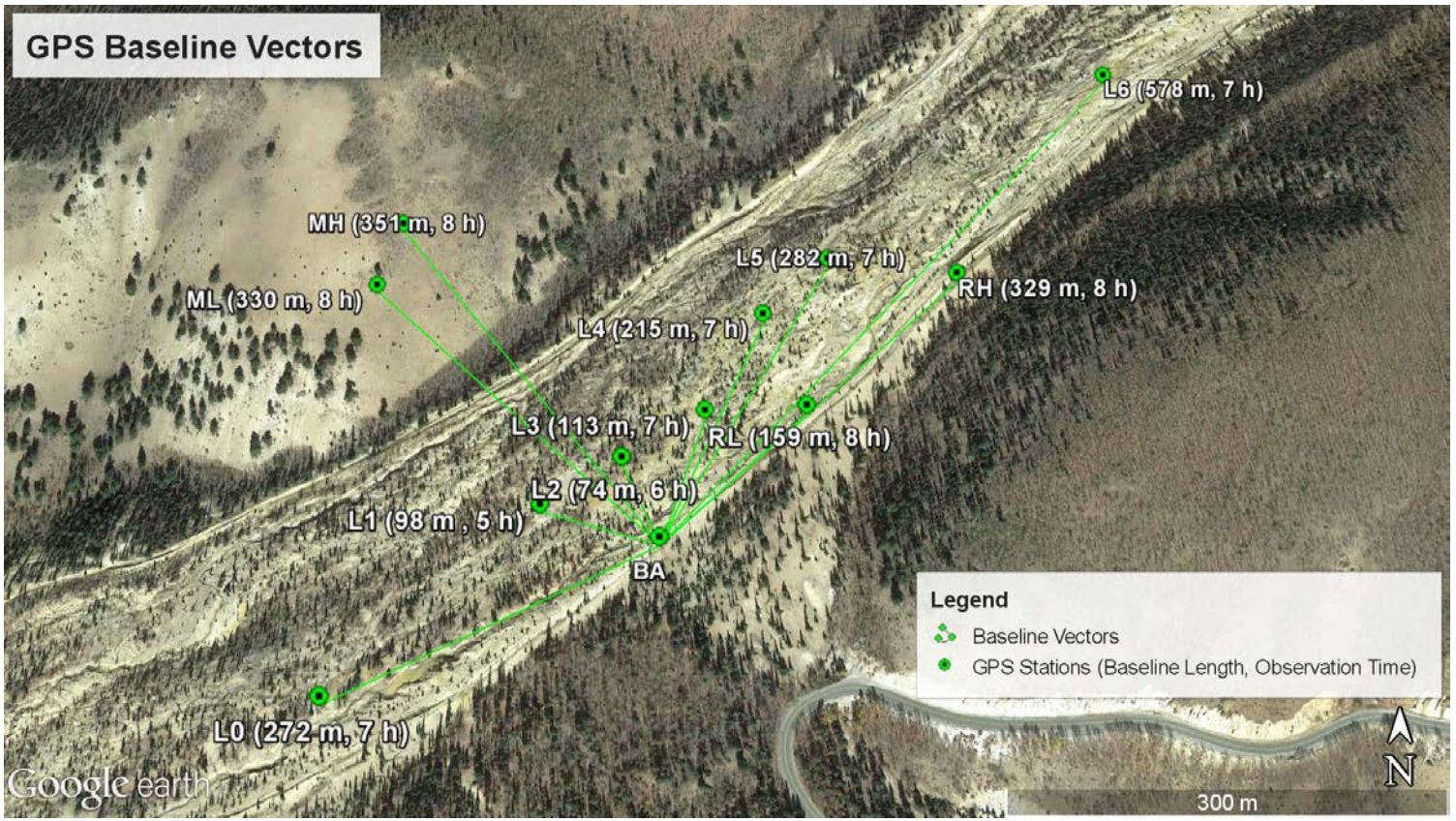

Figure 1-9 Google Earth view of all GPS stations. Five reference stations were located outside the landslide, including the base station (BA) located at the entrance to the nearest ground access from Highway 149, two on the left flank ridge (Ridge Low, Ridge High), and two on the mountain side (Mountain Low, Mountain High). Seven rover stations were located inside landslide area, running from L0 to L6 (Landslide 0, 1, 2…6).

1.4.3 GPS survey for the Slumgullion landslide

On the survey day, the base station (BA) was first set up, and then some team members set up the four GPS reference stations (RL, RH, ML, MH) on the boundary of the landslide; other team members worked on the set up of the landslide monitoring GPS (L0-L6). BA was set up at the very beginning of the survey and disabled at the end of each day; its observation window was the longest, and usually exceeded 8 hours; it was designed to introduce local CORS positioning into the GPS network we set up. Four other reference GPS units located on the boundary were used to verify the stability of BA. Figure 1-10 (a) shows the occupation timetable for all GPS units; Figure 1-10 (b) show a zoomed-in view for one GPS unit. At least four visible satellites were required for GPS positioning.

The recording interval for all GPS stations was set as one second, which means each receiver recorded satellite data every second. The tripod was reinforced with sandbags. The cable and receiver for NetR9 were protected with a water-repellent plastic bag. On July 3rd, due to inadequate preparation, several GPS units failed to record data because of instrument and operation problems; for this date, only three stations (BA, RL, and L1) have valid data records, as can be seen in Figure 1-10. The surveys on July 5th and 8th were designed for only GPS measurement. The surveys on July 3rd, 7th, and 10th were carried out as an integrated GPS and TLS survey where all the reference stations(BA, RL, RH, ML, MH) and part of the landslide monitoring stations were surveyed.

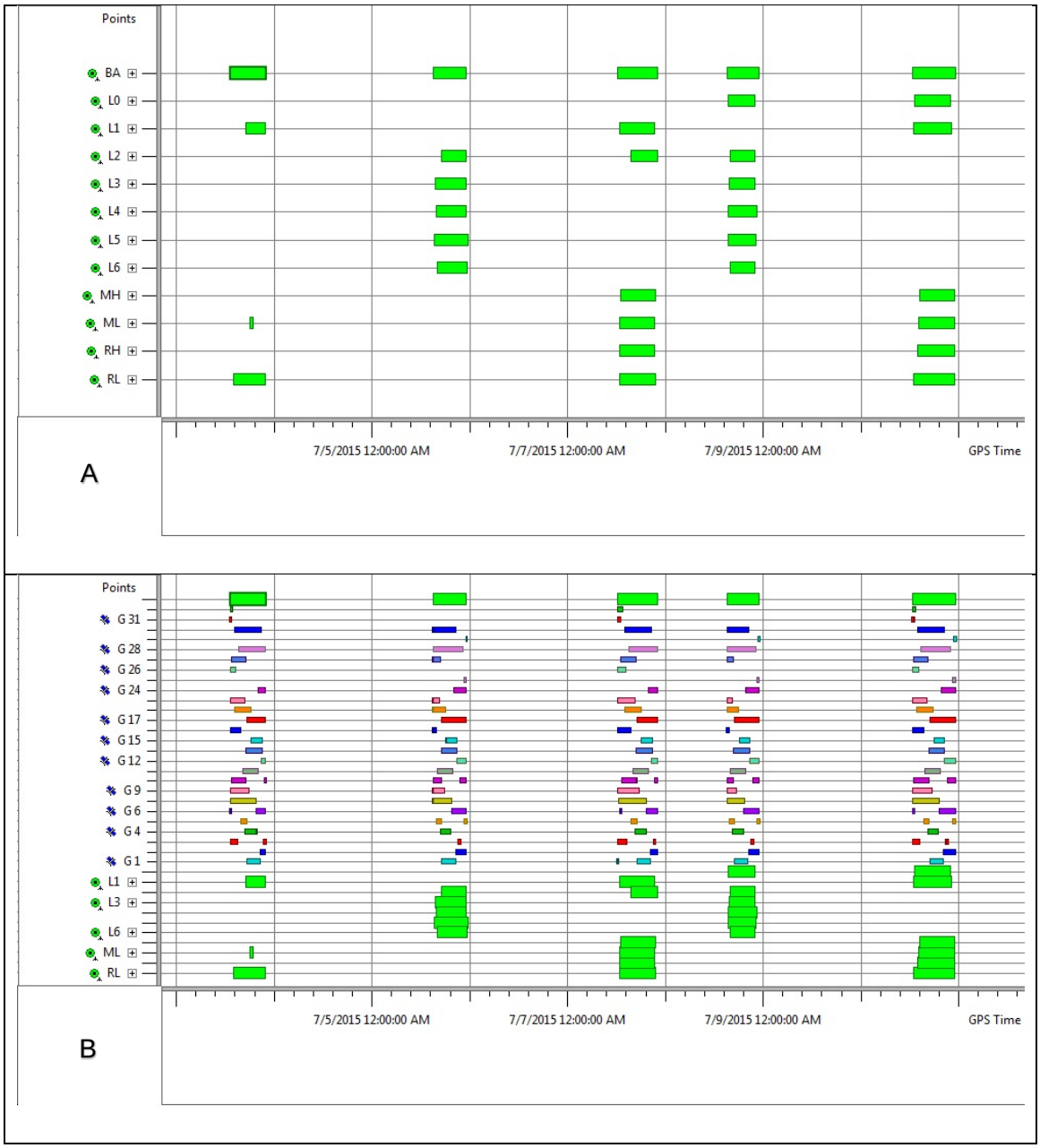

Figure 1-10 GPS occupation timetable. (a) the observation windows for all GPS units; the x-axis is GPS time; (b) a zoomed-in view for one GPS unit; different colors represent data from various satellites.

For BA, a static relative positioning was carried out referring its position to three nearby CORS. Location and distance to each CORS from BA are listed in Table 1-4.

Table 1-4 Three CORS stations used by OPUS for calculating the coordinates of the base station (BA). The distance records the baseline length between the CORS and BA.

PID Designation	Latitude	Longitude	Distance (m)
DO2634 CTI4 COMPASSTOOLS4CRNR CORS ARP	N37˚09'10.489"	W107˚45'21.876"	103017.9
DL3478 R301 CRAWFORD CORS ARP	N38˚39'23.739"	W107˚35'27.367"	79512.8
DL3642 MC09 NUCLA CORS ARP	N38˚14'35.614"	W108˚33'29.283"	117611.8

For the other reference stations (RL, RH, ML, MH), relative positioning was carried out referring to both BA and the CORS. The measurements referring to CORS were carried out to verify the stability of BA for the whole survey period. Detailed results of our GPS survey are given in Chapter 3, section 3.1.

1.4.4 TLS survey planning

The TLS surveys were conducted on July 3rd, 7th, and 10th, for the purpose of delineating ground deformation at the active part of the Slumgullion landslide. After setting up all the reference GPS stations and rover stations, the TLS survey was conducted. To cover the active part of the Slumgullion landslide, a series of scans were conducted. The complete coverage of the landsliding area could only be guaranteed if data collection was completed from different viewpoints. The location of each scan was called a Scan Position (SP), and all SPs finished in one day were stored as one TLS project. The change of the landslide

is delineated by differencing repeated TLS projects. Overall, there are three projects collected from our one-week survey. Each project contains a series of SPs, as listed in Table 1-5.

Table 1-5 TLS projects timeline

TLS Project	Date	Number of Scan Positions
1	07/03/2015	7
2	07/07/2015	8
3	07/10/2015	9

The SPs were chosen carefully to maximize their coverage along the active part of the landslide. Ideally, the maximum detection range for TLS can be 1800 m. Therefore, one SP should have been enough to have a good cover on the neck part of the landslide, which is under 200 meters. However, due to the occlusion of the laser pulse, multiple scans at different sites were often needed.

Figure 1-11 shows the ViewShed analysis provided by the ArcMap software package. It was used to estimate data coverage taken from multiple SPs. The estimation took into account that the rolling terrain would block the laser beams, but the occlusion from vegetation and other causes was not considered. The input for ViewShed analysis required an elevation model of the estimated area, the observer's height and object height, the azimuth angle, the vertical angle and the radius of the range of estimation. In our study, the elevation model was derived from the airborne LiDAR; the observation height for TLS was 2 m; the object height was zero, as the ground surface; the azimuth angle was 360˚ for the panorama scan pattern; the vertical angle was from 30˚ to 130˚ (zero as zenith); and the radius of estimation was from 0 to 1800 meters. After overlap with the point cloud collected by TLS, the ViewShed analysis agreed well with real TLS point cloud.

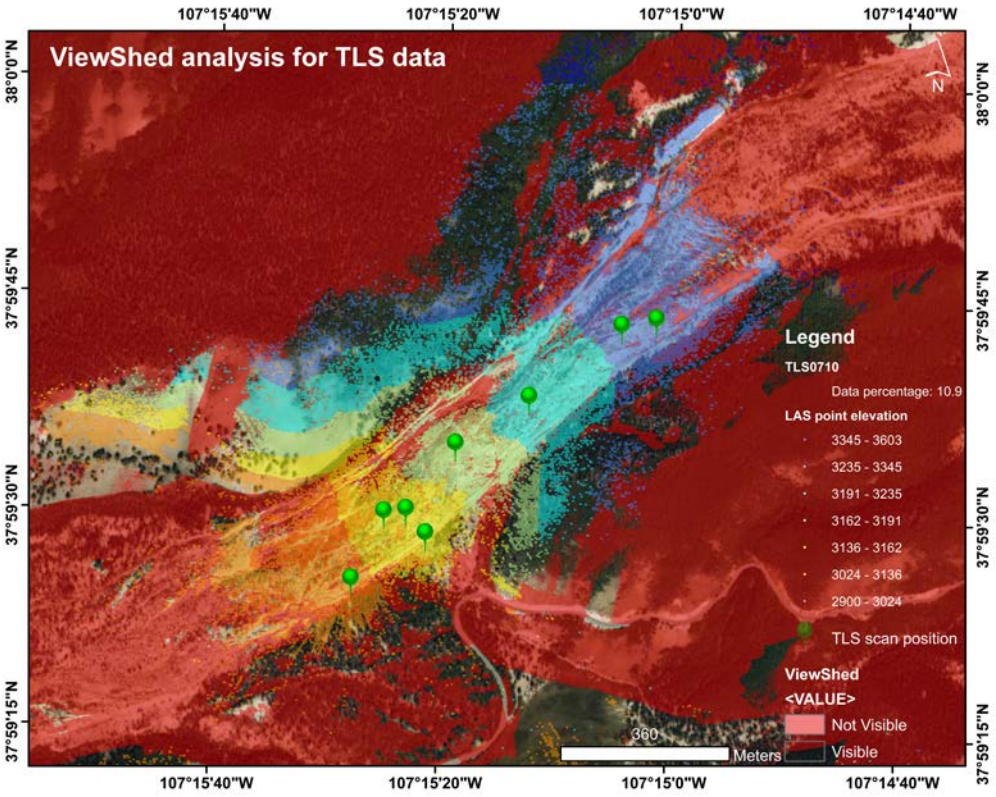

Figure 1-11 ViewShed analysis for the TLS data collected on July 10th, 2015. Red areas show topographic occlusion for the TLS scanner.

1.4.5 Occlusion pattern and resolution of LiDAR

Here we present the occlusion pattern and the temporal resolution of LiDAR measurements which are important for processing LiDAR data collected from a complex natural environment.

No matter how collimated a laser source beam is, it will spread and illuminate a circular area when it reaches a target in the distance. The illuminated area's shape is determined by the original shape of the laser and the surface of the target. The area of illumination is determined by the range from the TLS to the target. For a given angular beam spread, the greater the range, the larger the diameter of the area illuminated by a laser pulse. The

area illuminated by the laser that shoots perpendicularly towards a target is defined by the formula:

$$A = \pi \left(\frac{\theta R + d}{2}\right)^2, \quad (1\text{-}14)$$

where A is the area, θ the beam divergence angle in radians, R the range, and d the diameter of the aperture; θ is in the unit of milliradian (mrad). In our study, the TLS had a 0.3 mrad beam divergence, which corresponds to a beam diameter increase of 30 mm per 100 m range increase, and the beam diameter (aperture diameter) was $d = 7mm$. For ALS, the beam divergence was 0.5 mrad. If a 10 cm resolution is expected from TLS, then the range should be shorter than 310 m, which yields the diameter of the beam equal to 10 cm (i.e. $\theta R + d = 10\ cm$). For the Slumgullion landslide area, the expected change was 10 cm during the one-week survey; therefore, TLS data were filtered by a dissolved buffer 300 m away from all TLS SPs.

In order to delineate the slow-landsliding process, the ground surface is the target of the TLS survey. Occlusion is the obstruction between one point or region of the target area and the laser source. In the complex landslide environment, there can be many causes for occlusion. The obstruction between the TLS source and the ground surface can be heavy vegetation or collapsed rocks; the rolling terrain at the Slumgullion site also blocked the view of the TLS. Therefore, multiple viewpoints were required to get full coverage of the spatially complex natural environment. The overlapped area from different SPs permitted sensing of the target from various angles and distances. Vegetation on the landslide is at a right angle to the ground surface, thus scanning on both sides of the blocking vegetation was able to mitigate the occlusion caused by trees and bushes.

Choosing a longer range and using multiple SPs helped reduce the occlusion by the rolling terrain. Figure 1-11 shows the occlusion by the rolling terrain.

If several targets are illuminated by a single divergent beam, the TLS receiver can resolve those targets depending on how closely they are located. Temporal resolution is used to describe the ability of TLS to resolve different targets from a single laser pulse (see Figure 1-12). If T_p is the laser-pulse temporal width, c is the speed of laser, then the minimum resolvable distance ΔR is

$$\Delta R = \frac{cT_p}{2}. \tag{1-15}$$

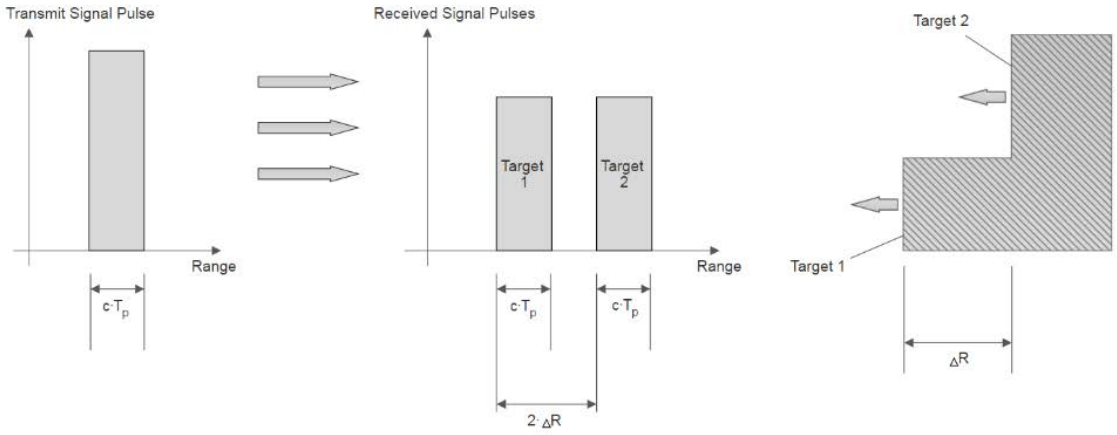

Figure 1-12 Temporal resolution illustration for TLS. The transmitted signal pulse and the returned signal have a length of T_p , the minimum resolvable distance is reached when echoes from multiple targets almost overlap with each other.

In our study, the TLS used a $T_p = 3$ ns pulse length; therefore, the minimum resolvable distance was $\Delta R = 0.45$ m. Targets located more than 45 cm apart were resolved as different returns. Up to fifteen returns can be recorded using the VZ-2000 TLS scanner under its 100 kHz scan program. The echo distribution in one of the scans taken at the Slumgullion landslide is shown in Figure 1-13.

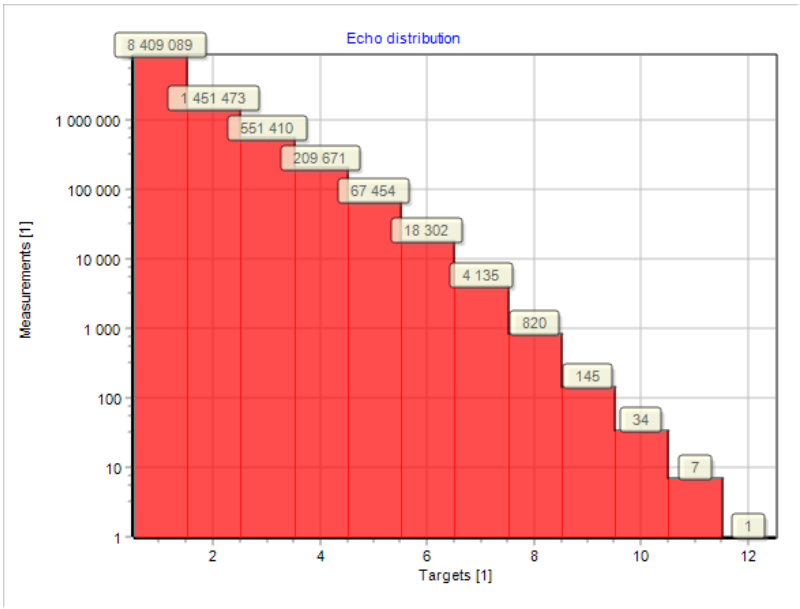

Targets | Measurements | Percentage

1	8409089	78.49761%	7	4135	0.03860%
2	1451473	13.54929%	8	820	0.00765%
3	551410	5.14733%	9	145	0.00135%
4	209671	1.95725%	10	34	0.00032%
5	67454	0.62967%	11	7	0.00007%
6	18302	0.17085%	12	1	0.00001%

Total measurements: 10712541

Total targets: 14289270

Figure 1-13 The echo distribution for the panorama scan at SP1 July 7th. For this scan, up to 12 targets were recorded by a single laser beam from TLS. The number of emitted laser pulses are counted as Total measurements, and the number of received laser echoes are counted as Total targets.

1.4.6 TLS data acquisition and environmental calibration

In this subsection, we present the TLS survey parameters and environmental calibrations for our landslide survey. A panorama scan pattern was used to acquire point clouds at the landslide area. The angular resolution for line scan and frame scan was 0.04˚, and the scan program was set as 100-kHz scan frequency, with the longest detection range at 1800 m. External GPS (R10) was used for georeferencing. The data collected at each SP were stored in the scanner's internal storage, and all data were downloaded as a project at the end of each day.

A list of tie points was set up during the scanning process. A tie point is a target with a well-known position. The tie points used for our project were cylinder reflectors that have high-laser reflectance. Shown in Figure 1-8 (a), the big reflector was 25 cm high and 20 cm long; shown in Figure 1-8 (b), the small reflector was 10 cm high and 10 cm long. The surface of a reflector was made of highly retroreflector tapes that had extremely high-laser reflectance, even far away from the TLS. The geometry of each reflector was captured by a TLS scan pattern called fine-scan. Different from a panorama scan, a fine-scan only targets toward where the reflector is located, and the angular resolution for line and frame scan is extremely high (0.001˚ for line and frame scan). Therefore, the position of the reflector was measured accurately, inferred from the TLS scanner. In the field, the reflector was put on a leveled tripod collocated with GPS units. This setup, combining GPS units and reflectors, linked the tie point position inferred from the TLS and the position measured by GPS units.

The SPs were reoccupied in three TLS projects. The purpose of maintaining almost the same scan view was to minimize the change detection error caused by the different looking angles. Ground markers with ribbons were used to mark each relocated SP.

The TLS were calibrated before surveying to eliminate the atmospheric effect on the laser pulse. The slant range of the TLS was calculated as

$$R = c_g \frac{t}{2} = \frac{c_0}{n_g} \times \frac{t}{2}. \quad (1\text{-}16)$$

The time measurement t was calibrated when the equipment was built. Laser velocity is affected by the ambient environment; if the latter changed dramatically, calibration could be made for each SP. In Equation (1-16, c_g is the group velocity in the medium at the 1550 nm laser wavelength, and c_0 is the speed of light in vacuum. The group velocity is a function of its index n_g, which is a function of temperature, pressure, and humidity. The group velocity of air exhibits only small fractional changes (k), described in the units of Parts Per Million (ppm). For example, if the atmospheric condition changes from n_{g1} to n_{g2}, the ToF will change accordingly:

$$t_2 = \frac{n_{g2}}{n_{g1}} t_1 = (1 + k10^{-6}) t_1. \quad (1\text{-}17)$$

According to RIEGL (2015), under the ideal test environment (12˚ Celsius temperature, 1000 mbar air pressure, and 60% relative moisture), sensitivity of corrections in ppm on three atmospheric parameters is listed in Table 1-6.

Table 1-6 Correction in ppm on three atmospheric parameters (RIEGL, 2015).

A change in temperature of 1˚ Celsius yields a change in correction of 1ppm
A change in air pressure of 10 mbar yields a change in correction of -2.7 ppm
A variation of relative moisture from 0-100% yields a change in correction of 0.5 ppm

From Table 1-6, it can be seen that air pressure and temperature dominate the correction in ppm. Therefore, before each project, these two parameters were measured by an atmospheric meter and input to the scanner for an automatic correction every survey day.

There is a Nikon D800 camera mounted on top of the TLS scanner, which is used to get the true color of the scanned object; the camera required calibration before surveying. It connects with the scanner by inner mounting points. For the landslide project, the trigger mode for the camera was set at automatic, so that exposure time and aperture were chosen automatically, based on the lighting conditions. This setting was necessary, because luminance difference can be huge for a panorama scan when the camera takes photos into sunlight. After each scan cycle, a panorama was taken by combining a series of photos from different frame angles. Twenty percent of image overlap was set for the project.

1.4.7 ALS and airborne SAR survey

During the TLS survey, the airborne laser scanning (ALS) and airborne synthetic aperture radar (airborne SAR) data (Cao et al., 2017) were collected simultaneously by the National Center for Airborne Laser Mapping (NCALM, http://ncalm.cive.uh.edu). ALS data has the advantage of identifying scarps of landslide covered by tree canopies; it is widely applied in identifying historical and current active landslides hidden in forested areas (Wang et al., 2013). ALS datasets is used for landsliding detection in Chapter 3 to compensate the limited spatial coverage of TLS.

2 The Workflow for TLS Data Processing

Airborne LiDAR is broadly utilized in high-resolution land surveying, and there are refined workflows on how to handle airborne LiDAR data in urban areas (Shan and Toth, 2008). However, there are a few differences between ALS and TLS which lead to unique methods to process TLS data. In this chapter, we present a workflow for TLS data processing to generate high-resolution Digital Terrain Models (DTMs) using TLS data we collected from our survey at the Slumgullion landslide.

Compared with ALS, TLS datasets have extremely dense-point records (e.g., one point per square centimeter). Furthermore, the application of LiDAR in a natural environment with complex geomorphic surface roughness also challenges the standard LiDAR data processing workflow. Therefore, we developed a unique workflow to process data we collected from the GPS and TLS integrated survey at the Slumgullion landslide following steps of data reduction, point cloud registration, point cloud filtering, and point cloud gridding (Figure 2-1). The following sections present each step in detail.

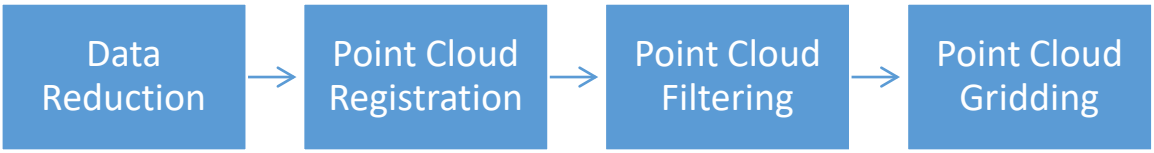

Figure 2-1 The workflow for TLS data processing.

2.1 Data Reduction

The TLS survey at the Slumgullion landslide resulted in extremely large datasets which tended to strain most software programs used for terrain analysis. TLS produced a massive number of positional measurements with an extremely high-spatial resolution that ranged in size from the fingerprint (e.g., 3 cm × 3 cm) to the handprint (e.g., 10 cm × 10

cm) levels (Xiong et al., 2017). A single TLS project processed by RiSCAN Pro software packages can be as large as ten gigabits. Therefore, data reduction was the first issue that needed to be considered before conducting TLS data processing and analysis (Buckley et al., 2008).

We used an octree filter for data reduction for all scans and a deviation filter for removing inaccurate measurements. Before we discuss these filters, we introduce the general format used to store point clouds and the general structure used for processing them.

2.1.1 LAS format

Point clouds are large datasets composed of 3D-point data. LiDAR point clouds are stored in LAS format. LAS is a standard output data format shared by almost all LiDAR hardware and software tools. This format combines GPS, POS, laser-pulse range data, and their attributes to produce XYZ data. It is the public format for the interchange of any three-dimensional XYZ tuplet between data users. This binary format is an alternative to proprietary systems or the generic ASCII file interchange system used by many companies. Compared with proprietary systems, LAS is more interchangeable across different systems and platforms; compared with ASCII files, LAS is more compact; thus, it is small in size and fast for processing. Also, LAS preserves the specific attributes that are unique for LiDAR records, such as return numbers and waveform information. The latest version, LAS 1.4, was approved by the American Society for Photogrammetry and Remote Sensing (ASPRS) Board on November 14th, 2011.

The LAS 1.2 Format was used by TLS and ALS in our project. This format contains binary data consisting of a public header block, any number of (optional) Variable Length Records (VRLs), and the point data records. All data is in little-endian format. The header block consists of a public block followed by VRLs. The public block contains generic data

such as point numbers and coordinate bounds. The VRLs contain variable types of data, including projection information, metadata, and user application data (ASPRS, 2008). There are four types of point data records. Only one type is allowed for a single LAS file. In our project, ALS data used Format 1, and TLS data used Format 3, as listed in Table 2-1. The only difference between the two Formats is that format 3 restores true color information for each point cloud.

Table 2-1 LAS file point data record, Format 1 and Format 3 (ASPRS, 2008).

Item	Format	Size	Required
X	long	4 bytes	*
Y	long	4 bytes	*
Z	long	4 bytes	*
Intensity	unsigned short	2 bytes	
Return Number	3 bits (bits 0,1,2)	3 bits	*
Number of Returns (given pulse)	3 bits (bits 4,5,6)	3 bits	*
Scan Direction Flag	1 bit (bit 6)	1 bit	*
Edge of Flight Line	1 bit (bit 7)	1 bit	*
Classification	unsigned char	1 byte	*
Scan Angle Rank (-90 to +90) –Left side	unsigned char	1 byte	*
User Data	unsigned char	1 byte	
Point Source ID	unsigned char	1 byte	*
GPS Time	double	8 bytes	*
Red (Format 3 only)	unsigned short	2 bytes	*
Green (Format 3 only)	unsigned short	2 bytes	*
Blue (Format 3 only)	unsigned short	2 bytes	*

We used several software packages for LAS data processing. Point cloud datasets in LAS 1.2 format were generated using RiSCAN PRO software package, 64 bit Version 2.2.1

(RIEGL, 2015). Because of the intrinsic-binary format of LAS datasets, they can be treated with MATLAB. CloudCompare is another software package that was used to manipulate point clouds, with its octree-based processing. Based on different purposes, the data were gridded using Surfer and ArcGIS. The Surfer software package accepts LAS as an input format. For the ArcGIS software package, we used the Create LAS Dataset tool from ArcCatalog. There is a scalability problem for ArcMap, in which point cloud datasets are thinned based on the current extent and the number of points within that extent. The limit of the number of points displayed is five million. For the landslide area in our study, most TLS single scans contained fifteen million points. Therefore, the scalability problem was a drawback for TLS point cloud display in ArcMap; details from point clouds cannot be seen at the macro scale. Originally, the LAS dataset in ArcMap is designed for ALS data which have a lower point density compared with TLS data sources.

2.1.2 Octree structure for point clouds

The octree structure is a recursive and regular subdivision of three-dimensional space. The structure is used to store and process point cloud data in three-dimensional space. In practice, the method is started by dividing the bounding box of the point cloud into eight equivalent cubes. A recursive subdivision is repeated within each cube. After recursive subdivision, the process stops when no point lies in the cubes or when the minimum size of the cubes is reached.

The subdivided cubes within each level are called cells. The octree structure enables a rapid search of each cell's location and its neighboring cells. Neighborhood calculation is fast, based on octree structure. Figure 2-2 shows the octree subdivision principle (Girardeau et al., 2005).

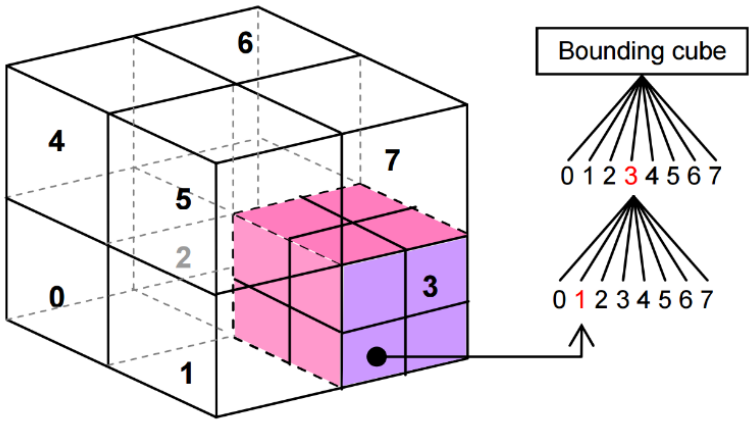

Figure 2-2 The principle of octree subdivision. The drawing shows the subdivision principle and the tree structure, using a second level subdivision of a bounding cube (Girardeau et al., 2005).

For a n-level subdivided octree structure, the index of every point within the structure is stored with $3n$ bits. In each level, there are three bits forming a code number from 0 to 7 to describe the cell's location. This octree structure makes it easier for code searching, such as dichotomic, and it offers a good flexibility to add or compress point cloud records.

2.1.3 Octree filter

An octree filter is designed based on the octree structure of a TLS's point cloud. Points within each end member cell are merged as a single point, and that point is located at the gravity center of all points within that cell. If two points from the neighboring cells are too close to each other, they are merged to their center as well. There is an option to delete cells containing only one point; this can be used to remove isolated points.

In our study for the landslide area, a $5\ cm \times 5\ cm \times 3\ cm$ octree size was chosen for the end member cell, and points that were closer than 10% of increment were merged. Because of the occlusion pattern, there were isolated points that represented the true

earth surface which had to be kept; thus, no isolated points were removed from the octree filter due to the rough and complex texture of the point cloud for the natural landslide surface.

After the octree filter, the data volume was reduced by more than half for each SP. For example, in the project conducted on July 10th, the point number for each SP before and after applying the octree filter is listed in Table 2-2.

Table 2-2 Number of points within each scan position before and after the octree filter.

Scan Position	SP1	SP2	SP3	SP4	SP5
Before	14336189	14959019	14867345	14867358	15269810
After	6423876	6077972	6856629	5307276	4042601
Reduced by (%)	55%	59%	54%	64%	74%
Scan Position	SP6	SP7	SP8	SP9	Sum
Before	15025821	17340210	14976214	14042066	135684032
After	4461555	9534131	5974807	5167416	53846263
Reduced by (%)	70%	45%	60%	63%	60%

The octree filter computed the center of gravity of the points within each cell; thus, it preserved the point distribution and the geometry information that we are interested in. Therefore, the octree filter proved to be an ideal filter that reduced the data volume, yet preserved the point distribution characters.

2.1.4 Deviation filter

While applying the octree filter, the distorted point cloud measurement can be removed by a deviation filter. The deviation is the shape distortion of the laser returns compared with the laser source. It is an integer number with no unit measured by TLS. A small deviation means less distortion and a high deviation means distorted laser records; these

may result from the edge effect, multiple returns, and a tilted target surface. Therefore, a deviation filter was used to remove points that were not measured accurately.

Deviation 0 is the ideal case where no distortion is found between the emitted and received echoes. Deviation up to 10-15 should be treated as robust measurements (RIEGL, 2015). The increase of deviation is caused by scanning over the edges of the target, scanning through vegetation, or scanning over a tilted surface, where the surface is not perpendicular to the laser beam. Our study landslide area has dense vegetation and rolling topography. As seen in Figure 2-3, most of the echoes from trees on the landslide area have higher deviation. Also, echoes from the terrain that are facing the TLS have lower deviation compared to those that are tilted away from the TLS.

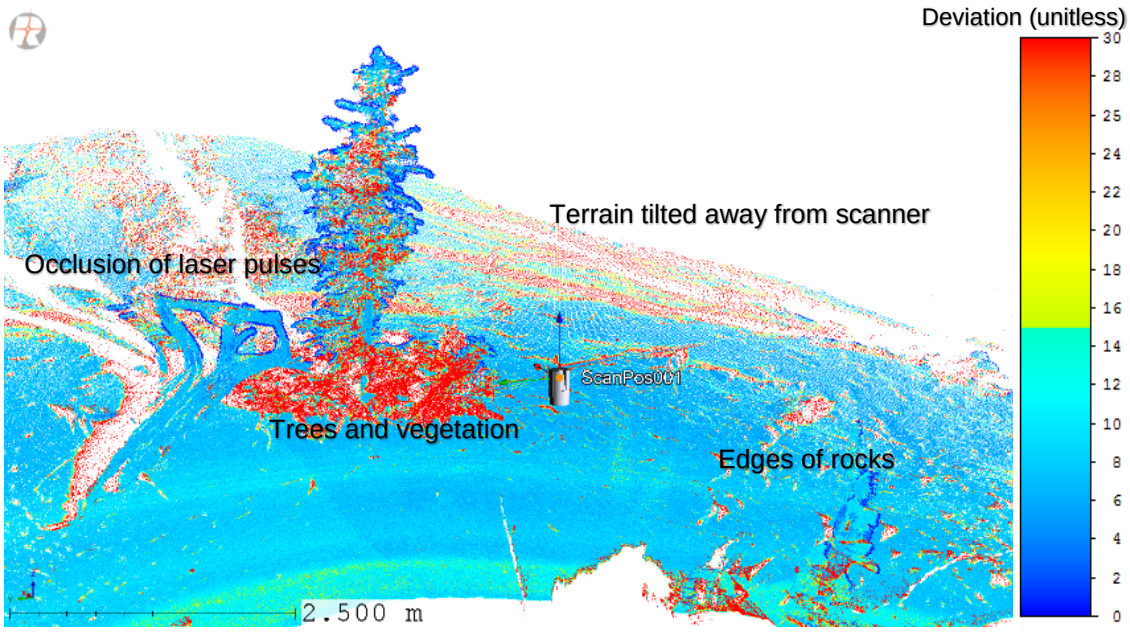

Figure 2-3 TLS point cloud colored by deviation (unitless). Warmer colors show higher deviation; cooler colors show smaller deviation. Laser echoes from trees and vegetation beneath the trees have high deviation. Red strips on the ground show the edges of rocks that have high deviation. Echoes of terrain that tilted away from TLS have high deviation. The white cutout surrounded by point cloud illustrates the occlusion of laser pulses. For the landslide area, the criterion for deviation was expanded up to 30 because of the complex natural environment and the broad range of target roughness.

However, for distant targets, the shape of the laser could hardly be determined with a faint return echo. Thus, all the laser echoes tended to be similar in shape, so that the deviation measurements tended to be zero. In this case, small deviation did not necessarily mean less distortion. Therefore, we wanted to explore the relation between the deviation and the range of laser measurement, so that we could determine a proper threshold for filtering the distorted laser record collected for the landslide area.

Figure 2-4 shows the relation between the range and deviation. Raw point cloud from the SP2 July 10th project was used as the sample data. Parallel to the x-axis, the deviation

distribution was calculated in a normalized histogram manner, in which the relative frequency of deviation was calculated for a particular range; the frequency is shown by color. Figure 2-4 shows a stack of deviation distribution at all ranges. In order to explore the boundary of the deviation measurement, the logarithm of the frequency was plotted, and is shown in Figure 2-5. In the sample LAS datasets, the maximum range is 1500 m, and the deviation ranges from 0 to 1517. The frequency of certain deviation D_j at certain range R_i is shown in Equation (2-1).

$$Range \in [0,1500],\ R_i = [Range_i, Range_i + 10];$$
$$Deviation = [0,1,2,\dots,1517],\ D_j = \left[Deviation_j, Deviation_j + 5\right]; \qquad (2\text{-}1)$$
$$Frequency_{ij} = \frac{Num\ of\ points(D_j,R_i)}{Num\ of\ points(R_i)}.$$

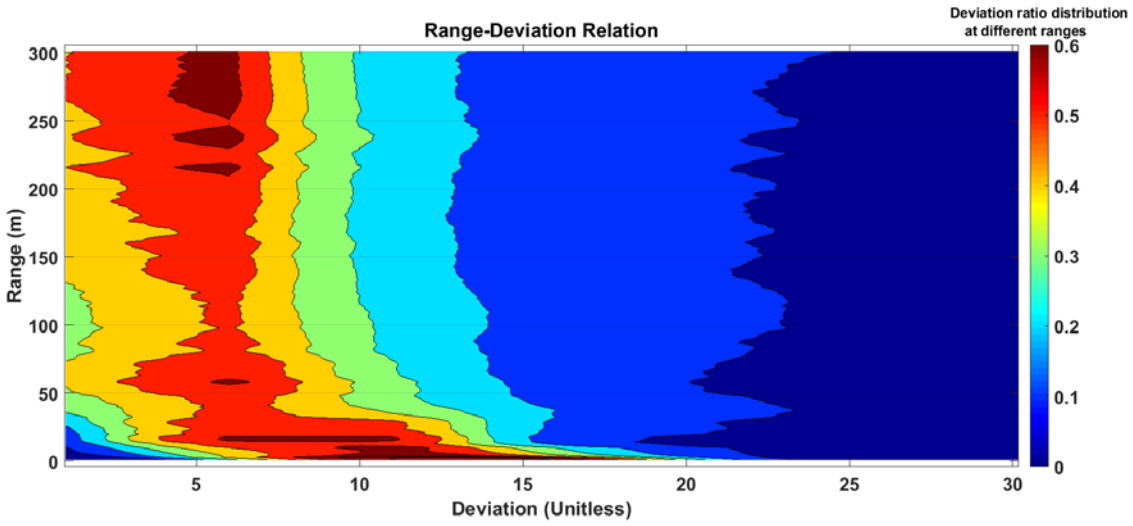

Figure 2-4 The relation between point cloud's range and deviation. Parallel to the x-axis, the color shows the relative frequency of deviation at a certain range. The figure is a stack of deviation distribution at all ranges.

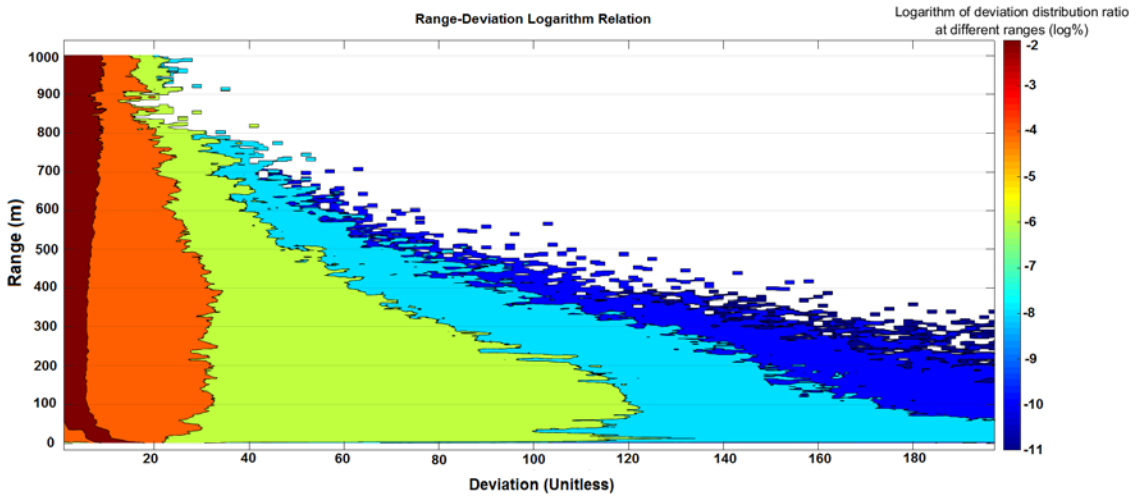

Figure 2-5 The logarithm relation between point cloud's range and deviation illustrated in Figure 2-4.

In Figure 2-4 and Figure 2-5, it can be seen there is a tendency for the deviation to decrease when the range increases. This is because the laser power received became weaker when the range increased. For distant targets, the shape of the laser could hardly be determined from a weak echo, and all the laser tended to be similar in shape, so the deviation tended to be zero. In this case, small deviation did not necessarily mean less distortion.

In Figure 2-5, there is a clear boundary that lies at 20 to 30 deviation for almost all ranges of measurement (the boundary between colors orange and green); beyond that, the deviation distribution is sensitive to range change. This is the boundary at which distorted laser pulses coming from distant targets begin to be classified as small deviation echoes. This boundary was used to separate the good data from the bad which could be in small deviation yet distorted for remote targets. Laser records with deviation less than 30 were treated as robust measurements in our study; points with deviation higher than 30 were

removed. The threshold for the deviation filter is highly dependent on the survey environment; this was especially true for our landslide area, where heavy vegetation and rough terrain surface exist. The method developed here can be used to analyze the range-deviation relation in another environment for TLS measurements.

There is not a fixed sequence for conducting the octree filter and the deviation filter. The deviation filter is preferred over the octree filter for creating a robust point cloud dataset. However, if the dataset is huge, the octree filter should be conducted first to improve workflow efficiency. In our workflow, the deviation filter was used before the octree filter.

2.2 TLS Point Cloud Registration and Georeferencing

As the second step of the workflow, the process of montaging all scans taken within a project is called registration. Although TLS has a dense point cloud recorded, complete coverage of the ground surface can only be guaranteed if different SPs are combined. VZ-2000 TLS uses an internal sensor frame to store raw point cloud data; this frame is called the Scanner's Own Coordinate System (SOCS). Multiple SOCS are transformed and combined into a common reference frame called a Project Coordinate System (PRCS). The Global Coordinate system (GLCS) is the coordinate system into which the PRCS is embedded with the help of GPS measurements.

In our Slumgullion landslide survey, all scans acquired within the same day were saved in a single project. The position of the TLS scanner within each project is known as a Scan Position (SP), as mentioned before. One TLS project may carry only one PRCS. PRCS can be an existing SOCS. Usually, SOCS that are defined by the first SP or the SP that carries the most control points is used to set up the PRCS. Other SPs are transformed from their own SOCS into this PRCS (RIEGL, 2015). The transformation is a rigid coordinate transformation with no scale correction. In some cases, if the scale of

measurement is different between SPs, the three-dimensional similarity transformation can be used. Using different scanners for the same project may cause a scale difference.

2.2.1 Coordinate transformation for TLS point clouds

The process that upgrades all the SOCS coordinates into a PRCS is called registration. The rigid coordinate transformation can be described by a M_{SOP}. M_{SOP} stands for a Matrix for Sensor's Orientation and Position. It consists of a translation part T and a rotation part R. The matrix stores the position and orientation information in the PRCS for each SP. It has the form

$$MSOP = \begin{bmatrix} r_{11} & r_{12} & r_{13} & t_1 \\ r_{21} & r_{22} & r_{23} & t_2 \\ r_{31} & r_{32} & r_{33} & t_3 \\ 0 & 0 & 0 & 1 \end{bmatrix}, \tag{2-2}$$

where the translation part describes the shift of the coordinate and the rotation part describes the triaxial rotation of the coordinates during the transformation. The rotation of the scanner is defined by the rotation of its three axes, Roll for the x-axis, Pitch for the y-axis, and Yaw for the z-axis. Roll, pitch and yaw relate to the rotation matrix by the following formula:

$$R = R_Z \cdot R_Y \cdot R_X$$

$$\begin{cases} R_X(R) = \begin{bmatrix} 1 & 0 & 0 \\ 0 & \cos(R) & -\sin(R) \\ 0 & \sin(R) & \cos(R) \end{bmatrix}, The\ Roll\ matrix\ with\ roll\ angle\ R \\ R_Y(P) = \begin{bmatrix} \cos(P) & 0 & \sin(P) \\ 0 & 1 & 0 \\ -\sin(P) & 0 & \cos(P) \end{bmatrix}, The\ Pitch\ matrix\ with\ pitch\ angle\ P. \\ R_Z(Y) = \begin{bmatrix} \cos(Y) & -\sin(Y) & 0 \\ \sin(Y) & \cos(Y) & 0 \\ 0 & 0 & 1 \end{bmatrix}, The\ Yaw\ matrix\ with\ yaw\ angle\ Y \end{cases} \tag{2-3}$$

To register data from SOCS into the PRCS, data points are multiplied with the rotational part of the M_{SOP}, and plus the translation part of the M_{SOP} of the SP. The key component

for any registration is to determine the M_{SOP}. For TLS, the M_{SOP} is calculated based on the measurement of position and rotation. The method of registration is the method that calculates the M_{SOP} for each SP:

$$\begin{bmatrix} X \\ Y \\ Z \end{bmatrix}_{PRCS} = T_{M_{SOP}} + R_{M_{SOP}} \begin{bmatrix} X \\ Y \\ Z \end{bmatrix}_{SOCS} . \quad (2\text{-}4)$$

The Global Coordinate System (GLCS) is the coordinate system into which the project coordinate system is embedded. Registration into the GLCS is called georeferencing. Compared with PRCS, a GLCS may store more digits of numbers describing the coordinates of the point cloud.

For the Slumgullion landslide project, the GLCS was used to organize the TLS data. The advantage of using GLCS compared with PRCS is that GLCS is the common coordinate across the platform for ground-based and airborne-based measurements. Also, the setup and maintenance of a local PRCS for a repeated survey can be costly. Consequently, GLCS was the better choice for our project. The GLCS used for this project is the Universal Transverse Mercator system (UTM Zone 13) with the ellipsoid height calculated from the North American Datum 1983 (NAD83, epoch 2011). Similar to registration from SOCS to PRCS, the georeferencing of a project is done by calculating the Matrix of Project's Orientation and Position ($\boldsymbol{M_{POP}}$). By multiplying the $\boldsymbol{M_{SOP}}$ matrix, data are georeferenced from PRCS into GLCS. For some registration methods, SPs can be directly registered or georeferenced into the GLCS. In that case $\boldsymbol{M_{POP}}$ is simply an identity matrix or a matrix that contains only the translation part, because PRCS cannot hold large digits of coordinates. The relationship between the SOCS, PRCS, and GLCS is shown in Figure 2-6.

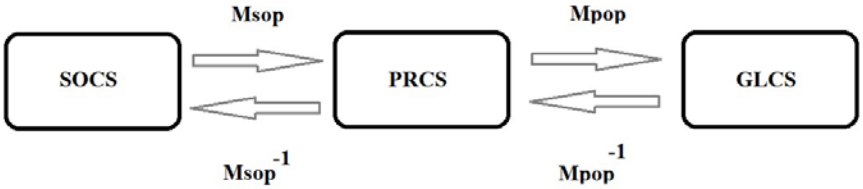

Figure 2-6 Coordinate transformation among the Scanner's Own Coordinate System (SOCS), Project Coordinate System (PRCS), and Global Coordinate System (GLCS). Transform is accomplished by multiplying the Matrix for Sensor's Orientation and Position (M_{SOP}) or multiplying the Matrix for Project's Orientation and Position (M_{POP}).

There are several methods to register data, i.e. to determine the $\boldsymbol{M_{SOP}}$ or $\boldsymbol{M_{POP}}$. Generally, these methods fall into two categories: registration with corresponding points, and registration for which corresponding points do not exist. In our study, both categories were covered, five methods using the point correspondences were compared, and one method using no correspondences was used for fine-alignment of the registered result.

To determine the $\boldsymbol{M_{SOP}}$ or $\boldsymbol{M_{POP}}$, six degrees of freedom (X, Y, Z, Roll, Pitch, and Yaw) had to be calculated. Different registration methods required different inputs to determine all six parameters, as listed in Table 2-3. The accuracy of the input and the method calculating the orientation and position matrix determine the final accuracy of a registration result.

Table 2-3 Input required by different registration methods that rely on point correspondence.

Registration method	Require scanner's position?	Require inclination sensors for Roll and Pitch?	Require compass reading for Yaw?	Require corresponding points between origin and transformed coordinate?
Direct georeference	Yes	Yes	Yes	No
Backsight	Yes	Yes	No	One tie point required
Three-point solution	Yes	No	No	Two tie points required
One-point solution	No	Yes	Yes	One tie point required
Freestation	No	No	No	Three tie points required

The accuracy of the measurement for the input mentioned above is as follows:

The accuracy of the scanner's position is determined by the GPS collocated with the TLS. GPS used for this study is a Trimble Net R10 mounted externally above the TLS scanner.

The accuracy of the inclination sensor is $\pm\mathbf{0.008}$° (one sigma under RIEGL test conditions). The readings from two inclination sensors determine how accurate the TLS is leveled.

The accuracy of the compass is $\mathbf{1}$° (one sigma under RIEGL test conditions). The performance of the compass is undisturbed by earth's magnetic field, but it may be disturbed by the local magnetic field or electromagnetic influence caused by the rechargeable battery. Larger uncertainty may occur when the instrument is not roughly leveled (tilt angle bigger than $\pm\mathbf{3}$°).

The accuracy of the angular encoders is $\pm\mathbf{0.0015}$° for vertical (Line) scan; $\pm\mathbf{0.0005}$° for horizontal (Frame) scan.

The accuracy of the range measurement is $8\ mm$; the precision (repeatability) of the range measurement is $5\ mm$ (one sigma at 150 m range under RIEGL test conditions).

For our survey at the Slumgullion landslide, there were several options for data registration. Direct georeference, Backsight, Three-point solution and Freestation registration were compared. Table 2-4 shows all the available information acquired from the GPS and TLS integrated survey that could be used for TLS registration.

Table 2-4 Measurements taken as inputs for TLS registration.

Date/ Project	Scanner's Position Measured by GPS	Inclination sensors	Compass reading	Tie points with GPS units and collocated reflectors
July3	7 scans conducted, SP1,SP3,SP7 do not have GPS records.	Available for all SPs	SP7 not available	Reference stations: BA, RL, ML. Rover stations: L1.
July7	8 scans conducted, SP8 does not have GPS record.	Available for all SPs	SP8 not available	Reference stations: BA, RL, MH, ML. Rover stations: L1, L2.
July10	9 scans conducted, all have GPS records.	Available for all SPs	Available for all SPs	Reference stations: BA, RH, RL, MH, ML. Rover stations: L0, L1.

The Scanner's position was determined by the R10 GPS equipped externally with TLS. GPS data were post-processed by OPUS, with a rapid static relative positioning referring to the local CORS mentioned in Chapter 1, section 1.4 (Table 1-4). The observation window for these GPS data usually lasted 20 to 30 minutes, and overall measurement accuracy was a couple of centimeters. OPUS provided the positions of each SP and the measurement accuracy. Disabled GPS records may have been caused by the battery issues and the observer's mistake. The TEQC toolkit was used to trim the data before

uploading to OPUS. For the SPs that have no GPS data for the scanner's position, methods like direct georeference and backsight registration are not available.

The inclination sensor worked well in the field. Before each scan, the tripod for the TLS was leveled by a torpedo level for a coarse leveling. Fine adjustment of the SOCS horizontal plane was realized by the inclination sensors inside the TLS. Two inclination sensors were able to correct any misalignment within five degrees of the row and pitch rotation which was used to define the platform horizon. Alone among all the compared registration methods, free station registration does not require inclination sensor reading.

Compass reading is affected by the local magnetic field. A disability of the compass may be caused by a TLS battery issue or other electronic device interference (e.g., cell phone and laptop). A bad compass reading may result from an unstable tripod setup; misalignment that is more than three degrees may cause an unstable tripod setup (RIEGL, 2015). Direct georeferencing and one-point solution use compass north as yaw measurement to align the scan; these are not available when no compass or a bad compass reading is collected.

Tie points are the points that correlate the original reference frame and the transformed reference frame. With a field set up like that in Figure 1-8, the reflector's position is captured by the TLS within its SOCS; collocated GPS records the tie point's position in a global coordinate. Therefore, the position of the tie point is recorded by two coordinate systems, and it creates a link or tie that helps to solve the orientation and position matrix that is used for the coordinate transformation. For backsight registration, one point's correspondence is used to determine the direction of the coordinate as a replacement of the compass. For three-point registration, two tie points are used to determine the direction and define the horizon for the scanner. For freestation registration, at least three points'

correspondences are used to directly determine the six degrees of freedom for the matrix of orientation and position. More correspondences are preferred to validate the registration result. In practice, four tie points visible in each scan is a good rule of thumb if freestation registration is applied. In our survey at the Slumgullion landslide, the reference GPS stations were very useful, because they were located at the landslide boundary, and visible to almost all SPs. There were two GPS units located on the mountain (MH, ML) and three located on the left flank ridge (RH, RL, BA); these formed a robust network geometry for positioning.

2.2.2 Comparison of different registration methods

Different registration strategies were compared by analyzing tie points' coordinates inferred from the point cloud and the GPS units. Based on the registered TLS datasets, the coordinate of the tie points can be calculated from the point cloud; it can also be measured by the co-located GPS units. A proper registration will yield little difference between the two, and it will yield a small standard deviation among the tie point coordinates observed from different SPs.

The TLS project conducted on July 3rd is used as sample data here. In this project, the three reference GPS stations (BA, RL, ML) were captured by all SPs. The comparison of their positions inferred from the registered point cloud and the GPS units is listed in Table 2-5 through Table 2-7.

Table 2-5 Comparison of the base station (BA) coordinate inferred from TLS datasets and GPS measurements. The difference is shown by three components (dX, dY, dZ) under the UTM zone 13N reference frame. The distance (Dis.) indicates the range from BA to the scanner's location.

Method	From	To	Dis.(m)	X-Easting(m)	dX(m)	Y-Northing(m)	dY(m)	Z-EL Height NAD83(m)	dZ(m)
GPS/Meas.	BA		nan	301883.796	nan	4207217.886	nan	3151.597	nan
TLS direct georeference registration	BA	SP2	33.601	301884.269	0.473	4207217.532	-0.354	3151.711	0.114
	BA	SP4	100.777	301885.266	1.47	4207219.269	1.383	3151.703	0.106
	BA	SP5	226.95	301890.973	7.177	4207215.600	-2.286	3151.617	0.02
	BA	SP6	291.53	301888.079	4.283	4207212.872	-5.014	3152.024	0.427
	Mean		nan	301887.147	3.351	4207216.318	-1.568	3151.764	0.167
	RMS		nan	2.614	nan	2.376	nan	0.155	nan
TLS backsight registration	BA	SP2	33.601	301883.795	-0.001	4207217.885	-0.001	3151.711	0.114
	BA	SP4	100.777	301883.805	0.009	4207217.876	-0.01	3151.703	0.106
	BA	SP5	226.95	301883.770	-0.026	4207217.807	-0.079	3151.617	0.02
	BA	SP6	291.53	301883.733	-0.063	4207217.832	-0.054	3152.024	0.427
	Mean		nan	301883.776	-0.02	4207217.850	-0.036	3151.764	0.167
	RMS		nan	0.028	nan	0.032	nan	0.155	nan
TLS three-point registration	BA	SP2	33.601	301883.801	0.005	4207217.906	0.02	3151.601	0.004
	BA	SP4	100.777	301883.802	0.006	4207217.880	-0.006	3151.597	0
	BA	SP5	226.95	301883.778	-0.018	4207217.807	-0.079	3151.590	-0.007
	BA	SP6	291.53	301883.806	0.01	4207217.832	-0.054	3151.587	-0.01
	Mean		nan	301883.797	0.001	4207217.856	-0.03	3151.594	-0.003
	RMS		nan	0.011	nan	0.039	nan	0.006	nan
TLS freestation registration	BA	SP2	33.601	301883.796	0	4207217.886	0	3151.597	0
	BA	SP4	100.777	301883.824	0.028	4207217.866	-0.02	3151.578	-0.019
	BA	SP5	226.95	301883.787	-0.009	4207217.870	-0.016	3151.591	-0.006
	BA	SP6	291.53	301883.784	-0.012	4207217.875	-0.011	3151.592	-0.005
	Mean		nan	301883.798	0.002	4207217.874	-0.012	3151.590	-0.007
	RMS		nan	0.016	nan	0.007	nan	0.007	nan

Table 2-6 Comparison of the position for GPS station ML inferred from TLS datasets and GPS measurements. The difference is shown by three components (dX, dY, dZ) under the UTM zone 13N reference frame. The distance (Dis.) indicates the range from ML to the scanner's location.

Method	From	To	Dis.(m)	X-Easting(m)	dX(m)	Y-Northing(m)	dY(m)	Z-EL Height NAD83(m)	dZ(m)
GPS/Meas.	ML		nan	301648.571	nan	4207449.055	nan	3180.465	nan
TLS direct georeference registration	ML	SP2	328.18	301644.772	-3.799	4207444.490	-4.565	3180.370	-0.095
	ML	SP4	230.662	301645.495	-3.076	4207445.922	-3.133	3180.455	-0.01
	ML	SP5	305.469	301648.085	-0.486	4207438.893	-10.162	3180.428	-0.037
	ML	SP6	456.977	301647.683	-0.888	4207438.845	-10.21	3180.743	0.278
	Mean		nan	301646.509	-2.062	4207442.038	-7.017	3180.499	0.034
	RMS		nan	1.406	nan	3.209	nan	0.144	nan
TLS backsight registration	ML	SP2	328.18	301648.398	-0.173	4207449.093	0.038	3180.370	-0.095
	ML	SP4	230.662	301648.626	0.055	4207449.291	0.236	3180.455	-0.01
	ML	SP5	305.469	301648.473	-0.098	4207449.085	0.03	3180.428	-0.037
	ML	SP6	456.977	301648.552	-0.019	4207449.228	0.173	3180.743	0.278
	Mean		nan	301648.512	-0.059	4207449.174	0.119	3180.499	0.034
	RMS		nan	0.085	nan	0.088	nan	0.144	nan
TLS three-point registration	ML	SP2	328.18	301648.401	-0.17	4207449.086	0.031	3180.460	-0.005
	ML	SP4	230.662	301648.485	-0.086	4207449.14	0.085	3180.476	0.011
	ML	SP5	305.469	301648.473	-0.098	4207449.069	0.014	3180.467	0.002
	ML	SP6	456.977	301648.547	-0.024	4207449.127	0.072	3180.478	0.013
	Mean		nan	301648.477	-0.094	4207449.106	0.051	3180.470	0.005
	RMS		nan	0.052	nan	0.029	nan	0.007	nan
TLS freestation registration	ML	SP2	328.18	301648.430	-0.141	4207449.106	0.051	3180.418	-0.047
	ML	SP4	230.662	301648.489	-0.082	4207449.106	0.051	3180.457	-0.008
	ML	SP5	305.469	301648.455	-0.116	4207449.107	0.052	3180.450	-0.015
	ML	SP6	456.977	301648.445	-0.126	4207449.095	0.04	3180.438	-0.027
	Mean		nan	301648.455	-0.116	4207449.104	0.049	3180.441	-0.024
	RMS		nan	0.022	nan	0.005	nan	0.015	nan

Table 2-7 Comparison of the position for GPS station RL inferred from TLS datasets and GPS measurements. The difference is shown by three components (dX, dY, dZ) under the UTM zone 13N reference frame. The distance (Dis.) indicates the range from RL to the scanner's location.

Method	From	To	Dis.(m)	X-Easting(m)	dX(m)	Y-Northing(m)	dY(m)	Z-EL Height NAD83(m)	dZ(m)
GPS/Meas.	RL		nan	302001.890	nan	4207324.712	nan	3167.543	nan
TLS direct georeference registration	RL	SP2	127.361	302000.459	-1.431	4207326.517	1.805	3167.608	0.065
	RL	SP5	118.436	302005.481	3.591	4207326.336	1.624	3167.590	0.047
	RL	SP6	131.682	302003.817	1.927	4207322.313	-2.399	3168.053	0.51
	Mean		nan	302002.912	1.022	4207324.970	0.258	3167.699	0.156
	RMS		nan	1.903	nan	1.687	nan	0.206	nan
TLS backsight registration	RL	SP2	127.361	302001.916	0.026	4207324.773	0.061	3167.608	0.065
	RL	SP5	118.436	302001.912	0.022	4207324.658	-0.054	3167.590	0.047
	RL	SP6	131.682	302001.936	0.046	4207324.605	-0.107	3168.053	0.51
	Mean		nan	302001.914	0.024	4207324.687	-0.025	3167.699	0.156
	RMS		nan	0.016	nan	0.062	nan	0.206	nan
TLS three-point registration	RL	SP2	127.361	302001.915	0.025	4207324.724	0.012	3168.014	0.471
	RL	SP5	118.436	302001.916	0.026	4207324.662	-0.05	3167.566	0.023
	RL	SP6	131.682	302001.972	0.082	4207324.611	-0.101	3167.860	0.317
	Mean		nan	302001.923	0.033	4207324.677	-0.035	3167.746	0.203
	RMS		nan	0.030	nan	0.045	nan	0.199	nan
TLS freestation registration	RL	SP2	127.361	302001.932	0.042	4207324.750	0.038	3167.549	0.006
	RL	SP5	118.436	302001.912	0.022	4207324.740	0.028	3167.558	0.015
	RL	SP6	131.682	302001.916	0.026	4207324.738	0.026	3167.557	0.014
	Mean		nan	302001.913	0.023	4207324.735	0.023	3167.552	0.009
	RMS		nan	0.015	nan	0.014	nan	0.006	nan

It can be seen from Table 2-5 through Table 2-7 that freestation registration gives the closest result to the ground truth, measured by the R10 GPS unit. Direct georeference performs the worst. Direct georeference registration and backsight registration are comparable in that both use the scanner's position and inclination sensors' measurements; therefore, they have the same estimation for the vertical component of the tie points. It can be seen that backsight registration improved the method for scanner orientation. A compass, in this case, works no better than a remote corresponding object when aligning the scan in a particular direction. Therefore, registration methods that use a compass reading as an input are unreliable.

One-point registration uses the compass reading to orientate the scanner. Using one tie point, the calculation of the scanner's position is sensitive to its orientation. For that reason, the registration result is similar to that of direct georeferencing; it is even worse when an unreliable compass reading is utilized.

Backsight registration and three-point registration are comparable in that both use corresponding points to determine the scanner's direction. The difference is that three-point registration improves the method for scanner horizon definition by using corresponding points rather than inclination sensors. The measurement accuracy for corresponding points depends on the line scan resolution of the TLS (0.0015˚); the measurement accuracy for inclination sensors is 0.008˚. The range measurement (8 mm) contributes little to the accuracy defining the horizon. This is because the horizon plane is defined by the Z components of these three points. TLS provides a side look of the target; with a small polar angle ($\boldsymbol{\theta}$), the range uncertainty contributes more on the XY measurement than on the Z component. Therefore, the horizon plane for TLS is more accurately defined using the corresponding points.

However, there are situations in which backsight registration gives a more accurate result than three-point registration. For example, the position of RL calculated from backsight registration is closer to the ground truth measured by the GPS units. This is caused by the incomplete TLS scan for the reflector; if there are occlusions and distortions in the fine scan of the reflector, there might be bias for reflector position in SOCS, which ultimately causes misalignment with the GLCS position. Such problems happened in the field when the reflector was too far, or the reflector was scanned in a tilted direction. The accuracy of TLS was usually lower in the field, due to unfavorable conditions, such as the following: poorly reflective or very rough surfaces, severe weather conditions (e.g., rain, hot wind, or fog), very bright ambient conditions, parallel incident angles, and excessive range (Zhou et al., 2017). Overall, the backsight and three-point solution yielded similar registration results.

Freestation registration is unique in that it does not require internal measurements from inclination sensors and a compass. All degrees of freedom were calculated from the corresponding points. Each pair of points linked the position in SOCS and GLCS. Therefore, the uncertainties of this method came directly from both coordinates. The measurement accuracy of SOCS depended on the line scan resolution (0.0015˚), the frame scan resolution (0.0005˚), and the range measurement accuracy (8 mm). The measurement accuracy of GLCS depended on the R10 GPS unit which was calculated by OPUS. As discussed in this section, the performance of the inclination sensors and compass was no better than direct distance measurement. Therefore, freestation registration performed better than direct georeference and backsight registration. The positions of reference stations were processed with OPUS-Static; the SPs were processed with OPUS-Rapid Static. The former required more than 2 h observation; the latter

required more than 20 min to calculate a static position. In the field, the reference stations were set up and collected data for more than 6 h (for BA more than 8 h). The scanner was set up for 20-30 min while the R10 GPS was recording the location for each scan position. With longer GPS observation time, static survey yields higher accuracy measurement than rapid static. Therefore, the freestation registration performed better than the three-point resolution and thus was the best registration for our case.

Another advantage of freestation registration is that it does not require the position of the scanner to be known. This made it possible to use the local coordinate system for TLS data registration. Thus, the measurement uncertainties of GPS measurement were able to be avoided. This local coordinate registration strategy was also used in our change detection analysis for point cloud comparison (see section 3.3).

All data collected in our Slumgullion landslide survey were registered using the freestation method. If not enough tie points existed, backsight and three-point registration were used as backups. The registration results are presented in Figure 2-12.

2.2.3 Georeferencing

Georeferencing is the registration that transforms SOCS or PRCS into GLCS. The transformation uses the orientation and position matrix calculated from the global coordinate. The global coordinate is provided by GPS measurement for tie points and scan positions. To determine the scanner's global position, an external Trimble R10 GPS unit was used. Figure 2-7 shows the mounting of the R10 on a VZ-2000 TLS scanner.

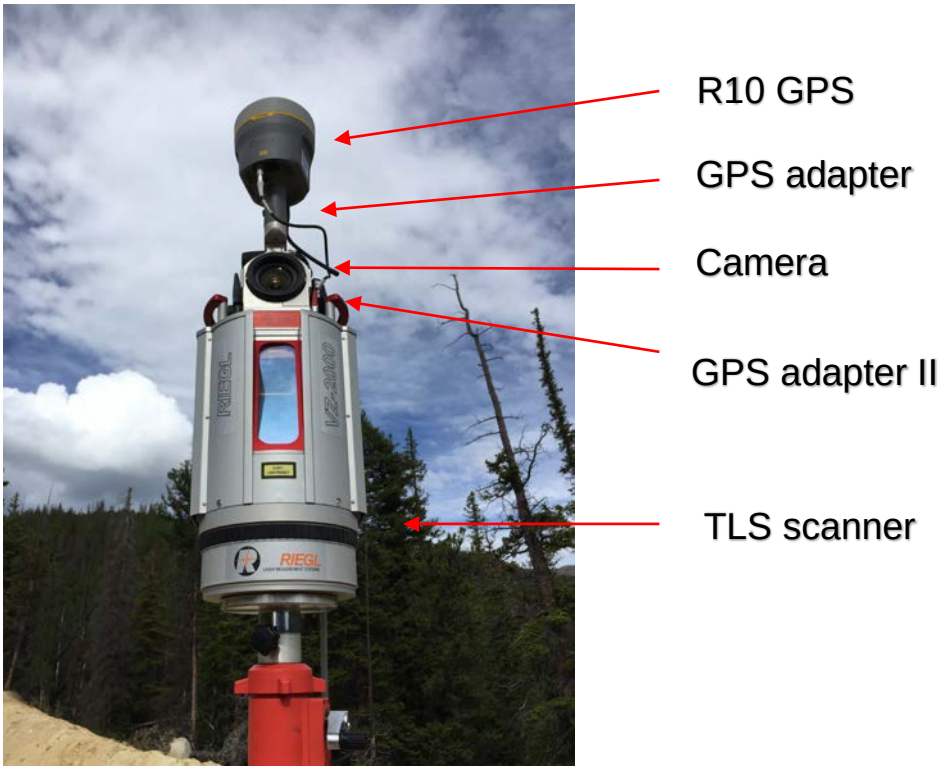

Figure 2-7 General set up of the TLS. The camera is fixed on top of the scanner inside the Special GPS Mounting Adapter 2; Adapter 2 connects with another adapter that mounts the R10 GPS unit.

When using the scan position data, there was a slight difference between the position of the TLS scanner and that of the R10 GPS antenna. A vertical shift between the center of the scanner and the phase center of the GPS unit is called an antenna height. A correct antenna height will help calibrate the measurement from the R10 to the center of the TLS which is the origin of SOCS.

The R10 GPS unit offered the position to the phase center of its antenna. With the correct antenna type, the software processing GPS data rectified that position to the bottom edge of the GPS (adapter not included). We obtained a 50 mm high adapter for R10 GPS unit. The distance from the center the scanner to the base plate of the R10 GPS adapter was

250.7 mm. In all, the distance between the origin of the scanner and the GPS was 300.7 mm.

SPs' GPS data were processed with the Online Positioning User Service (OPUS) with a rapid static relative positioning (OPUS-RS) referring to the local CORS. OPUS is a free, automated and Web-based GPS post-processing utility provided by the National Geodetic Survey (NGS). The website for OPUS is www.ngs.noaa.gov/OPUS. OPUS has become one of the most useful tools that NGS has provided to the surveying, engineering, and academic communities (Soler and Wang, 2016).

A standard report from OPUS is shown in Appendix I. One OPUS report contained position information for one SP. To collect the coordinates from all reports, a Visual Basic for Applications (VBA) script was written in an Excel Macro, and is given in Appendix II. This script is useful for extracting information from numerous OPUS reports.

Reference stations positions were processed by OPUS with a static relative positioning (OPUS-S) referring to the local CORS. Similar OPUS reports were generated, and the coordinates of each reference stations were able to be collected using the same VBA script mentioned above and given in Appendix II. The antenna height for reference stations was 20.8 cm. The difference between OPUS-S and OPUS-RS is discussed in subsection 2.2.4 to compare the GPS accuracy between reference stations and SPs.

2.2.4 Difference between OPUS-S and OPUS-RS

The position of OPUS-S (Static) was calculated by the Program for the Adjustment of GPS EphemerideS (PAGES). Using double-differenced phase measurements, PAGES can be used to estimate tropo corrections, station coordinates, linear velocities, satellite state vectors, and polar motions.

Previous studies have demonstrated that coordinates computed with OPUS-S are independent from the CORS geometry and the distance from the rover to the CORS control stations (Eckl et al., 2001); the only variable affecting the results is the time span of the observations (Soler et al., 2006). On the contrary, the OPUS-RS (Rapid Static) uses the geometry of the CORS and the distance to the rover to calculate coordinates. With limited observation times, the atmospheric conditions in the troposphere and ionosphere at the CORS stations were interpolated and/or extrapolated to predict atmospheric conditions at the rover. This interpolation causes the dependence of the geometry and distance. In general, static solutions and rapid static solutions provide similar accuracy; static solutions are preferred when longer observations of more than 2 h are available. The rapid static solution may not work in some areas due to its aggressive algorithms incorporating CORS geometry and distance; this is shown in Figure 2-9. The accuracy of OPUS-RS is shown in Figure 2-8.

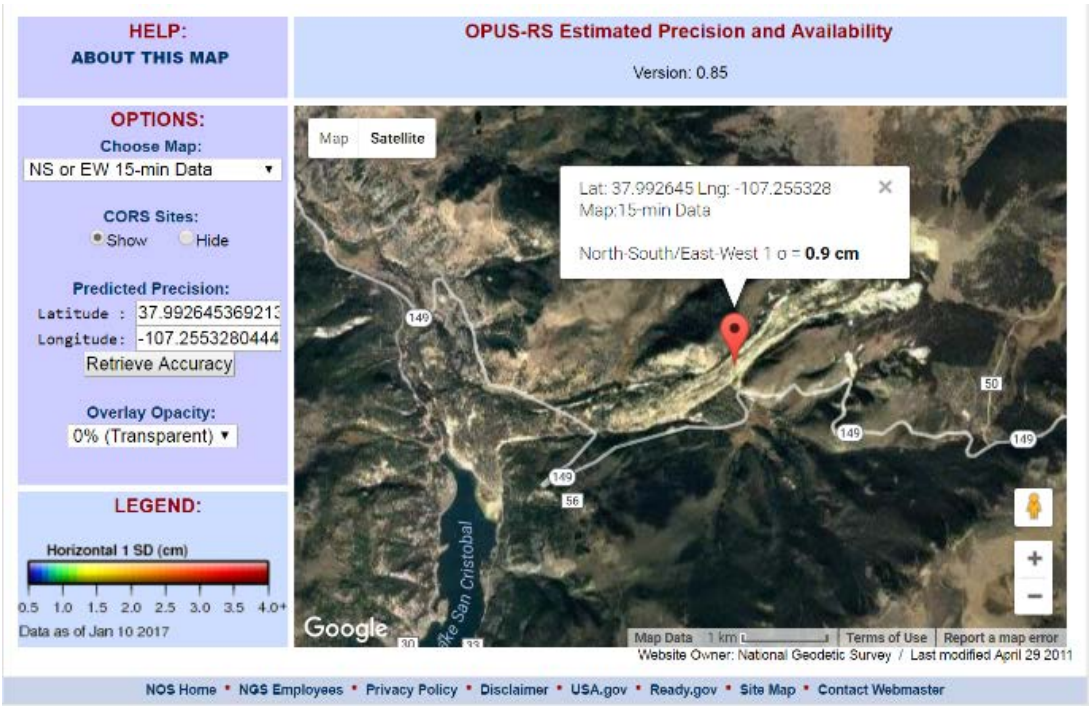

Figure 2-8 Horizontal and vertical components accuracy of OPUS-RS results at the Slumgullion landslide. Horizontal accuracy (top) is below 1 cm for one sigma. Vertical accuracy (bottom) is below 3.5 cm for one sigma.

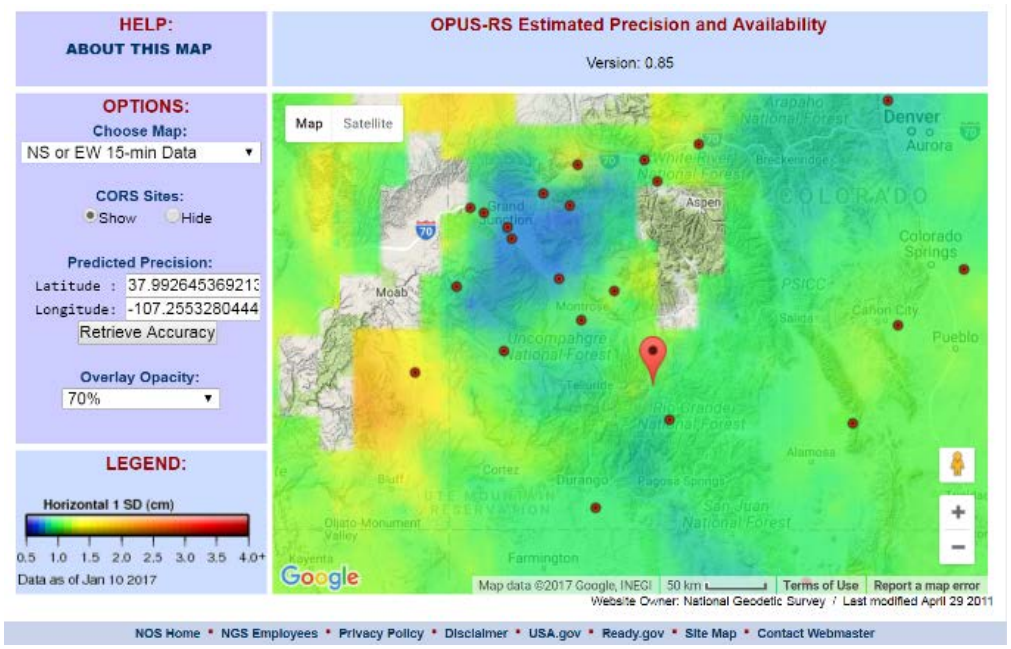

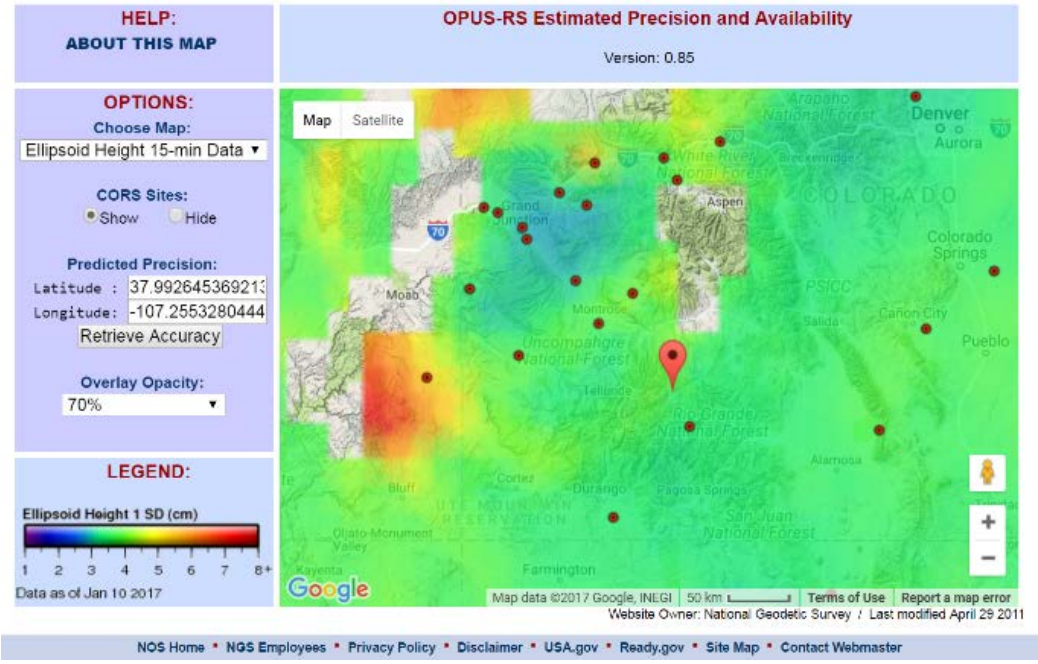

Figure 2-9 Accuracy of OPUS-RS results around the Lake City, Colorado. Top figure shows the horizontal accuracy, and bottom figure shows the vertical accuracy. The red marker indicates the landslide area. Red dots show the locations of surrounding CORS. The OPUS-RS method is not available at the blank areas.

2.2.5 Fine alignment of registration-MSA

Data registration based on corresponding points is swift and accurate; however, such an approach may have problems when there is an unstable reflector set-up, non-optimal reflector positioning, or when measurement errors exist. Multi-Station Adjustment (MSA) tries to solve those problems by modifying each scan position to calculate the best overall fit. The correspondence used by MSA can be tie points, tie objects, and/or tie point sets. The idea is to use several iterations of a least square fitting to calculate the best overall fit for all scan positions based on the tie points distance measurement, tie objects geometry measurement, and/or tie point sets ICP measurements, as shown in Figure 2-10.

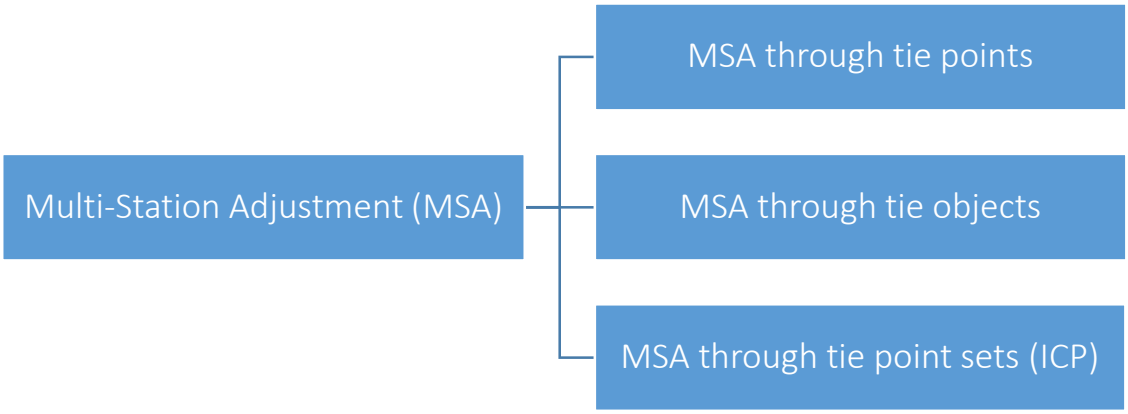

Figure 2-10 Multi-Station Adjustment for point cloud fine alignment.

The essential algorithm for MSA using tie point sets is the Iterative Closet Point (ICP) method. The ICP method estimates the point-to-point distances between different point sets. By minimizing that distance, this method can calculate the 6 degrees of freedom used in coordinate alignment. By minimizing the alignment error, the ICP method can register data by automatically searching for corresponding points (RIEGL, 2015). This method registers data by treating the point cloud as an entirety and matches the data by its overall shape. Assuming that two or more sampled point sets $(\boldsymbol{p_i}, \boldsymbol{q_i})$ need to be

registered, the rigid body transformation can be defined by rotation matrix $\boldsymbol{R}$ and translation vector $\boldsymbol{T}$, as shown in Equation (2-5):

$$\boldsymbol{q_i = Rp_i + T.} \tag{2-5}$$

Then, the Euclidean distance between the point sets can be computed; ICP calculates the transformation parameters by minimizing the distance

$$\boldsymbol{d = \sum_i (Rp_i + T - q_i)^2 \rightarrow min.} \tag{2-6}$$

The point cloud's coordinates are transformed and registered based on the transformation parameters calculated by the sampled point sets. Compared to corresponding points' registration, ICP broadens the registration requirements by using corresponding point sets. These corresponding point sets can be found at the overlapping scan areas between scan positions.

For the Slumgullion landslide area, the occlusion pattern of laser beams led to limited overlapping areas. These areas were difficult to estimate due to limited data coverage, which led to poor performance when performing ICP alignment. Meanwhile, overlapping areas could barely be recognized when the scan positions were far apart. Thus, only a few scan positions can use ICP as a compensated registration method if the corresponding points are not available or poorly performed.

Although ICP fails to accurately register scans taken at different scan positions during the same day, MSA's use of tie points is perfect for aligning scans from different days' measurements. To detect landslide changes using TLS data, projects taken from different days were combined into a master project. The master project was organized by a local reference frame set up using the geometry of tie points' reflectors mounted on the reference stations (BA, ML, MH, RL, RH). Tripods for the tie points were left on the

landslide throughout the survey, and reference stations BA, ML, MH, and RH proved to be stable compared to rovers inside the moving landslide mentioned in section 1.4. Using the MSA method, all scan positions were aligned at this local reference frame that maximized the overall fitting of tie points BA, ML, MH, RH. This local coordinate system is immune to GPS measurement uncertainties, since it does not require any GPS positions as input; the only uncertainty comes from the modeling of the reflector, which shares the same precision as the TLS fine scan. This local reference frame was ideal to monitor the landslide moment because it was detailed enough to depict the landslide movement during our one-week survey; thus, it was used in the point cloud-to-cloud comparisons for the earthflow detection.

2.3 Point Cloud Filter and Classification

After registration, the third step of our workflow was to filter and classify point clouds based on various attributes. Subsection 2.3.1 shows point cloud colorizing of the TLS datasets using the true color image taken from the camera collocated with the scanner. Terrain filter is presented in subsection 2.3.2; a unique water aliasing was found during the terrain filter at the sag pond area on the landslide.

2.3.1 Point cloud colorizing

Before filtering, point clouds can be colorized based on the true color images taken by the camera on top of the TLS scanner. This photography was optional after each scan session. After a panorama scan, the scanner rotated while the camera took a series of photos of the scanned area. The overlap of each image was set as 20% for our project and the exposure time and the aperture were set during calibration. Point clouds were colored based on the pixel values of the image. Points that were not captured in the photo were classified and could be removed. Removing uncolored point clouds is optional based on

different projects. For our project, all points were preserved while colorizing. The color information provides an intuitive way to visualize point clouds. Color information can also be used for classification or other processing. Figure 2-11 shows the panorama image combined from a series of photos taken at one scan position and the point cloud at the same location. Figure 2-12 shows the colored point cloud for the whole landslide area.

Figure 2-11 Panorama (top) taken at the Slumgullion landslide. Reflectance of point clouds for the same location (bottom).

Figure 2-12 TLS registration results colored by images taken by the camera collocated with the scanner.

2.3.2 Terrain filter

After registration, data were classified by terrain points and off-terrain points using a terrain filter. Point clouds of vegetation, rocks on the ground, and people were separated from points on the ground, which were used to process the digital terrain model (DTM) for the landslide area. The filter works in a hierarchical manner by filtering from coarse to fine at several levels of detail (LoD). An estimated ground surface was calculated based on the lowest point clouds. The distance from all points to this surface was calculated and used to classify the point cloud.

The filter generates a 2.5D point set with only one vertical component allowed for each XY location. For the Slumgullion landslide area, there were no overhanging-terrain. In addition, the terrain filter removed all the MTA aliasing because the MTA returns were located in the air, which were eliminated as off-terrain points. Figure 2-13 shows an example of the terrain filter.

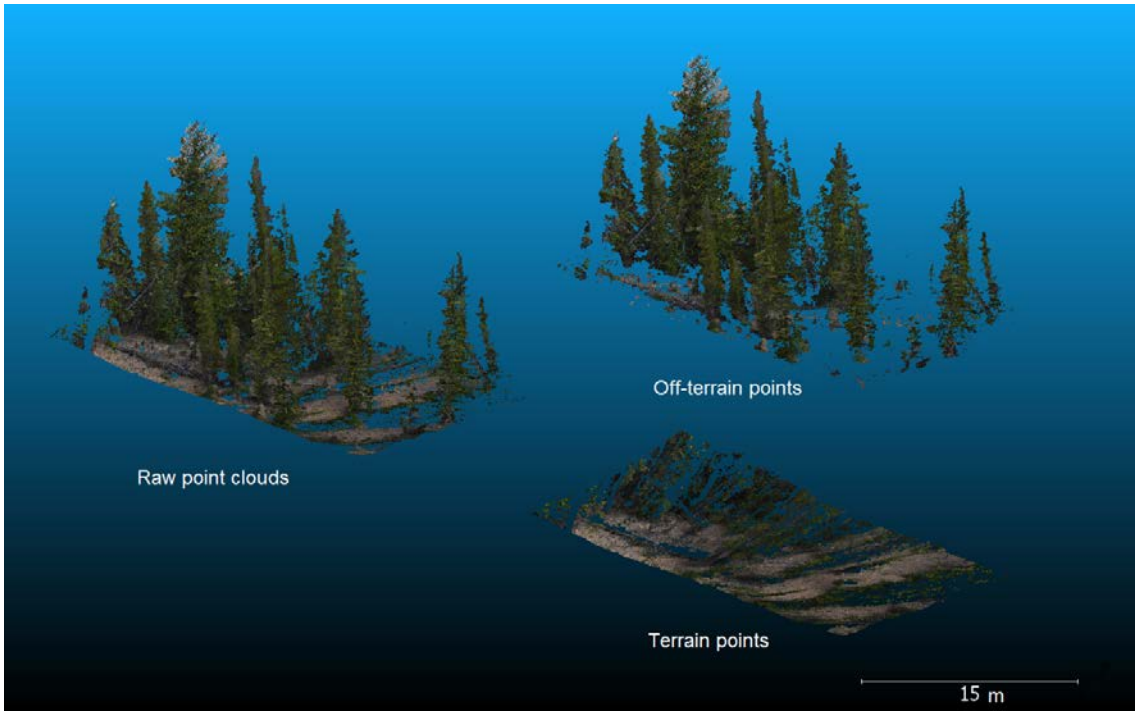

Figure 2-13 Point clouds before and after the terrain filter. The left part shows the raw point cloud. The right part shows the points that are classified as off-terrain points and terrain points.

The terrain filter is not omnipotent, especially when the survey area is in a complex environment. For example, there are sag ponds located at the Slumgullion landslide, as shown in Figure 2-14, where the still water surface works like a mirror. The reflected laser returns created a false illusion of the target beyond the sag pond. The mirror effect left a series of point sets beneath the ground surface, as shown in Figure 2-15. When using the terrain filter, the fake point beneath the ground was estimated to be the ground surface, and points above it were classified as off-terrain, which led to a misclassification of the terrain point sets. If no action was taken, the terrain filter could leave fake point sets below and cut a hole into the real terrain surface. This hole led to incorrect DTM interpolations, as shown in Figure 2-16.

Figure 2-14 Sag pond found on the Slumgullion landslide. Photo is taken by the camera on collocated with the TLS scanner. There were showers and intermittent rains on every survey day.

To prevent such aliasing, points beneath the ground should be eliminated before applying the terrain filter. Points beneath the ground were manually removed or removed by a mining filter that estimates the points below the ground surface. For our project, the area around the sag ponds was inspected manually, and points below the ground were eliminated before applying the terrain filter.

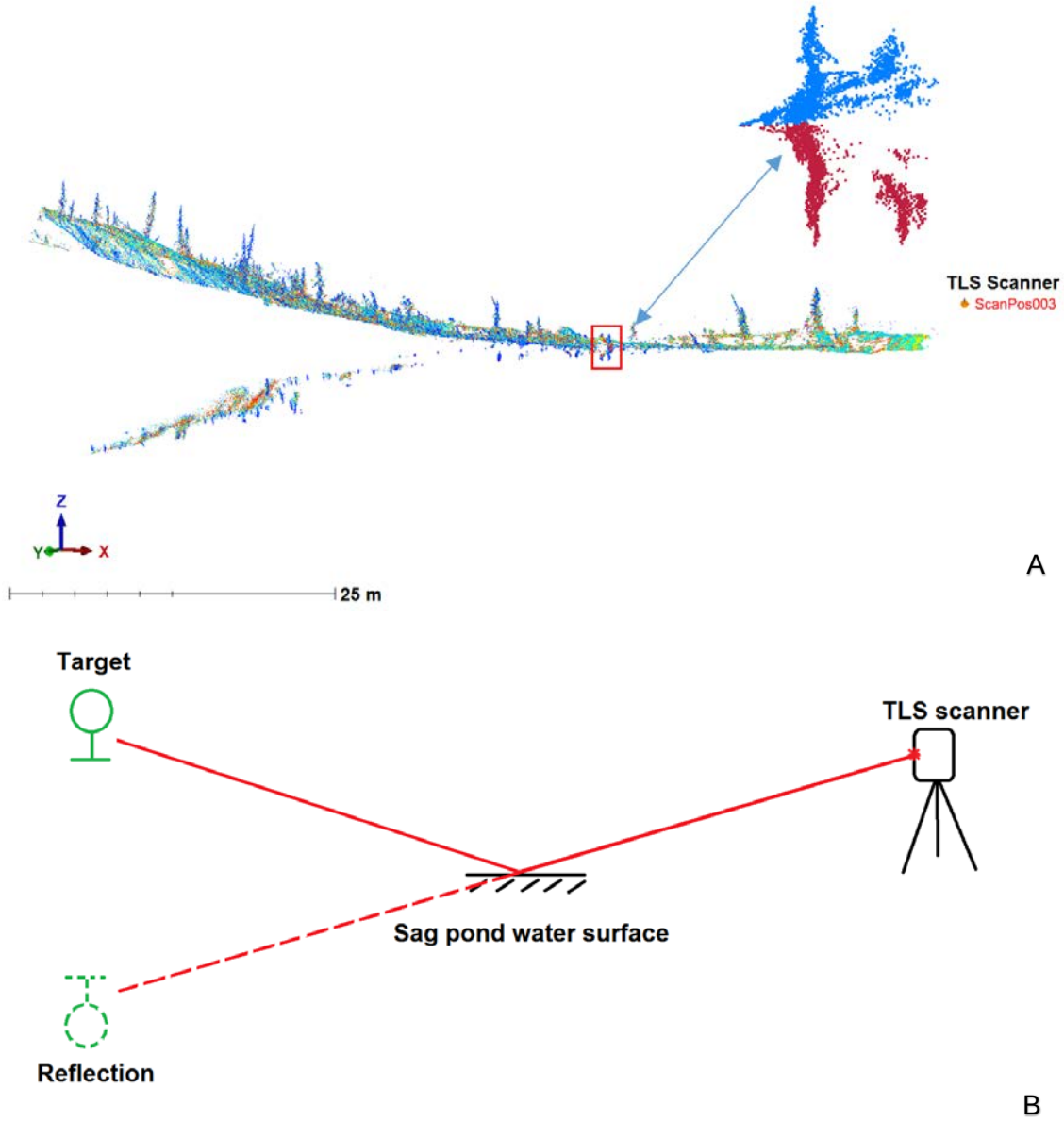

Figure 2-15 Water aliasing of laser measurements. (a) the mirror effect caused by water on the landslide; the point cloud under the ground indicates the reflection of targets on the ground; the zoomed-in look shows a sample of trees and their reflections. (b) a illustration of the reflected laser pass.

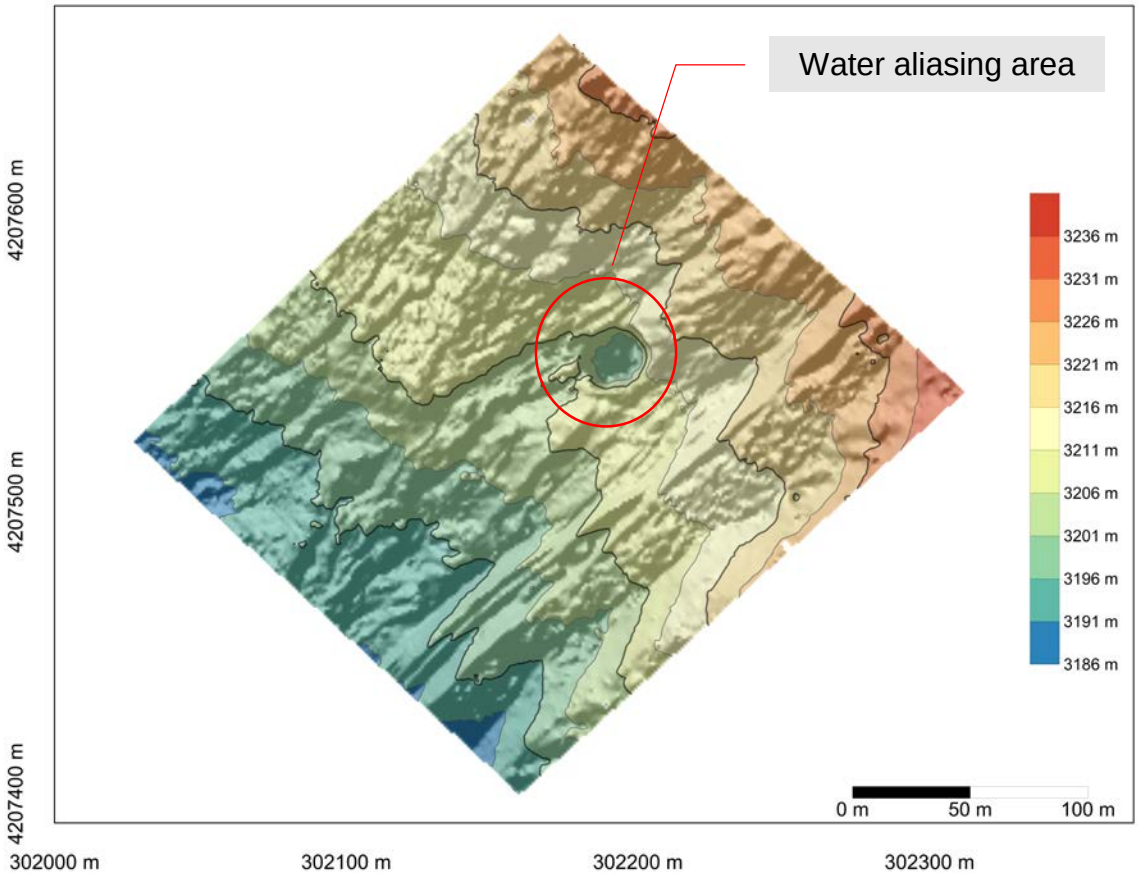

Figure 2-16 DTM interpolation error at the water aliasing area. Terrain filter cutting a hole at the water aliasing area on the interpolated DTM.

After the terrain filter, the point sets classified as terrain were combined into a bare earth model; the model was checked manually for outliers. Because of unevenly distributed points and occlusion patterns, the ground surface estimations may fail on the boundary of the data or in the area where raw data have gaps. As a result, the terrain filter fails in those areas and leaves any points above the ground as outliers. These outliers can be manually removed, and the result is a bare earth model. This model is a point cloud version of a digital terrain model (DTM), which uses point clouds to represent the ground surface.

2.4 Point Cloud Gridding

Sometimes point cloud density for TLS is so high that the point sets acquired by TLS are sufficient to represent the geometry of the object for the purpose of comparison (Girardeau, 2015). Nonetheless, the radial scan pattern and the occlusion of laser beams restricts data from properly representing the ground surface at places that are far from the scanner or blocked by rolling terrain. Therefore, interpolation is necessary to fill in holes where no points or not enough points are recorded. In this section, Kriging interpolation for TLS point cloud data is presented as the fourth step in our workflow.

Interpolation is a fundamental step in digital terrain modeling (Li et al., 2005). Since the terrain filter already generates a 2.5D point set represent surface of the ground, there was no need to pre-filter the Z component per each XY coordinate. The vertical component was resampled within each grid cells, and medians were selected as the input to the gridding so that outliers were eliminated from the data.

Choosing a gridding method depends on many factors as no general method fits in all situations (Fisher and Tate, 2006). For TLS point clouds, if data coverage is poor, gridding results will be unreliable regardless of the gridding method used; if data coverage is good, the results will be good no matter which gridding method is performed. This is due to the high point density character of TLS data (Shan and Toth, 2008). The gridding method used for our study was Kriging. Kriging is a geostatistical gridding method that optimizes interpolation based on regression against observed Z-values of surrounding data points. The method utilizes a variogram that depends on the spatial distribution of data rather than the actual values. It has been proven by Lloyd and Atkinson (2002) that the Kriging method is well suited to fill in gaps where above-surface features have been removed from the point cloud to obtain a DTM, as long as sufficient data are available around such gaps.

Nevertheless, researches continue to debate about the computational burden of Kirging TLS data. It can be advantageous in some instances when aiming to derive a digital terrain model from LiDAR data, but in many cases, simpler approaches, like the inverse distance weighting method, may suffice (Lloyd and Atkinson, 2002).

2.4.1 Variogram for Kriging method

The sliding mass is stretched and reshaped when it entered the narrowed landslide neck. This deformation could cause an anisotropy of the terrain. The anisotropy describes the directional dependence of the spatial correlation for the Z component of the interpolated data. In subsection 2.4.1, we analyzed the anisotropy of point clouds collected at the Slumgullion landslide.

To quantify the anisotropy, the DTM of our project on July 3rd was analyzed as a sample. Using the Surfer software package, we used a Power Model to fit the variogram to the landslide area. Characteristic parameters were calculated based on the variogram model. For the Power Model, the Sill was 87.91 m, the Length was 110 m, and the power was 1.5. The anisotropy analysis yielded a 2.3 anisotropy ratio and a 9.8˚ anisotropy angle, with 0˚ as east. Directional variogram plots with an angular tolerance of 30˚ and no bandwidth limit are shown in Figure 2-17.

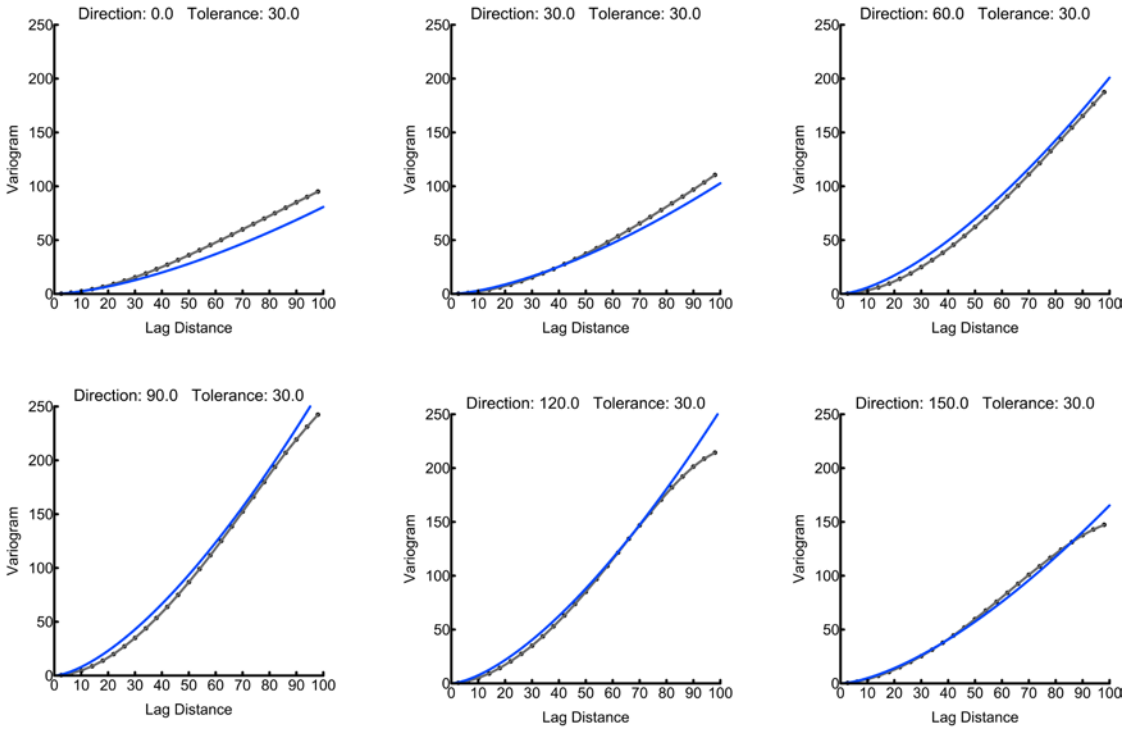

Figure 2-17 Variogram plots for Kriging method (0˚ as east).

Based on the variogram model, TLS data were gridded using the Kriging method. The grid size was 10 cm × 10 cm. No data were extrapolated beyond the exterior boundary of the landslide area.

2.4.2 DTMs derived from TLS and ALS

The Kriging gridding resulted in a rasterized DTM with 10 cm resolution for the data acquired by TLS on July 3rd and July 10th. ALS data collected by NCALM were gridded using the Surfer software package with 1 m spatial resolution; the result is shown in Figure 2-18..

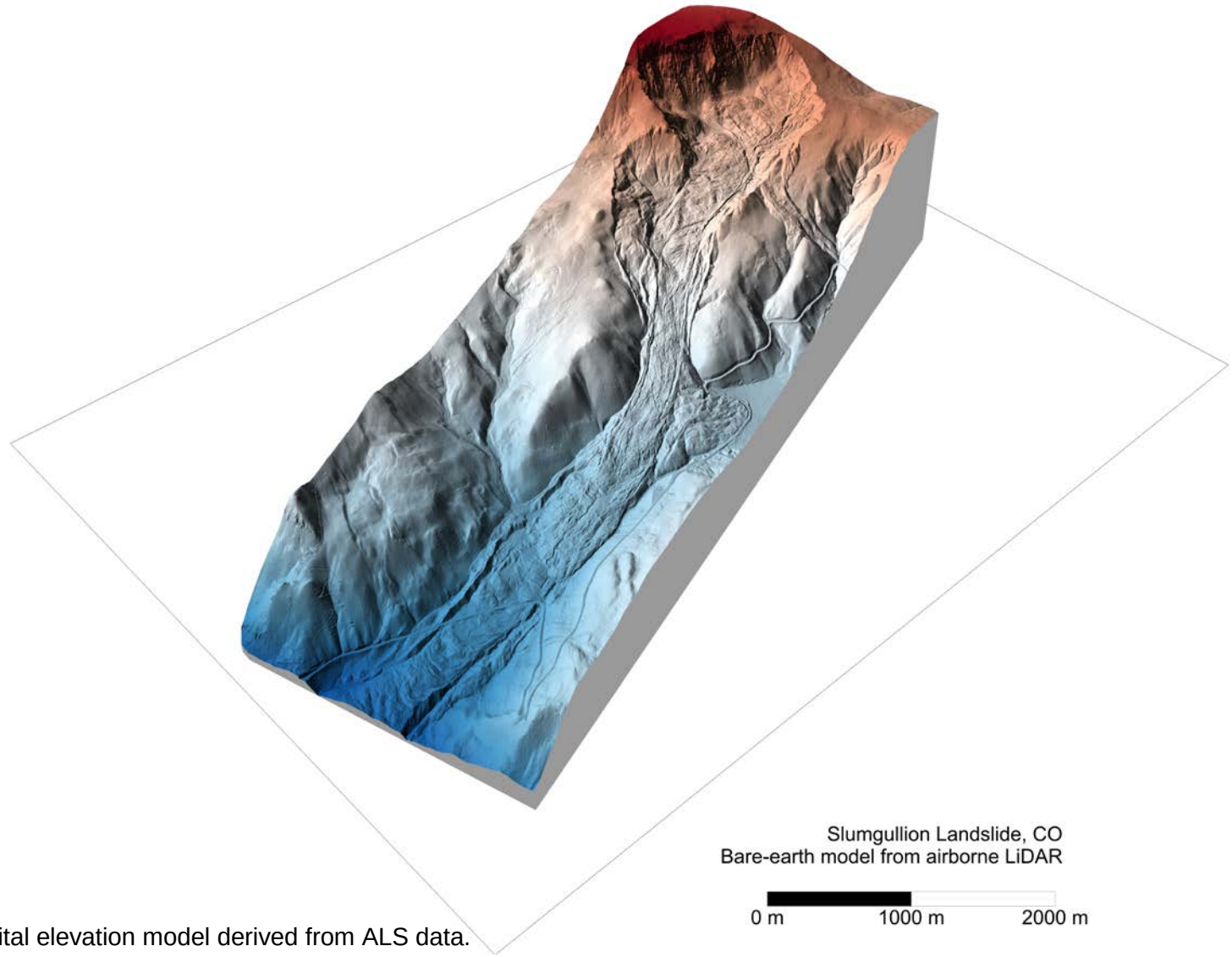

Figure 2-18 Digital elevation model derived from ALS data.

After gridding, data were ready to be used as a DTM representing the geomorphology of the Slumgullion landslide. The workflow for TLS DTM production is set up and summarized in Figure 2-19. Additional information related to topography can be derived using the DTM; for example, topography contours are shown in Figure 2-20. When joined with other measurements, a multiple attribute geological and geographic map can be generated.

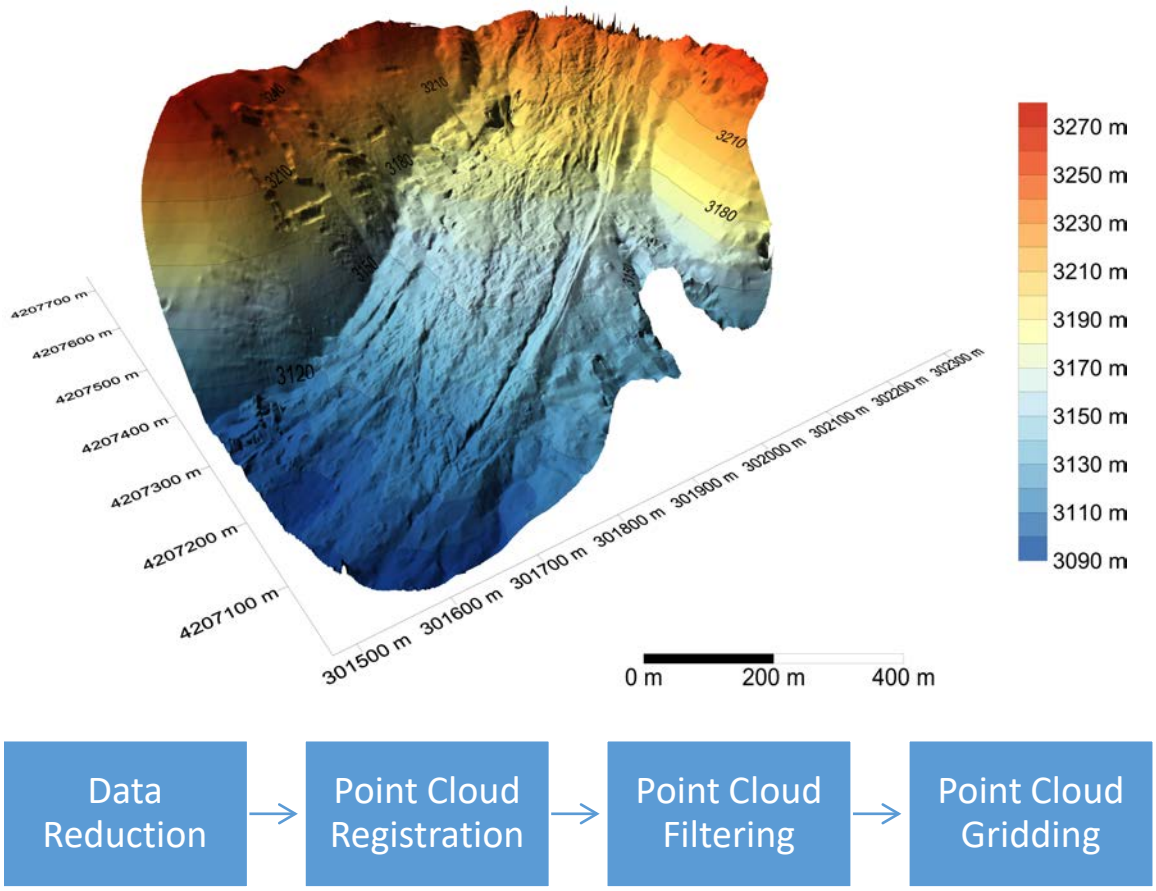

Figure 2-19 High resolution (10 cm×10 cm) DTM derived from TLS datasets for the active part of the landslide.

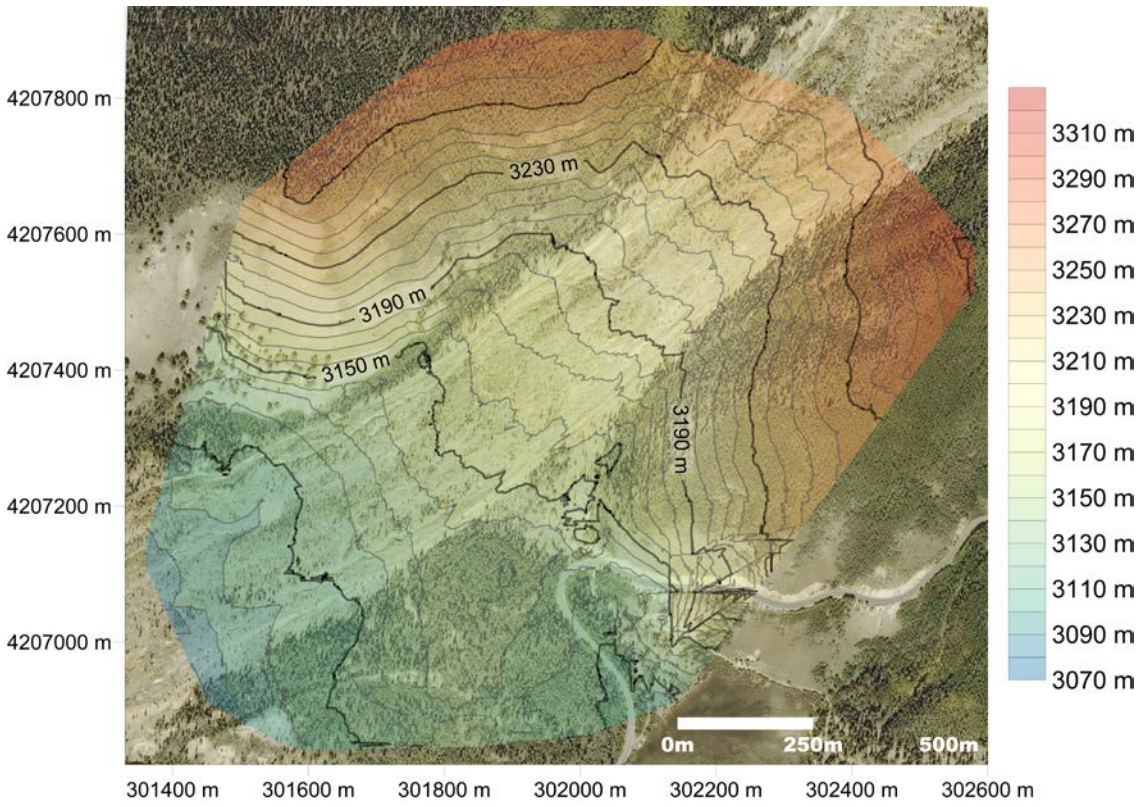

Figure 2-20 Contour information generated from the DTM illustrated in Figure 2-19.

3 Short-Term Topographic Change Detection for the Slumgullion Landslide

After processing the LiDAR data using the workflow described in Chapter 2, we organized the data by dates on which the project was conducted. The movement of the landslide was characterized by comparing project data collected from different days. Movement speed was calculated using data collected during the July 3rd project and July 10th projects.

Movement change detection for the Slumgullion landslide was conducted at three levels, as presented in the following section 3.1 through 3.3. The first tier detected movement based on the point measurements from GPS units. The second tier detected changes based on the raster differencing from the LiDAR DTMs. The third tier detected movement based on the octree-based point cloud-to-cloud distance from LiDAR point clouds.

3.1 Landslide Detection with GPS Measurements

Using GPS to detect movement changes takes advantage of the relative GPS positioning mentioned in Chapter 1. To start, baseline vectors between base station (BA) and the other GPS units were processed. Changes in the baseline vectors were then calculated to quantify the sliding motion of the Slumgullion landslide during our one-week survey.

3.1.1 Relative GPS positioning for the Slumgullion landslide

Baseline vectors ($\boldsymbol{\Delta X, \Delta Y, \Delta Z}$) were calculated between base station BA and other rovers spread along the landslide area (L0-L6). We used the Topcon Tools Software package to compute the baseline vectors with millimeter accuracy. The length of the baseline was extremely short, less than 500 meters, between the base station BA and the rovers, as listed in Table 3-1.

The baseline vectors collected from different days were compared to yields the baseline changes; the change of a baseline vector monitors the relative movement of a rover on different days by referring to a stable base (BA). The baseline changes were plotted using the Coplot Software package and showed in Figure 3-1.

Table 3-1 Baseline vectors for the rovers at the Slumgullion Landslide. Each baseline is named as ‘base-rover’ style. The Starting Time and the duration of each observation are recorded. The distance from the base to the rovers is decomposed into three components, the north-south (dN), the east-west (dE), and the vertical directions (dHt). The measurement uncertainties are recorded within the one sigma range. The baseline length (3D dis.) and the duration of the observation window is recorded.

Name	Start Time	dN (m)	dE (m)	dHt (m)	Horz. RMS (m)	Vert. RMS (m)	3D dis. (m)	Duration
BA−L0	7/10/2015 13:13	-103.537	-248.989	-37.085	0.001	0.001	272.305	8:59:45
BA−L0	7/8/2015 15:30	-103.538	-248.956	-37.088	0.001	0.001	272.275	6:38:30
BA−L1	7/10/2015 12:58	34.001	-91.946	-3.863	0.001	0.001	98.147	9:28:50
BA−L1	7/3/2015 17:03	34.052	-91.859	-3.852	0.001	0.001	98.083	5:07:00
BA−L1	7/7/2015 12:45	34.025	-91.913	-3.854	0.001	0.001	98.125	8:56:55
BA−L2	7/8/2015 15:52	68.358	-29.268	6.19	0.001	0.001	74.647	6:13:40
BA−L2	7/7/2015 15:29	68.381	-29.272	6.193	0.001	0.001	74.671	6:56:20
BA−L2	7/5/2015 17:09	68.384	-29.24	6.193	0.001	0.001	74.661	6:14:20
BA−L3	7/5/2015 15:39	106.723	36.676	12.526	0.001	0.001	113.588	7:33:50
BA−L3	7/8/2015 15:44	106.697	36.647	12.522	0.001	0.001	113.555	6:31:10
BA−L4	7/5/2015 15:45	195.411	87.01	22.079	0.001	0.001	215.131	7:27:20
BA−L4	7/8/2015 15:29	195.383	86.981	22.07	0.001	0.001	215.094	7:06:45
BA−L5	7/5/2015 15:24	240.913	143.034	37.995	0.001	0.001	282.855	8:03:00
BA−L5	7/8/2015 15:28	240.884	142.999	37.992	0.001	0.001	282.811	7:03:10
BA−L6	7/5/2015 16:04	409.19	399.216	83.943	0.001	0.001	578.039	7:22:30
BA−L6	7/8/2015 15:49	409.157	399.175	83.932	0.001	0.001	577.986	6:23:20

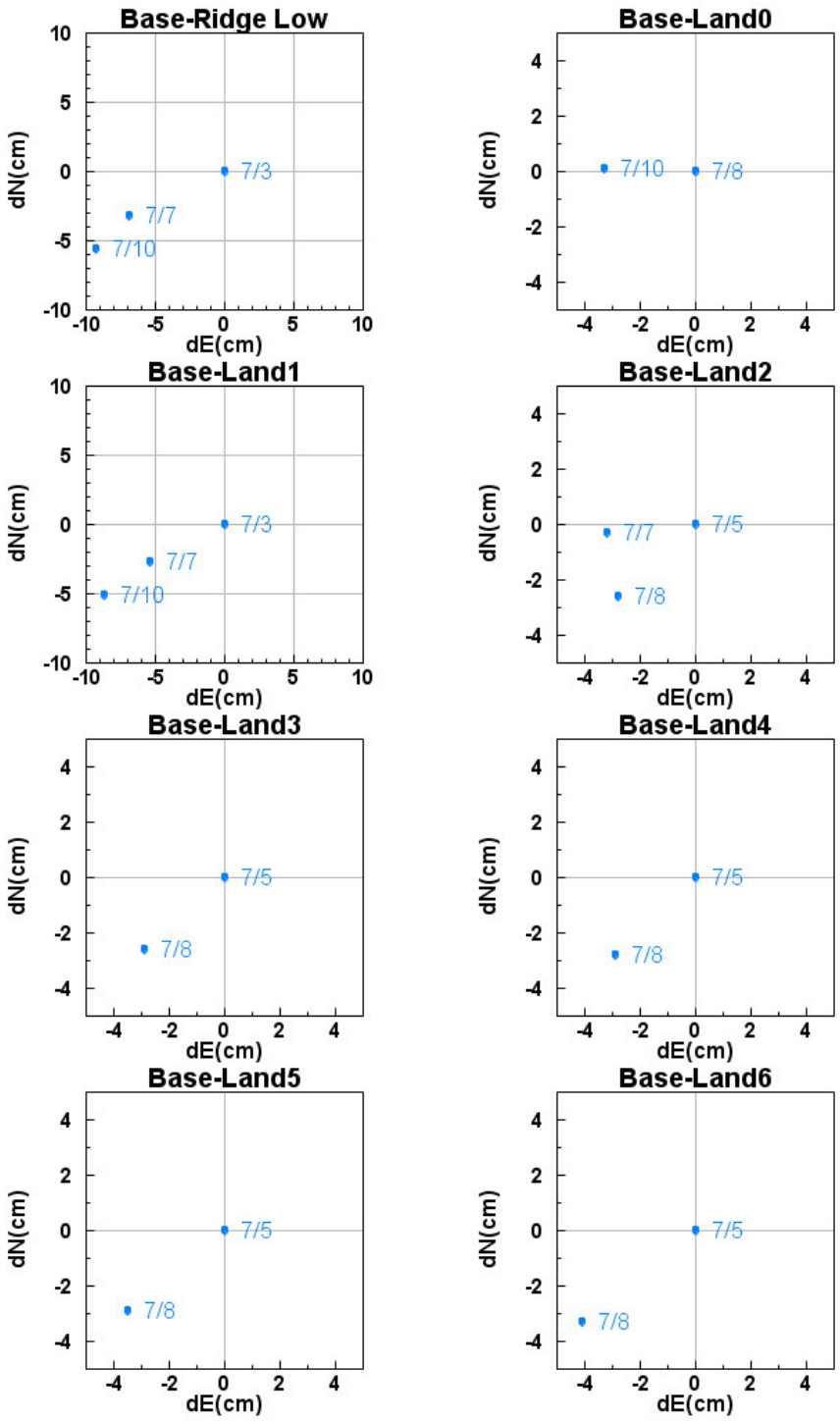

Figure 3-1 Changes of the GPS baseline vectors. Changes were normalized by the first day's measurements located at the origin. Displacement from the origin represents the relative motion of a rover referring to the base station (BA).

Figure 3-1 shows baseline changes derived using relative GPS positioning. Each rover (L0-L6) refers its position to the base Station (BA), and the baseline distance obtained from different days was then normalized based on the first day's measurements. The plot represents the change in distance referring to the first-day measurements. Figure 3-1 shows the baseline change of the horizontal components. Each square grid represents a movement of 5 cm along its side.

Using the information in Figure 3-1, the overall landslide movement direction and speed were calculated. Figure 3-2 presents the overall movement of the landslide measured by GPS units.

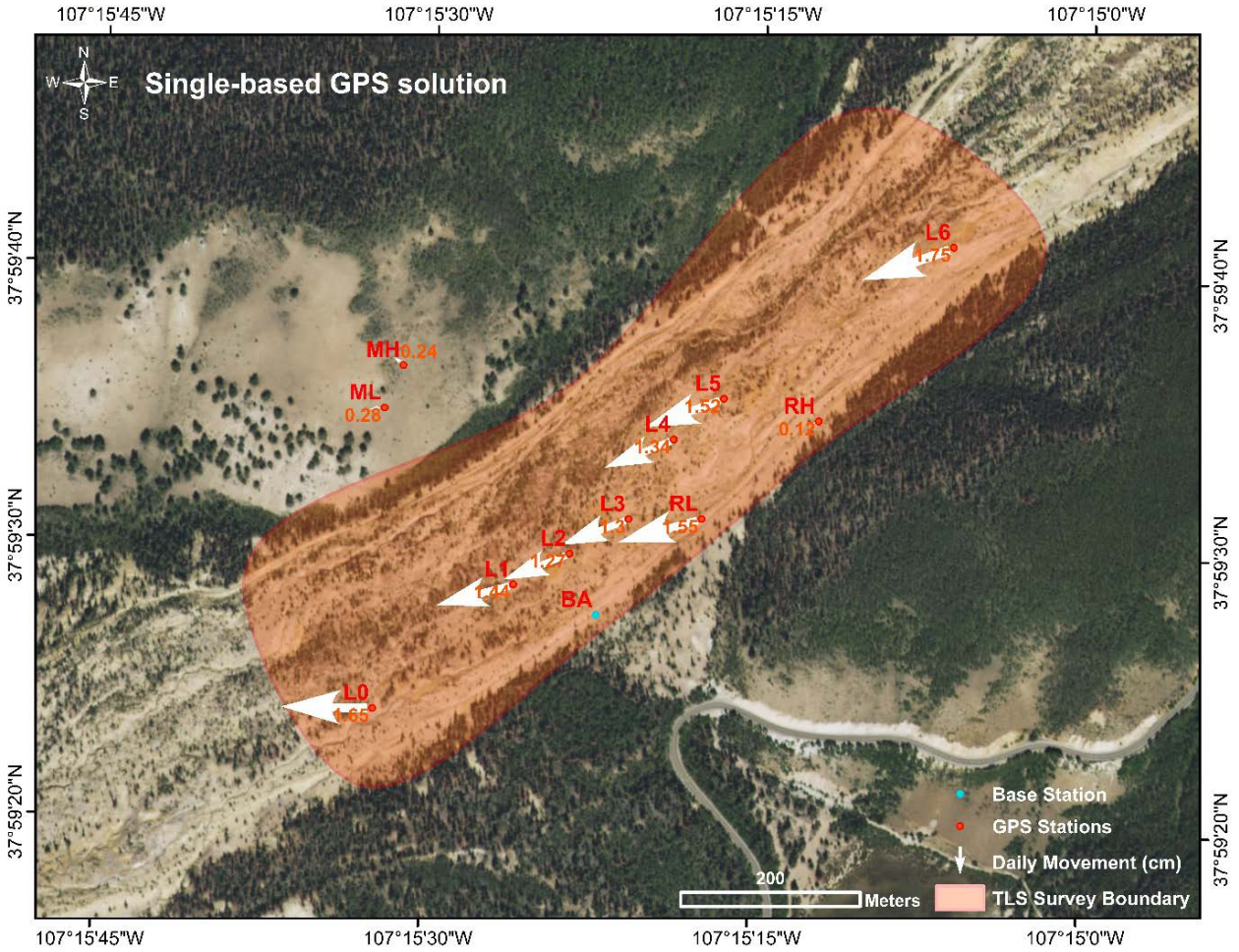

Figure 3-2 Landslide movements detected by GPS units. Arrow orientation represents movement direction; size and number represent the speed (cm/day).

Figure 3-2 shows the positions of six GPS stations (L0-L6) that were calculated from a single-based (BA) GPS solution. Introduced in Chapter 1, single-based GPS solutions are able to obtain an accuracy of under 5 mm horizontally and 15 mm vertically (Wang, 2011). The average daily movement detected by the GPS units during our survey was about 1.5 cm. The rovers were moving in the southeastern direction along with the landslide; their daily displacement are listed in Table 3-2. The daily displacement for reference stations RL, RH, ML, and MH are listed in Table 3-3.

Table 3-2 Daily displacement rates of the rover stations derived from baselines.

Baseline	N(cm/d)	E(cm/d)	Horz.(cm/d)	Vert.(cm/d)	3D(cm/d)
	Base (BA) - Landslide monitoring site (L0-L6)				
BA−L0	0.05	-1.65	1.65	0.15	1.66
BA−L1	-0.73	-1.24	1.44	-0.16	1.45
BA−L2	-0.87	-0.93	1.27	-0.10	1.28
BA−L3	-0.87	-0.97	1.30	-0.13	1.31
BA−L4	-0.93	-0.97	1.34	-0.30	1.38
BA−L5	-0.97	-1.17	1.52	-0.10	1.52
BA−L6	-1.10	-1.37	1.75	-0.37	1.79
Average	-0.77	-1.18	1.47	-0.14	1.48
SD	0.38	0.26	0.18	0.17	0.19

Table 3-3 Daily displacement rates of the reference stations derived from baselines.

Baseline	N(cm/d)	E(cm/d)	Horz.(cm/d)	Vert.(cm/d)	3D(cm/d)
	Base (BA) - Reference (RL, RH, ML, MH)				
BA−RL	-0.80	-1.33	1.55	-0.24	1.57
BA−RH	0.07	0.10	0.12	-0.03	0.12
BA−ML	-0.06	-0.27	0.28	-0.03	0.28
BA−MH	-0.23	0.03	0.24	0.07	0.24

3.1.2 Stability of base GPS station (BA)

As mentioned in subsection 3.1.1, relative GPS positioning process used a single baseline solution in which all the GPS stations referred their position to a single base station BA. Therefore, the stability of the base station was crucial for accurately measuring baseline changes. In this subsection, we proved the stability of the base station BA.

Stability of the base station BA was analyzed at two levels. First, stability of base station (BA) was analyzed by referring to the other GPS stations ML, MH, RL, and RH which were located outside the landslide. Second, stability was examined referring to local CORS in order to monitor its global coordinate displacements.

Reference GPS stations ML, MH, RL, and RH were located at the stable boundaries on both sides of the landslides. Therefore, a reference to these locations was able to prove a stable base station. Using the same relative positioning method mentioned in subsection 3.1.1, we inspected the baselines connecting base station BA and other reference stations ML, MH, RL, and RH.

Table 3-4 shows the baseline vectors processed with the Topcon Tools Software package, and records the relative displacement between the base station and the other reference stations. Based on the results listed in Table 3-4, the baseline changes for the BA-Reference GPS pairs were calculated; the change is plotted in Figure 3-3.

Table 3-4 Baseline vectors for the reference stations (MH, ML, RH, RL) at the Slumgullion Landslide. Each baseline is named as 'base-reference' style. The Starting Time and the duration of each observation are recorded. The distance from the base to other reference stations is decomposed into three components, the north-south (dN), the east-west (dE), and the vertical directions (dHt). The measurement uncertainties are recorded within the one sigma range. The baseline length (3D dis.) and the duration of the observation window is recorded.

Name	Start Time	dN (m)	dE (m)	dHt (m)	Horz. RMS (m)	Vert. RMS (m)	3D dis. (m)	Duration
BA−MH	7/7/2015 13:05	278.443	-214.132	50.796	0.001	0.001	355.057	8:45:00
BA−MH	7/10/2015 14:19	278.436	-214.131	50.798	0.001	0.001	355.052	8:51:15
BA−ML	7/10/2015 14:03	231.166	-235.248	28.932	0.001	0.001	331.219	9:04:45
BA−ML	7/3/2015 18:00	231.17	-235.229	28.934	0.001	0.002	331.209	1:00:00
BA−ML	7/7/2015 12:52	231.172	-235.247	28.932	0.001	0.001	331.223	8:48:05
BA−RH	7/7/2015 12:44	215.625	248.569	44.755	0.001	0.001	332.225	8:55:20
BA−RH	7/10/2015 13:55	215.627	248.572	44.754	0.001	0.001	332.228	9:13:45
BA−RL	7/7/2015 12:45	106.796	118.018	16.011	0.001	0.001	160.034	9:04:20
BA−RL	7/10/2015 12:58	106.772	117.994	16.008	0.001	0.001	160	10:09:55
BA−RL	7/3/2015 14:03	106.828	118.087	16.025	0.001	0.001	160.108	8:03:45

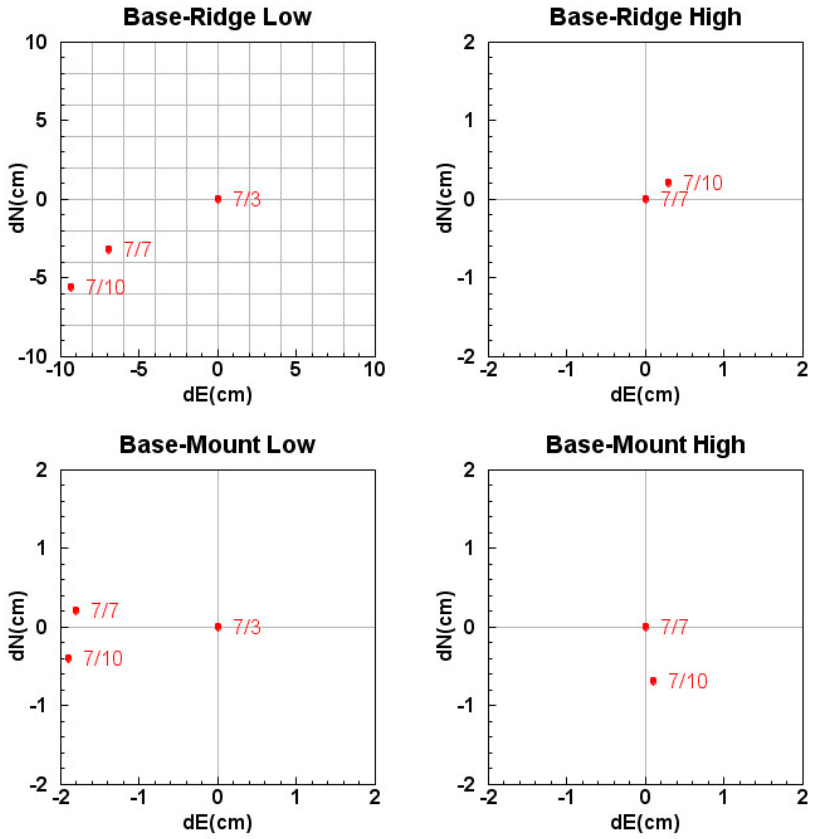

Figure 3-3 Baseline changes for the BA-Reference GPS pairs. The baseline vectors shown are connecting base station with other reference GPS stations, including RL, RH, ML, and MH. Each square grid represents a 2 cm movements along its side.

Comparing Figure 3-1 and Figure 3-3, the reference stations RH, ML, and MH show no coherent movements; neither the direction nor the magnitude of movement was apparent enough to calculate the trend of the sliding motion. Compared to rovers L0-L6 on the landslide, which had baseline changes of up to 10 cm, the baseline change for each reference station RH, ML, and MH was below 2 cm during the one-week survey. Direction changes were coherent for the rovers, while the direction changes for RH, ML, and MH

were random. The data proved that the base station BA and other reference stations RH, ML, and MH were quite stable compared to the moving landslide.

Reference station RL proved to be unstable exception. There was a 10 cm movement toward the southeast, similar to the rovers inside the landslide; this shows an unstable reference station moving along with the landslide. Movement speed and direction were comparable to the rover stations, as shown in Figure 3-2. Movement speed of reference station RL is calculated in

Table 3-3. The instability of the reference station RL may have been caused by mistakenly setting up the GPS on the wrong side of the ridge along the shear zone created by the rapidly moving landslide.

In addition to comparing the baseline vectors between the base and other reference stations, the position of the base station can also be compared using its global position with referenced the local CORS. Data were processed using OPUS, and the position of the base station was referred to the local CORS. In Table 3-5, the displacement referring to the first day's measurements is calculated.

Table 3-5 Global positions of the base station (BA) (UTM zone 13N). Displacement is normalized to the first day's observations.

Date	Easting(m)	dE(cm)	Northing(m)	dN(cm)	EL Height NAD83 (m)	dVert. (cm)
07/03/15	301883.797	0.0	4207217.886	0.0	3151.805	0.0
07/05/15	301883.793	-0.4	4207217.901	1.5	3151.794	-1.1
07/07/15	301883.814	1.7	4207217.881	-0.5	3151.784	-2.1
07/08/15	301883.800	0.3	4207217.897	1.1	3151.783	-2.2
07/10/15	301883.817	2.0	4207217.891	0.5	3151.793	-1.2
Average	301883.804	0.9	4207217.891	0.6	3151.792	-1.3

As listed in Table 3-5, the average displacement of the base station over one-week survey was about one centimeter. We can conclude that the base station was quite stable compared to the moving landslide, which had more than 10 cm of cumulative horizontal displacement from July 3rd to July 10th. Displacement referring to the first day's measurement is plotted in Figure 3-4.

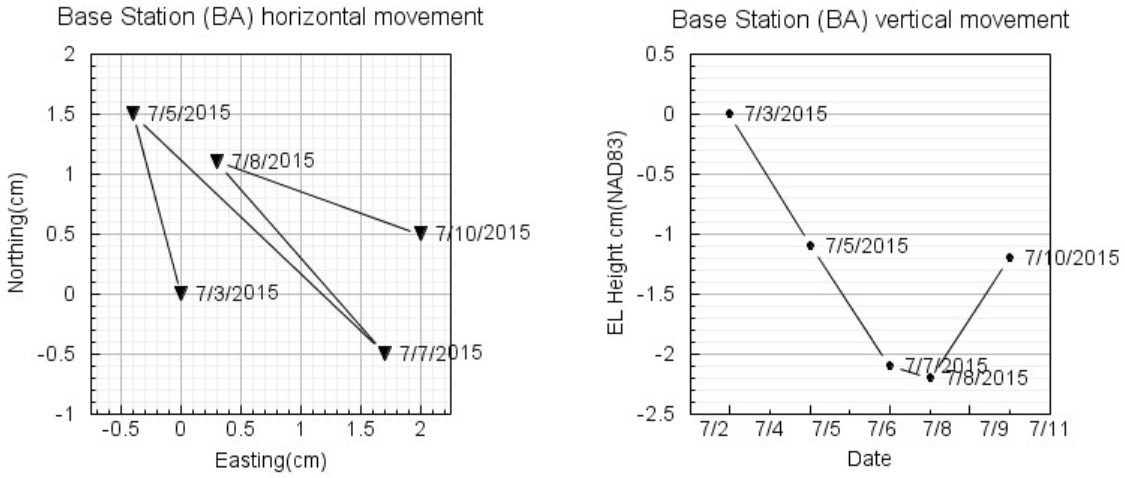

Figure 3-4 Relative displacements of base station (BA) referring to its first measurement on July 3rd, 2015.

From Figure 3-4, there is no trend for the base station's movement. The maximum displacements for all components were smaller than the measurement uncertainties of the GPS units. The maximum measurement uncertainties for the base station position were approximately 2 cm for the horizontal components and 3 cm for the vertical component.

3.2 Landslide Detection with LiDAR DTMs

Movement detection in 2D utilizes the raster differencing at the pixel level. This method is broadly used for raster data analysis from pixel-based sensors like cameras, and multispectral or hyperspectral scanners. This method begins by setting up raster models

that represents the compared objects. The models are then compared at the pixel level to yield the changes of the target area. In the following subsection, we presented two raster based comparison methods revealing movement of the Slumgullion landslide.

For the Slumgullion landslide area, we filtered the TLS and ALS point cloud data representing the bare earth surface. After the gridding process, the data were interpolated within the landslide area where a 2.5D surface was generated as the Digital Terrain Model (DTM). The grid unit in the DTM works similarly to the pixels collected from a camera sensor. The point cloud is transformed into a standard raster format so that all the compared data conform to the same grid size and cover the same area. The TLS data were then compared using a grid resolution of 10 cm×10 cm; the ALS data were compared using a grid resolution of 1 m×1 m. After this transformation, raster models collected from different days were analyzed using the following two methods.

3.2.1 Differential of DTM (DoD)

The first method we used is called the Difference of DTMs (DoD). This method is commonly used for large scale planar scene comparisons. Two DTMs are compared by subtracting one from the other on a pixel-by-pixel basis. The comparison results yield the difference between vertical components for each pixel or grid. Only the common areas between two DTMs are compared. This technique is convenient for computing the contrast between two raster models.

From Figure 3-5, the comparison results from the differential ALS shows no apparent displacement between data collected from July 3rd to July 10th. No movement trend was observed at the landslide area.

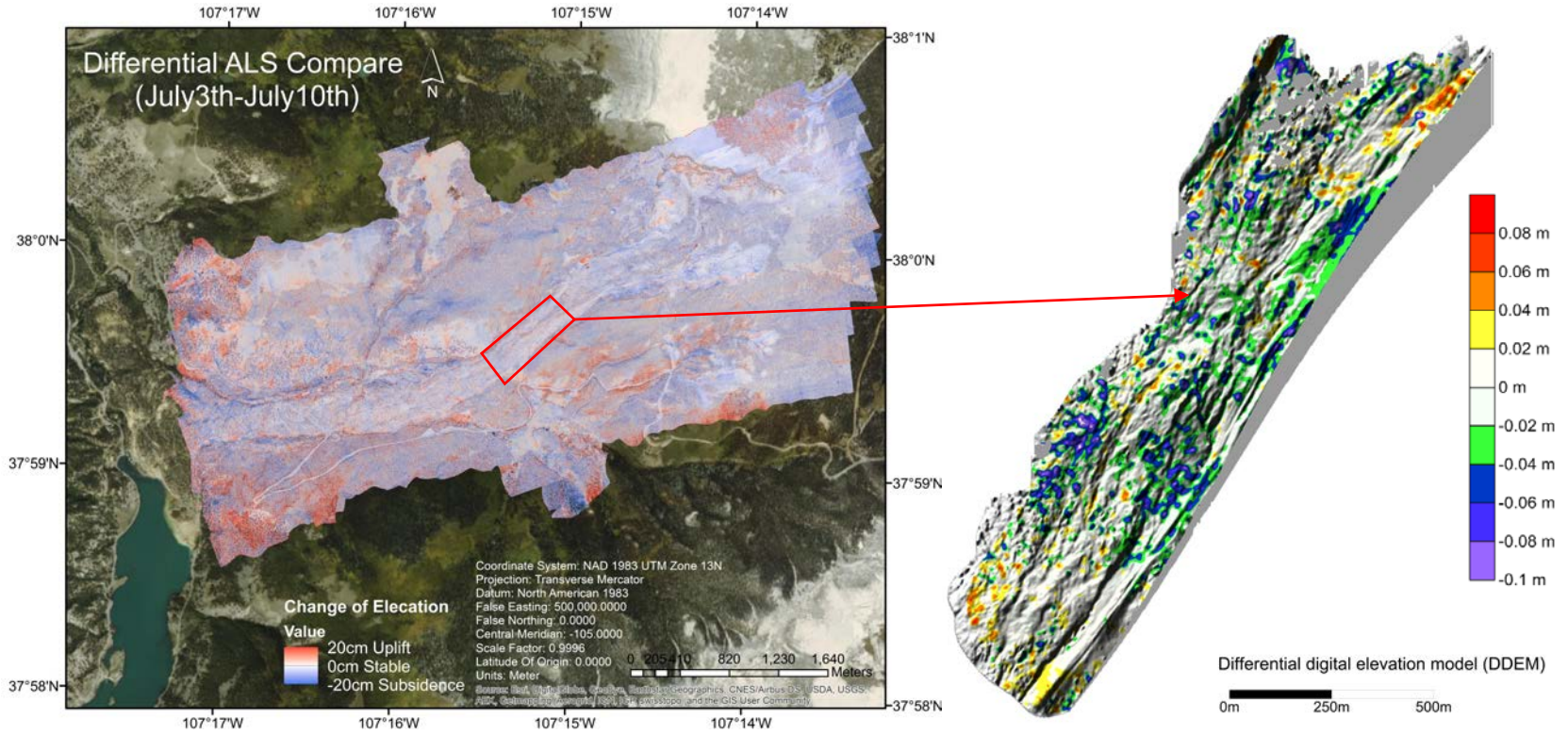

Figure 3-5 (Left) Differential of DTMs result derived from the repeated ALS surveys between July 3rd and 10th, 2015 for the whole landslide area. Processed by ArcMap software, warmer colors indicate an increase in elevation; cooler colors shows a decrease in elevation.

Figure 3-6 (Right) Differential of DTMs result derived from the repeated TLS surveys on July 3rd and 10th, 2015 for the active part of the landslide area. Processed by Surfer software, warmer colors indicate an increase in elevation; cooler colors shows a decrease in elevation. DoD results derived by TLS data has higher resolution than the results derived by ALS data.

From Figure 3-6, most of the landslide was stable, showing no color in the DoD result calculated from TLS datasets. The statistics of the differenced Z component is listed in Table 3-6.

Table 3-6 Statistics of the differenced Z component for DoD method.

Total Nodes:	1299540	Mean:	-0.009465372
Z		Median:	-0.00699464
Count:	151047	Root Mean Square:	0.027731946
1%-tile:	-0.078074405	Trim Mean (10%):	-0.008993662
5%-tile:	-0.055775723	Interquartile Mean:	-0.007699703
10%-tile:	-0.043915751	Midrange:	-0.03366793
25%-tile:	-0.024761081	Winsorized Mean:	-0.009189678
50%-tile:	-0.00699464	TriMean:	-0.007971523
75%-tile:	0.00686427	Variance:	0.000679472
90%-tile:	0.021089044	Standard Deviation:	0.026066685
95%-tile:	0.031042657	Interquartile Range:	0.031625352
99%-tile:	0.049236195	Range:	0.36153935
Minimum:	-0.214437605	Median Abs. Deviation:	0.015590775
Maximum:	0.147101745	Average Abs. Deviation:	0.020108525

The DoD method failed to reveal the landslide process compared to the GPS measurements for various reasons. The average slope of the landslide is small, around 8˚. According to previous studies be Coe et al. (2003), the total movement of the Slumgullion landslide (combined horizontal and vertical movements) was largely dominated by the horizontal component. Given a small slope, the vertical change of the landslide could hardly be detected from one week of data. The DoD method compares the

Z component of the raster; therefore, it is sensitive to the vertical change of the DTM. It is not sensitive to horizontal change unless the horizontal shift causes a vertical difference.

Uncertainties of GPS measurements were at the centimeter level for the vertical component, and the beam divergence for TLS yielded a 3 cm measurement uncertainty for every 100 m range increase. Although relative GPS positioning can provide 15 mm vertical accuracy (Wang, 2011), the vertical component changes, as listed in Table 3-2, still fall outside the level of detection. Therefore the variation of the vertical component can hardly be detected from the DTM georeferenced by GPS.

The radial scan pattern and laser beam occlusion yielded an unevenly distributed point cloud. The interpolation on such poitn clouds introduced uncertainties in the gridding results. Furthermore, the common grid size for each DTM imposed a limit to the level of detail held within the raw point cloud data. This limitation restricted the gridded data to be shown at different morphological scales. Within the 10 cm grid size, the vertical component was averaged, therefore, insensitive to changes that are under 10 cm.

The rapidly changing slope and aspect in Figure 3-7, together with the rapid horizontal displacement of the terrain, mitigated the real differences in terrain elevation. The short-term change of the Slumgullion landslide during our survey behaved like a translational slide where the moving mass of the landslide consists of a small region moving downslope as a relatively coherent part. Pixel-by-pixel comparison does not trace the corresponding target; therefore, it can not trace the coherent sliding pattern of the translational slide. On the other hand, GPS can trace the landslide movement because the tripods were left on the landslide and moved with the sliding mass. In one-week period, movement of the landslide can be monitored by GPS measurements, but can hardly be detected by this method.

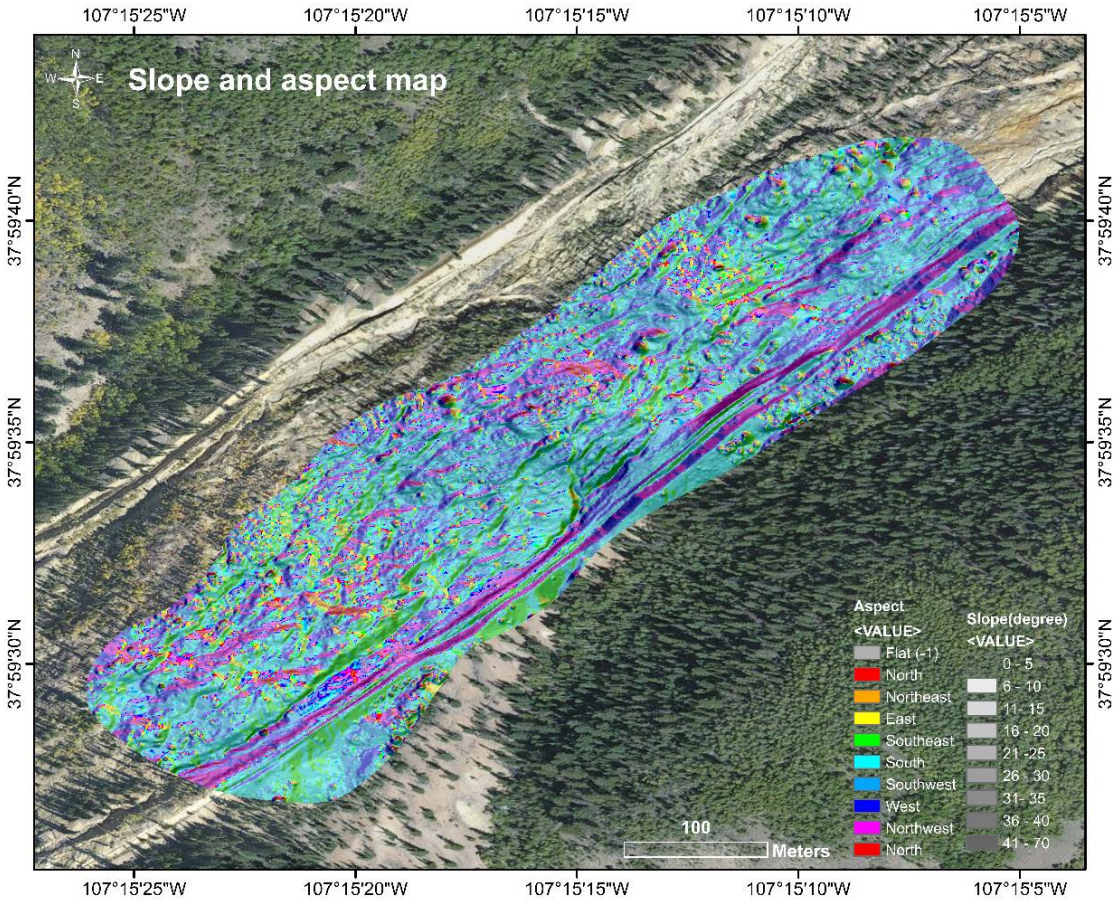

Figure 3-7 The slope and aspect calculated from the TLS DTM. The ridge that separated the active and inactive part of the landslide is in pink located in the diagonal direction.

3.2.2 Edge detection

The second method is called edge detection. This method is broadly used in digital image processing. Edges of the image from one scene are characterized and then compared to edges processed from another scene. For this study, DTMs collected from July 3rd to 10th were processed with their edges plotted on the same map. Landslide changes can be identified where the edges of two DTMs do not overlapped.

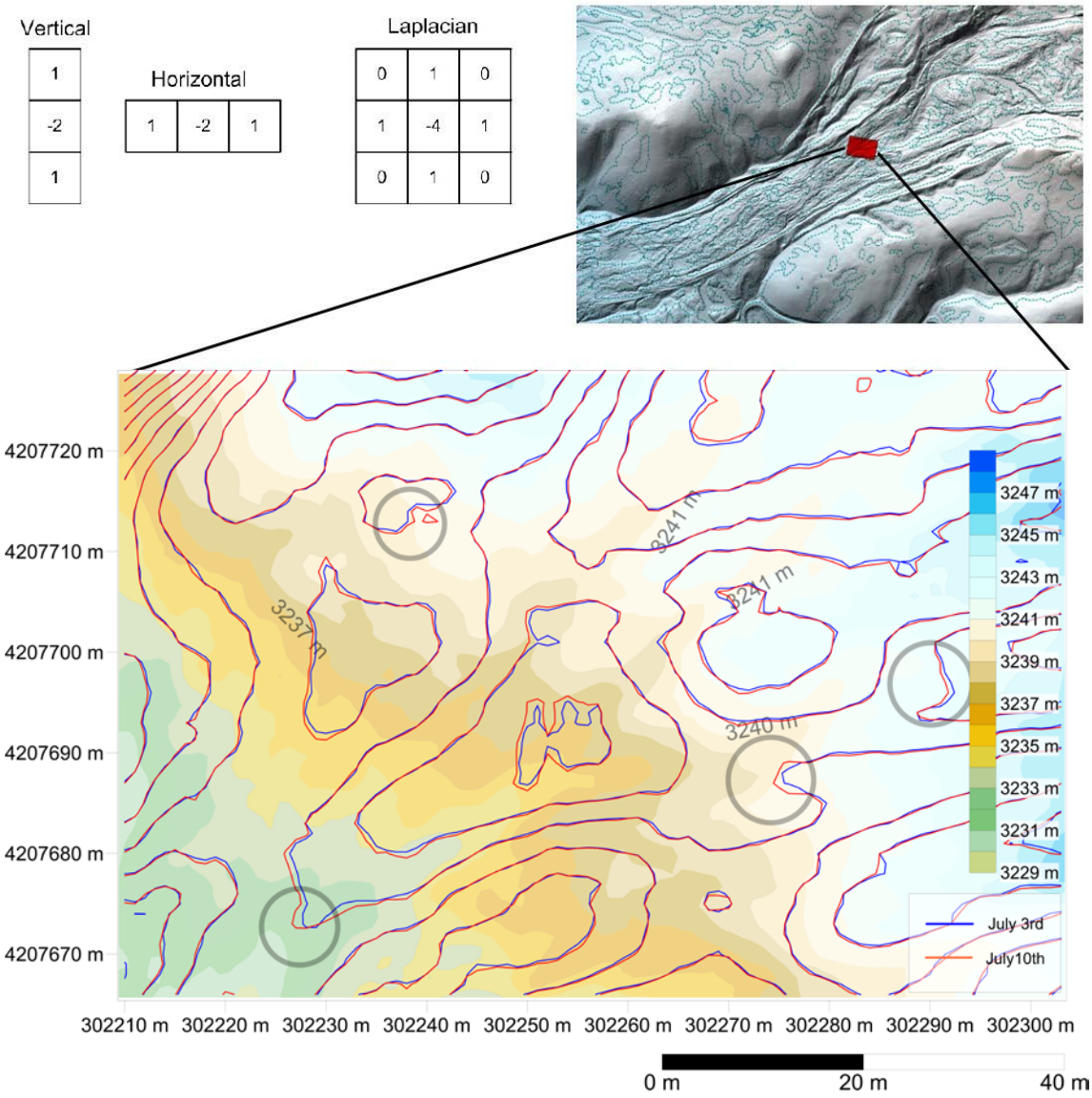

Figure 3-8 Edge detection method using ALS datasets. The circled area shows that edges of topography shifted toward the southeast direction during one-week survey.

The edge of the DTM is characterized by a Laplacian filter. We chose the Laplacian operator because it is the lowest order rotation-invariant partial derivative operator. This means the edge is characterized in all directions so that the changes of the edges can be depicted in all directions.

To get the edge of the DTM, gridded DTMs were filtered to remove any noise in the original raster. Then, a 5×5 Gaussian filter was applied to the gridded data that filtered out any high-frequency noise, caused by cliffs or hang overs in the terrain. The first-order Laplacian filter shown in Figure 3-8 was applied to generate the DTM edges. Data edges acquired from July 3rd and July 10th were then plotted together to show any changes. In Figure 3-8, the change of edges shows the landslide moving toward the southeast direction.

The edge detection worked fine when coherent movement occurred on the landslide that the whole landslide shifted to one direction without substantial shape changes. This is possible in the short term observations of a fast-moving landslide. During one-week survey, the morphological change of the landslide was only visible at the edge of the terrain where the newly formed territory created new edges compared to the old DTM. Edge detection is sensitive to such change; therefore, we tested it as a method to derive the short-term movement of the Slumgullion landslide.

From the edge detection results, only a few places showed a sliding motion. The edges detected from July 3rd and July 10th were, in general, overlapping, thereby showing no movement. The method failed to detect a general landslide movement for the following reasons. First, such limited morphological changes happened during our one-week survey that the horizontal sliding was too small to be detected. Second, in order to derive an edge, a low pass filter was used to smooth out the DTM. Change of the DTM might be mitigated due to this filtering process. Third, the one-meter grid size for ALS data was too large to depict accurate edge positions and to compare the sliding motions within one week.

Other drawbacks to edge detection are that it cannot accurately quantify the movements and that it requires full data coverage of the compared area. Because of occlusion patterns,

the DTM collected from TLS was too noisy to be processed using this method; only ALS datasets were tested using this method.

3.3 Landslide Detection with Cloud-to-cloud (C2C) Comparison

The point density collected by TLS was so high that sometimes there was no need to interpolate or extrapolate the data to represent the morphologic characters of the natural surface. Three-dimensional point cloud change detection has the advantage of being able to calculate changes in both horizontal and vertical directions (Lague et al., 2013). For that reason, 3D point cloud-to-cloud (C2C) comparison was used in our study. In this chapter, subsection 3.3.1 briefly introduces the octree-based distance calculation that can be applied to point cloud-to-cloud comparison; subsection 3.3.2 presents the computation of Hausdorff distance; and subsection 3.3.3 analyzes TLS datasets collected from the Slumgullion landslide.

3.3.1 Octree-based distance calculation

Point cloud comparison detects changes by calculating the distance between the compared point sets. The distance is calculated using an octree structure. Repeated subdivision of the octree enables a tree structure when storing and processing data. The root of the tree is the bounding box of all point clouds. Sibling cubes share the same parent cube, and the smallest cubes are called leaf nodes. With this tree structure, sibling cubes contain adjacent point clouds with the same scale, as shown in Figure 2-2. The tree structure and coding method make it easier to search for adjacent-point sets and their neighbors at different octree levels. This makes it perfect for similar scaled neighboring point cloud comparison (Girardeau et al., 2005).

There are some prerequisite conditions for point cloud comparison. First, the two point sets must share the same coordinates and scale. Both the coordinates and scale can be

unified during the registration and georeferencing processes. Second, the starting bounding box should contain all the compared point sets. The assumption is that homologous point sets lie in the same level of octrees so that the compared point sets happen to be homologous. Third, the geometry is well represented by the compared point clouds, therefore, full spacial coverage is required. TLS has an extremely dense-point cloud, as shown in Figure 3-9; thus, a C2C comparison can be performed directly on raw TLS point cloud. Therefore, TLS datasets are used in C2C comparisons without a terrain filter. Outliers and distorted measurements are removed manually after applying a deviation filter. Because ALS data have a 50 cm × 50 cm resolution, which is too sparse to calculate changes at the 10 cm level, it is not used for the cloud comparison.

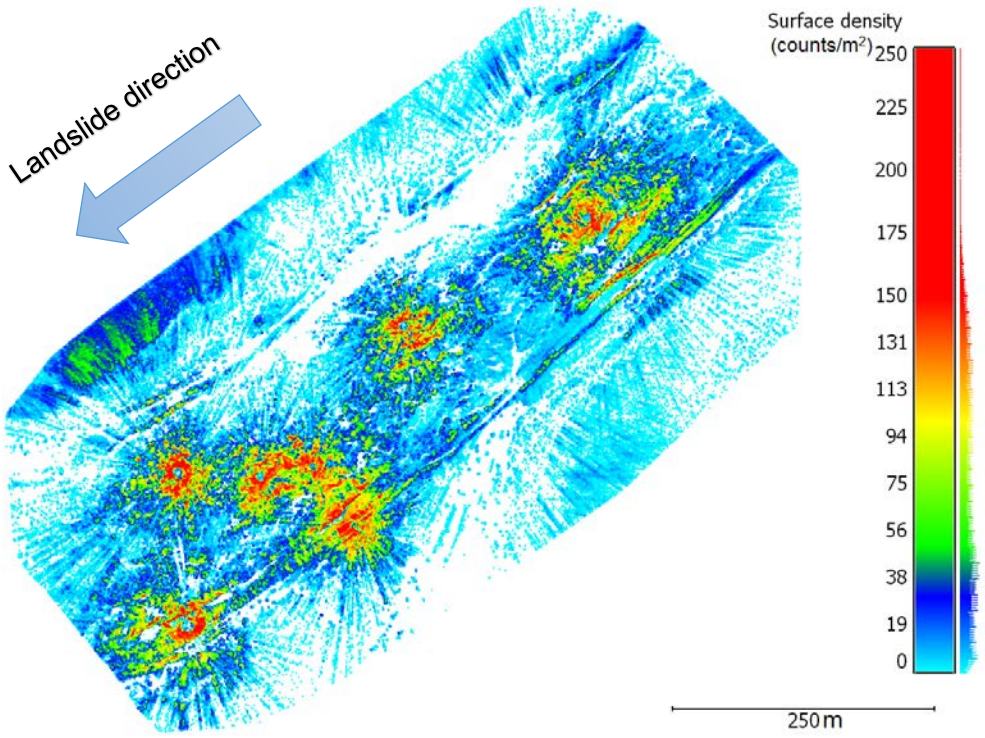

Figure 3-9 Point cloud density for TLS measurements (counts/m^2). The point cloud shows the TLS data collected on July 10th.

In our study, a local coordinate was set up using the tie point positions of reference stations MH, ML, RH, and BA. Data were aligned using the Multi Station Adjustment (MSA) function introduced in the workflow. Tie points from July 7th were set as a reference. Other tie points, collected on July 3rd and 10th, were registered to the reference using MSA.

There are many strategies for octree-based comparisons. Basic methods include average distance computation, best-fitting plane orientation computation, and Hausdorff distance computation. Advanced comparison strategies improve the process by: 1) changing the searching methods for homologous point sets; 2) using the local normal distance instead of Cartesian distance; and 3) enhancing the stability of the algorithm when point sets contain outliers or with different roughness, point densities, or coverage. Several cloud comparison strategies have been invented for natural surface 3D comparisons (e.g., Lague et al., 2013). For our project, we used the Hausdorff distance computation method employed by the CloudCompare Software package to calculate the 3-D point cloud-to-cloud distance.

3.3.2 Hausdorff distance

The Hausdorff distance measures how far apart two point clouds are from each other. For example, compared point sets A and B are defined by $\boldsymbol{a_i} \in \boldsymbol{A}, \boldsymbol{b_j} \in \boldsymbol{B}$, where $\boldsymbol{i}, \boldsymbol{j}$ is the number of points within each set. The minimum Euclidian distance D between two sets is shown in Equation (3-1 below

$$D(A,B) = \min_{a_i \in A}\left\{\min_{b_j \in B}\left[d(a_i, b_j)\right]\right\}. \tag{3-1}$$

With a similar definition, Equation (3-2 computes the Hausdorff distance h as

$$h(A,B) = \max_{a_i \in A}\left\{\min_{b_j \in B}\left[d(a_i, b_j)\right]\right\}. \tag{3-2}$$

This definition of the Hausdorff distance is asymmetric, i.e. $h(A,B) \neq h(B,A)$; thus, a more general definition of Hausdorff distance is generated in Equation (3-3

$$H(A,B) = max[h(A,B), h(B,A)]. \quad (3\text{-}3)$$

Cloud-to-cloud comparison takes advantage of the dense point clouds collected by TLS. It calculates the Hausdorff distance between the compared point sets. A sample of the computed cloud-to-cloud distances is shown in Figure 3-10.

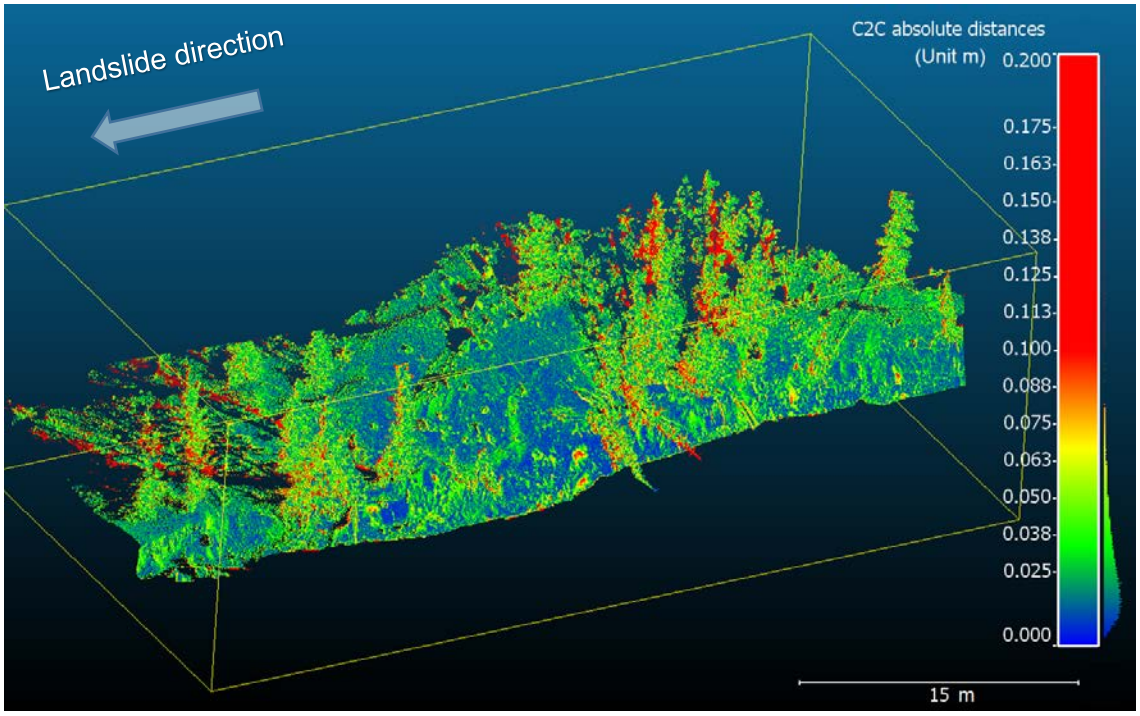

Figure 3-10 Point cloud comparison result from the July 3rd to July 10th project. Landslide changes are shown in color. Cooler colors represent closer point-to-point distances, and warmer colors represent larger point-to-point distances. This view was taken near the left ridge inside the landslide.

In Figure 3-10, point cloud sets are compared between projects collected between July 3rd and 10th. Figure 3-11 shows a histogram of the cloud-to-cloud distances. From the histogram, we see a continuous displacement ranging from zero displacements to 15 cm.

The results do not necessarily correspond to the real landslide movements. To depict the landslide movement from the C2C comparison results, further analysis was required and presented in subsection 3.3.3.

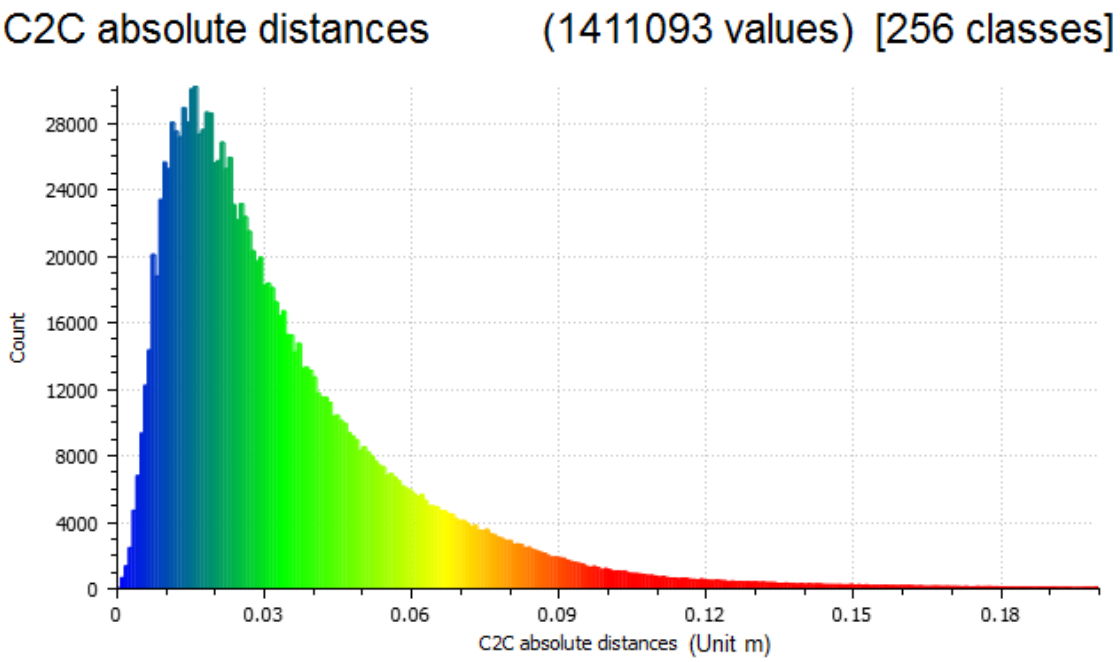

Figure 3-11 Histogram of the point cloud-to-cloud (C2C) distances.

3.3.3 Landslide movement detected from C2C results

To depict landslide movement from our cloud-to-cloud (C2C) comparison results, we had to zoom into the meter scale and sort the C2C distances into three categories: Stable, Coherent, and Collapse. This classification helps distinguish translational landslide movements from other geomorphological changes that happened in the short-term.

During our one-week survey, no dramatic geomorphological changes occurred, and landslide movements displayed more translation than rotation or collapse. A translational slide could happen in a style that the moving mass of the landslide consists of a single unit, or a few closely related units, or even a small region that move downslope as a

relatively coherent mass, as shown in Figure 3-12. According to our GPS survey, different locations on this translational slide shared roughly a 10 cm horizontal speed during the one-week survey. To monitor this translational movement, the comparison scale that we chose had to be small enough to witness a change at the 10 cm level; the translational landslide movement was isolated as the coherent category detected from the C2C result.

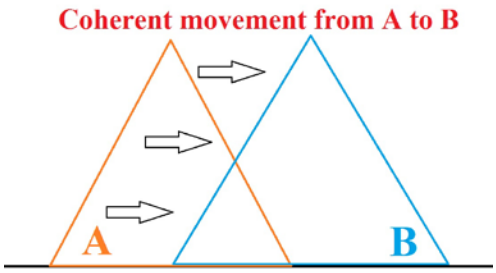

Figure 3-12 Illustration of a coherent movement.

From our GPS measurements, vertical movement during the one-week survey was less than 2 cm, and the average slope of the landslide was less than 8˚. The small vertical movement and the mild slope caused the compared point clouds to overlap or to become parallel in the vertical direction. If two compared clouds overlapped or were parallel in the vertical direction, the sliding motion, dominated by a horizontal shift, may have been mitigated or even ignored by the C2C detection. Because the compared point sets are not necessarily to be homologous or correlated, we categorized the parallel and overlapping areas by classifying them as the “stable” parts of the movement for the purpose of isolating the translational movement, as shown in Figure 3-13.

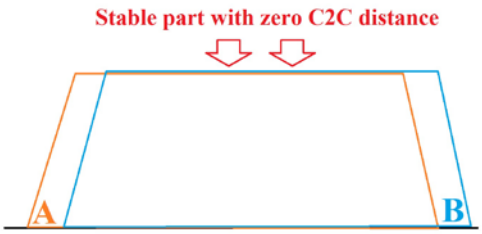

Figure 3-13 Illustration of a stable part.

A region where C2C distances are extremely large is defined as a collapse. A collapse can be caused by dramatic geomorphological changes, or it can be due to a deficiency in

the compared point sets or due to a partially absence of the compared point clouds, as shown in Figure 3-14.

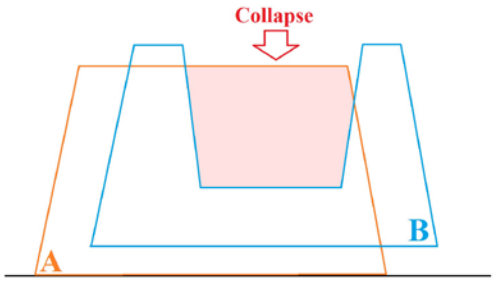

Figure 3-14 Illustration of a collapse.

From the C2C results, the stable part was where barely any distance existed between the compared point clouds. There are two possible explanations for undetectable distances: 1) no movement happened, or the change was too small to be detected by TLS; 2) translational movement happened, but the compared point sets overlapped or were vertically paralleled, and therefore no district contours exist. An example of the overlaps of the compared point sets is shown in Figure 3-15. From this figure, the maximum distance between the compared point sets is under 3 cm. The overall compared results for the Slumgullion landslide indicates that the displacement calculated by the C2C method for the stable category was under 3 cm, which already reaches the minimum detection level of TLS.

Translational motion detected from the C2C results was evident at the edge of the target. Inside the landslide, such a target can be a tree trunk, a big rock, or the steep surface of the trench created by the shearing effect of the landslide. Translational motion detected from tree branches and leaves was unstable due to wind or other anthropic reasons. Taking the rock shown in Figure 3-16 as an example, translational movement can be found on the edges facing the moving direction of the landslide. Maximum displacement was under 10 cm. Under full data coverage, a rock can be found shifted showing active displacements, and the intersection of the compared point clouds showed no distance detected by the C2C comparison, as shown by the blue line in the middle of Figure 3-16.

Among the three categories we created, the coherent displacement is the category that most closely related to the real motions of the landslide. The coherent displacement recorded a translational movement shared by the moving mass. After comparison, the range for translational movements was from 3 cm to 10 cm from July 3rd to 10th.

The collapse detected by the C2C method had an apparent shape change, and the distance between the compared point sets was significant. Displacements of more than 10 cm were found at the collapsed parts. The collapse can be a real change of the surface induced by natural or anthropic reasons, or it can caused by a deficiency in the compared data; a deficiency can be a result of laser occlusions or oblique scan angles. Extremely large distances are generated from C2C if part of the compared point cloud sets is missing.

By comparing the results derived from GPS and LiDAR, we concluded that as the dimension of comparison increased, the spatial information monitored in the change detection increased; however, the position correlation between the reference data and the compared data decreased. Therefore, there is a tradeoff between how detailed the detection is versus how closely the detected components correspond. This means that GPS measurements can provide accurate landslide movements as point records, but they cannot represent the overall trend or movement fields of the landslide area. Similarly, while LiDAR can depict movement patterns with cloud-to-cloud comparison, the detection results lack target correlations.

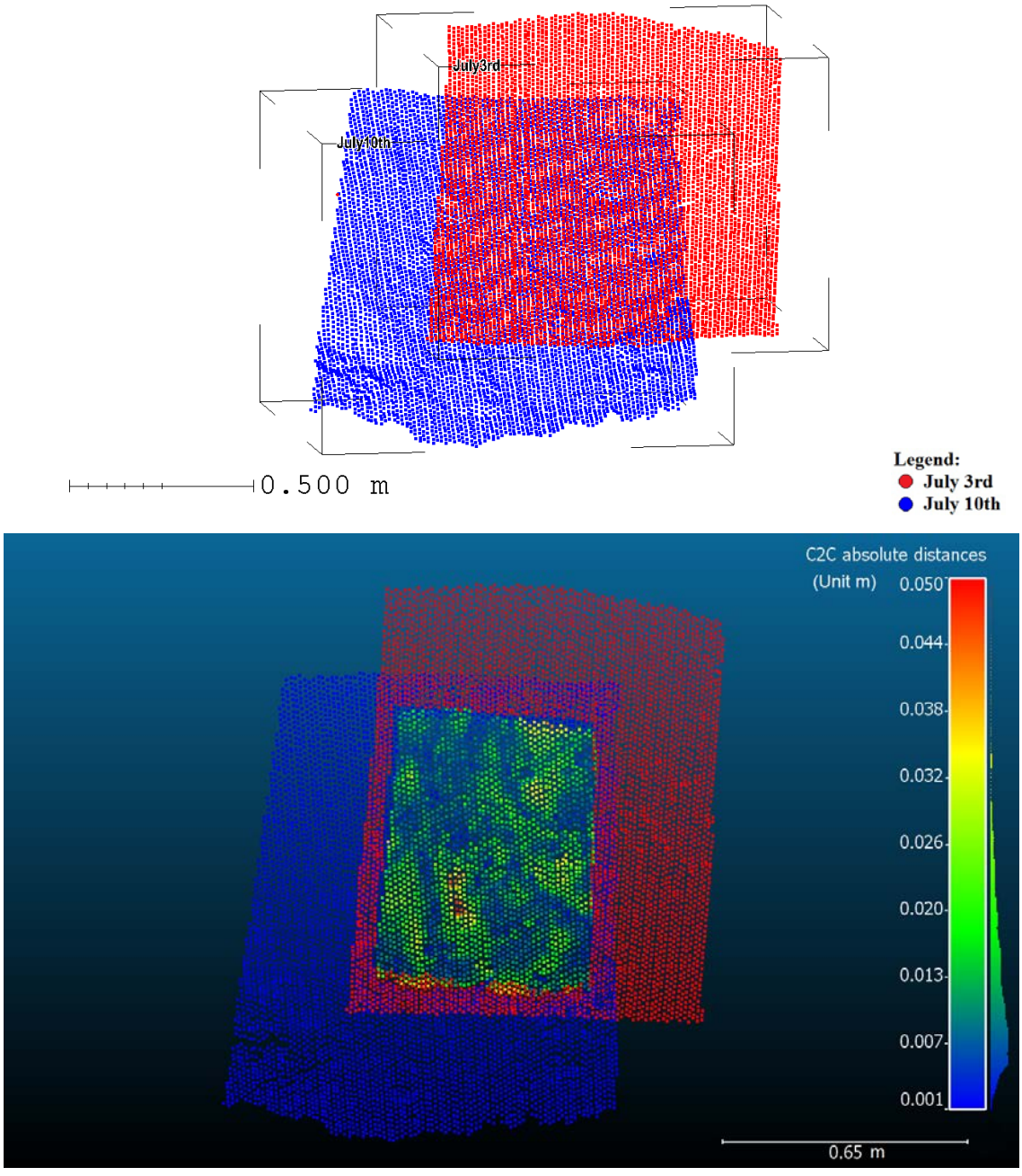

Figure 3-15 Stable part detected by C2C comparison. The top figure shows the point clouds being compared. The bottom figure shows C2C distances by color. The maximum distance is under 3 cm between the compared point sets.

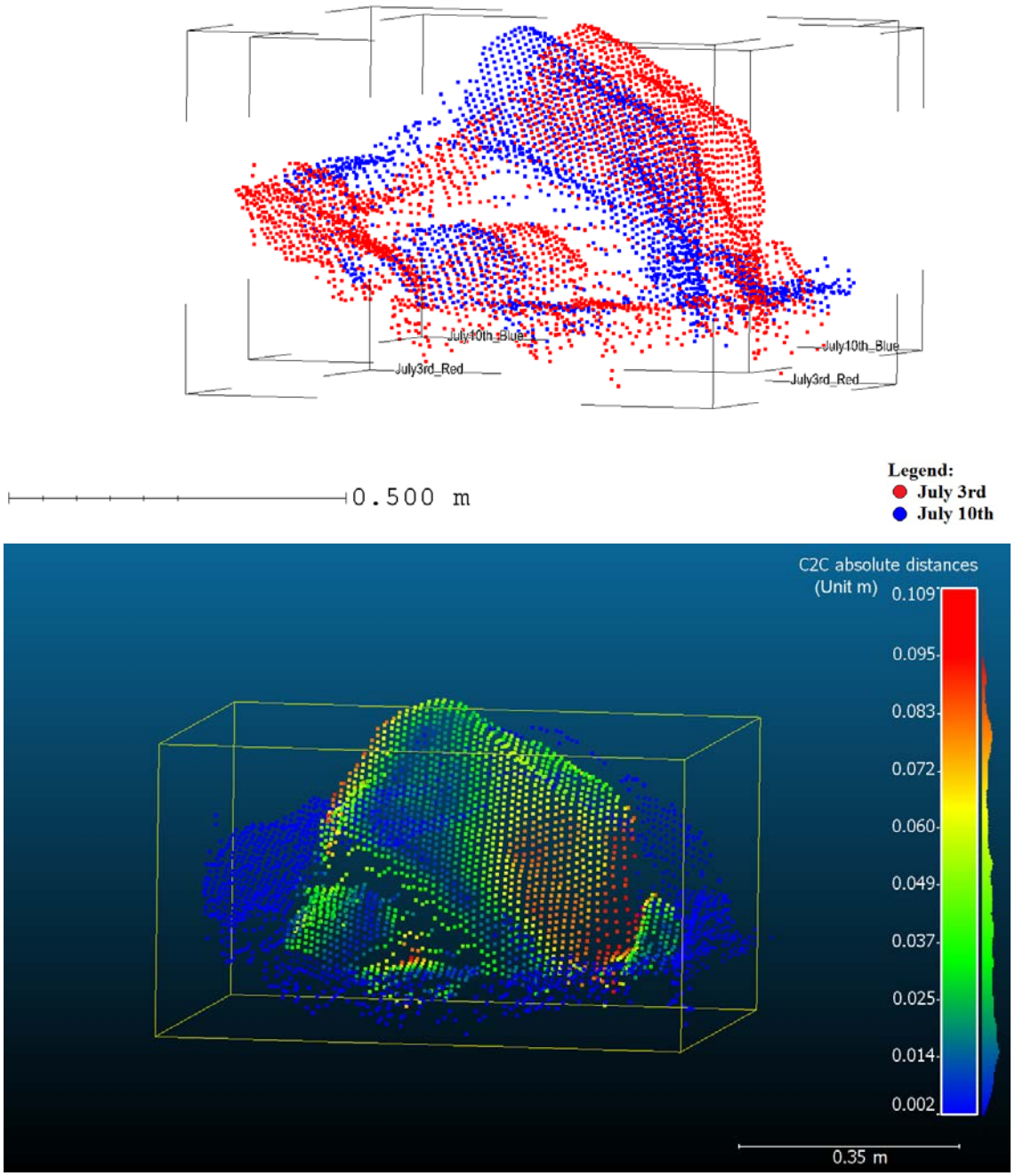

Figure 3-16 Coherent movement detected by C2C method. The top figure shows the point clouds being compared. The bottom figure shows C2C distances by color.

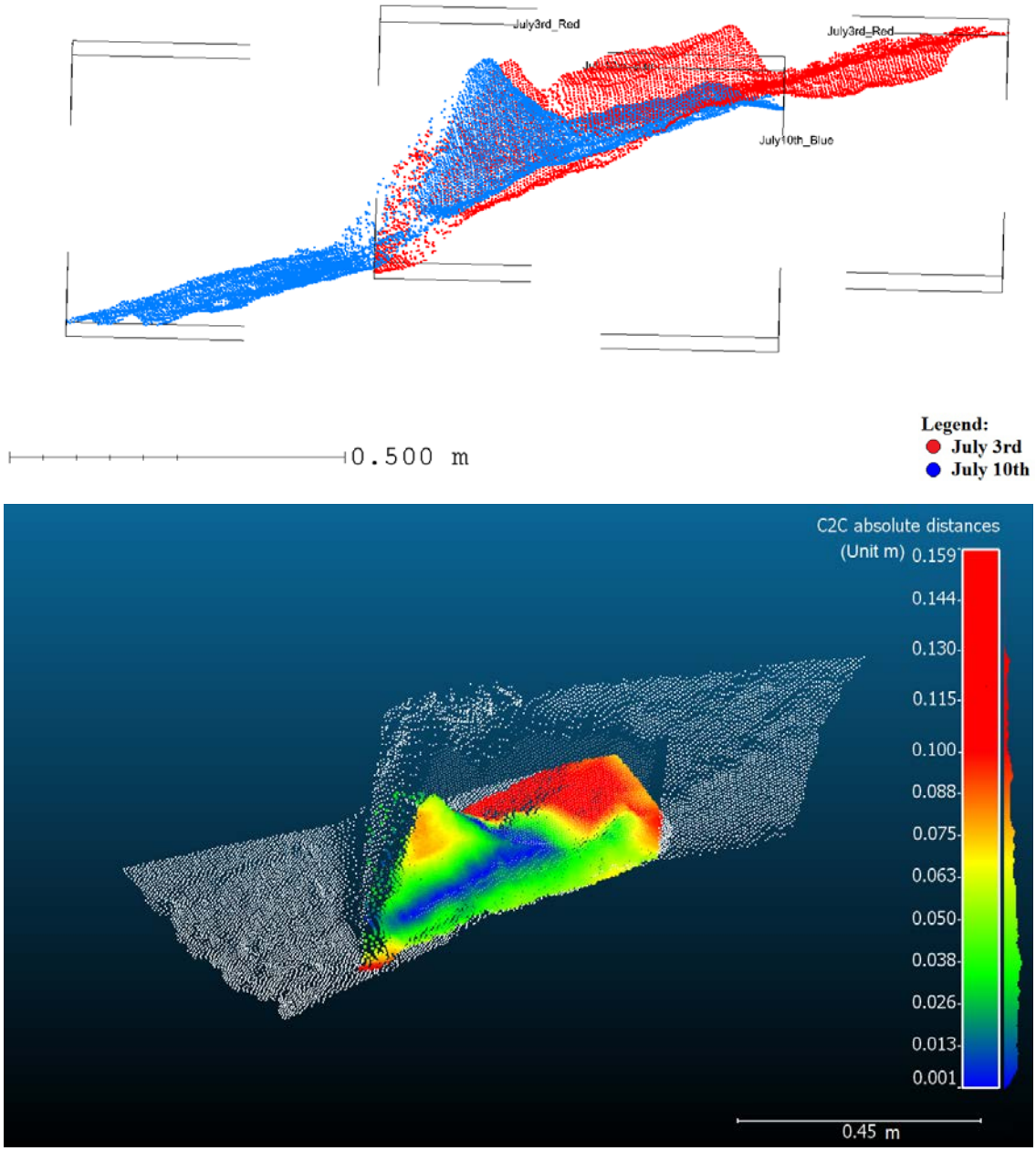

Figure 3-17 Collapse of the terrain detected by C2C method. The top figure shows the point clouds being compared. The bottom figure shows C2C distances by color.

4 Conclusion and Discussion

In this study, we demonstrated a method to identify slow landslide deformations using the integration of GPS, TLS, and ALS datasets. During one-week period from July 3rd to July 10th, 2015, we conducted an integrated GPS and LiDAR survey at the Slumgullion landslide, located near Lake City, Colorado. According to GPS measurements, the active part of the landslide moves at a rate of 1.47 cm per day horizontally. We found translational movements of the landslide with displacements ranging from 3 cm to 10 cm using TLS datasets.

This thesis consists of three parts. The first part introduced the background information about the study and the GPS and LiDAR integrated survey conducted at the Slumgullion landslide. The second part explained the workflow that we developed to generate high-resolution digital terrain models from TLS datasets. The third part analyzed the slow landslide movements recorded during the one-week survey.

The first part of the thesis introduced previous studies of the Slumgullion landslide area, the geological background of the landslide, and the one-week GPS and LiDAR integrated survey at the Slumgullion landslide. Positioning and ranging principles of GPS and LiDAR were introduced. The workflow for the GPS and TLS integrated field surveying was explained in detail and can be applied to study landslides in other regions.

The second part of the thesis developed a workflow for TLS data processing. TLS datasets were processed following the steps of data reduction, registration, filter, and gridding. An octree filter was applied to decimate raw laser points, and data volume was reduced by up to seventy percent after octree filter. A Deviation filter was introduced to remove the distorted laser measurements. The threshold for the deviation filter was explored; we

filtered data for deviation more than 30. Five registration methods were compared using the TLS dataset collected from the survey. Results showed that direct georeference registration was the worst registration method. Backsight and three-point registration yielded similar solutions, whereas freestation registration showed the most stable and reliable registration results. A terrain filter was applied to reveal the ground surface covered with dense vegetation. Unique water aliasing was found during the terrain filter of TLS datasets. The filtered point cloud was gridded with Kriging method. Final digital terrain models derived from TLS for the active part of the landslide, and ALS for the whole Slumgullion landslide area, are shown in Figure 2-19 and Figure 2-18.

The third part of this thesis analyzed the slow earth mass movement of the Slumgullion landslide during our one-week survey. Detected by GPS measurements, the average speed of the sliding movement was 1.47 cm per day horizontally. Different change detection strategies for the LiDAR point cloud measurements were compared. A coherent movement pattern was detected from the cloud-to-cloud comparison using TLS data. The lateral landslide motion detected from TLS ranged from 3 cm to 10 cm within our one-week survey. By comparing the topographic changes detected from GPS and LiDAR datasets, we conclude that the GPS unit is capable of tracing the corresponding location's movement in the landslide with centimeter accuracy. LiDAR had the advantage of detecting the movement pattern of the slow landslide process with a range of displacement, so there was a tradeoff between accuracy and the scale of detection. The integrated survey had the advantage of quantifying the slow landslide motion with both accurate point measurements and broad-scale pattern recognitions. It is expected that the results of this study will promote the application of GPS and LiDAR techniques in the practice of landslide hazard mitigation and landslide process studies.

Future work will be reoccupation the survey site at the Slumgullion landslide since one-week survey is far from enough to study the landslide mechanism. We demonstrated that GPS and LiDAR are a good combination for landslide surveying. Our integrated survey strategy can be used to delineate large area landslide process in detail.

References

Atwood, W. W., and Mather, K. F. (1932). Physiography and quaternary geology of the San Juan Mountains, Colorado. US Government Printing Office.

Board, American Society for Photogrammetry and Remote Sensing. (2008, September). LAS Specification Version 1.2. In ASPRS Board Meeting.

Buckley, S. J., Howell, J. A., Enge, H. D., and Kurz, T. H. (2008). Terrestrial laser scanning in geology: data acquisition, processing and accuracy considerations. Journal of the Geological Society, 165(3), 625-638.

Cao, N., Lee, H., Zaugg, E., Shrestha, R., Carter, W., Glennie, C., Wang, G., Lu, Z., and Diaz, J. (2017). Airborne DInSAR results using time-domain backprojection algorithm: a case study over the Slumgullion landslide in Colorado. Journal of Selected Topics in Applied Earth Observations and Remote Sensing. (Manuscript submitted for publication).

Chleborad, A. F., Diehl, S. F., and Cannon, S. H. (1996). Geotechnical Properties of Selected Materials from the Slumgullion Landslide. The Slumgullion Earth Flow: A Large-scale Natural Laboratory, 2130, 67.

CloudCompare (version 2.7.0) [GPL software]. (2017). Retrieved from http://www.cloudcompare.org/

Coe, J. A., Ellis, W. L., Godt, J. W., Savage, W. Z., Savage, J. E., Michael, J. A., Kibler, J.D., Powers, P.S., Lidke, D.J., and Dbray, S. (2003). Seasonal movement of the Slumgullion landslide determined from Global Positioning System surveys and field instrumentation, July 1998–March 2002. Engineering Geology, 68(1), 67-101.

Crandell, D.R., and Varnes, D.J. (1960). Slumgullion earthflow and earthslide near Lake City, Colorado. Geological Society of America Bulletin, v. 71, no. 12, pt. 2, p. 1846.

Crandell, D.R., and Varnes, D.J. (1961). Movement of the Slumgullion earthflow near Lake City, Colorado. Art. 57 in Short papers in the geologic and hydrologic sciences: U.S. Geological Survey Professional Paper 424-B, p. B136-B139.

Eckl, M. C., Snay, R. A., Soler, T., Cline, M. W., and Mader, G. L. (2001). Accuracy of GPS-derived relative positions as a function of interstation distance and observing-session duration. Journal of Geodesy, 75(12), 633-640.

Endlich, F.M. (1876). Report of F.M. Endlich. In: U.S. Geological and Geographical Survey (Hayden) of the Territories Annual Report 1874, 203 pp.

Fisher, P. F., and Tate, N. J. (2006). Causes and consequences of error in digital elevation models. Progress in Physical Geography, 30(4), 467-489.

Fleming, R. W., Baum, R. L., and Giardino, M. (1999). Map and description of the active part of the Slumgullion landslide, Hinsdale County, Colorado (p. 36). Denver: US Geological Survey.

Girardeau-Montaut, D. (2015). Cloud Compare version 2.6. 1-user manual. Online at: http://www. danielgm. net/cc/doc/qCC/CloudCompare% 20v2, 6, 20.

Girardeau-Montaut, D., Roux, M., Marc, R., and Thibault, G. (2005). Change detection on points cloud data acquired with a ground laser scanner. International Archives of Photogrammetry, Remote Sensing and Spatial Information Sciences, 36(part 3), W19.

Glenn, N. F., Streutker, D. R., Chadwick, D. J., Thackray, G. D., and Dorsch, S. J. (2006). Analysis of LiDAR-derived topographic information for characterizing and differentiating landslide morphology and activity. Geomorphology, 73(1), 131-148.

Hofmann, B., Lichtenegger, H., and Collins, J. (2001). GPS theory and practice. Springer Wien NewYork.

Jackson, M. E., Bodin, P. W., Savage, W. Z., and Nel, E. M. (1996). Measurement of local horizontal velocities on the Slumgullion landslide using the Global Positioning System. US Geol. Surv. Bull, 2130, 93-95.

Lague, D., Brodu, N., and Leroux, J. (2013). Accurate 3D comparison of complex topography with terrestrial laser scanner: Application to the Rangitikei canyon (NZ). ISPRS Journal of Photogrammetry and Remote Sensing, 82, 10-26.

Li, Z., Zhu, C., and Gold, C. (2004). Digital terrain modeling: principles and methodology. CRC press.

Lipman, P. W. (1976). Geologic map of the Lake City caldera area, western San Juan Mountains, southwestern Colorado (No. 962).

Lloyd, C. D., and Atkinson, P. M. (2002). Deriving DSMs from LiDAR data with kriging. International Journal of Remote Sensing, 23(12), 2519-2524.

Madole, R.F. (1996). Preliminary chronology of the Slumgullion landslide, Hinsdale County, Colorado. D.J. Varnes, W.Z. Savage (Eds.). The Slumgullion Earth Flow: A Large-Scale Natural Laboratory U.S. Geological Survey Bulletin, 2130, pp. 5–7.

Parise, M., and Guzzi, R. (1992). Volume and shape of the active and inactive parts of the Slumgullion landslide, Hinsdale County, Colorado (No. 92-216). US Geological Survey.

RIEGL Company. (2015). RiSCAN PRO manual, (Version 2.0.2). www.riegl.com

Savage, W. Z., and Fleming, R. W. (1996). Slumgullion landslide fault creep studies. The Slumgullion earth flow: a large-scale natural laboratory. US Geological Survey Bulletin, 2130, 73-76.

Shan, J., and Toth, C. K. (Eds.). (2008). Topographic laser ranging and scanning: principles and processing. CRC press.

Soler, T., and Wang, G. (2016). Interpreting OPUS-Static Results Accurately. Journal of Surveying Engineering, 142(4), 05016003.

Soler, T., Michalak, P., Weston, N. D., Snay, R. A., and Foote, R. H. (2006). Accuracy of OPUS solutions for 1-to 4-h observing sessions. GPS solutions, 10(1), 45-55.

Trimble. (2010). Trimble NetR9 GNSS Reference Receiver User Guide, Version 4.15.

Trimble. (2012). Trimble R10 GNSS receiver, Version 1.00.

Varnes, D. J., and Savage, W. Z. (Eds.). (1996). The Slumgullion earth flow: a large-scale natural laboratory (No. 2130-2132). US Government Printing Office.

Wang, G., and Soler, T. (2012). OPUS for horizontal subcentimeter-accuracy landslide monitoring: case study in the Puerto Rico and Virgin Islands region. Journal of Surveying Engineering, 138(3), 143-153.

Wang, G., Joyce, J., Phillips, D., Shrestha, R., and Carter, W. (2013). Delineating and defining the boundaries of an active landslide in the rainforest of Puerto Rico using a combination of airborne and terrestrial LiDAR data. Landslides, 10(4), 503-513.

Xiong, L., Wang, G., and Wessel, P. (2017). Anti-aliasing filters for deriving high-accuracy DEMs from TLS data: A case study from Freeport, Texas. Computers & Geosciences, 100, 125-134.

Zhou, X., Wang, G., Bao, Y., Xiong, L., Guzman, V., and Kearns, T. J., (2017). Delineating Beach and Dune Morphology from Massive Terrestrial Laser Scanning Data Using the Generic Mapping Tools. Journal of Survey Engineering. (Manuscript submitted for publication).

Appendix I: A standard OPUS report.

```
From:    opus <opus@ngs.noaa.gov>
Sent:    Thursday, January 21, 2016 11:26 AM
To:      User's email address
Subject:         OPUS solution : BA.15O OP1453396949221

 FILE: BA.15O OP1453396949221

 1008   NOTE:  Antenna offsets supplied by the user were <=0.  Coordinates
 1008   returned will be for the antenna reference point (ARP).
 1008
                              NGS OPUS SOLUTION REPORT
                              ========================

All computed coordinate accuracies are listed as peak-to-peak values.
For additional information: http://www.ngs.noaa.gov/OPUS/about.jsp#accuracy

      USER: User's email address                      DATE: January 21, 2016
RINEX FILE: BA.15o                                    TIME: 17:25:20 UTC


  SOFTWARE: page5  1209.04 master52.pl 022814      START: 2015/07/10  12:46:00
 EPHEMERIS: igs18525.eph [precise]                  STOP: 2015/07/10  23:22:00
  NAV FILE: BA.15n                           OBS USED: 26600 / 28028   :  95%
  ANT NAME: TRM57971.00     NONE             # FIXED AMB:   112 /   126   :  89%
ARP HEIGHT: 0.000                            OVERALL RMS: 0.016(m)


 REF FRAME: NAD_83(2011)(EPOCH:2010.0000)              IGS08 (EPOCH:2015.5226)

         X:     -1493755.396(m)   0.011(m)          -1493756.233(m)   0.011(m)
         Y:     -4808871.037(m)   0.026(m)          -4808869.707(m)   0.026(m)
         Z:      3906596.616(m)   0.022(m)           3906596.505(m)   0.022(m)

       LAT:   37 59 27.59367      0.012(m)        37 59 27.61122      0.012(m)
     E LON:  252 44 38.04425      0.003(m)       252 44 37.99535      0.003(m)
     W LON:  107 15 21.95575      0.003(m)       107 15 22.00465      0.003(m)
    EL HGT:          3151.793(m)   0.034(m)              3150.919(m)   0.034(m)
 ORTHO HGT:          3166.781(m)   0.063(m) [NAVD88 (Computed using GEOID12B)]

                         UTM COORDINATES    STATE PLANE COORDINATES
                          UTM (Zone 13)         SPC (0503 CO S)
Northing (Y) [meters]     4207217.891           453230.817
Easting (X)  [meters]      301883.817           760157.429
Convergence  [degrees]    -1.38916532          -1.07715246
Point Scale                1.00008344           0.99994913
Combined Factor            0.99958908           0.99945484

US NATIONAL GRID DESIGNATOR: 13SCC0188307217(NAD 83)


                              BASE STATIONS USED
PID       DESIGNATION                        LATITUDE    LONGITUDE DISTANCE(m)
DO2634 CTI4 COMPASSTOOLS4CRNR CORS ARP     N370910.489 W1074521.876  103017.9
DL3478 R301 CRAWFORD CORS ARP              N383923.739 W1073527.367   79512.8
DL3642 MC09 NUCLA CORS ARP                 N381435.614 W1083329.283  117611.8

                    NEAREST NGS PUBLISHED CONTROL POINT
HL0318      F 169                          N375929.0   W1071426.1      1361.9

This position and the above vector components were computed without any
knowledge by the National Geodetic Survey regarding the equipment or
field operating procedures used.
```

Appendix II: VBA script for extracting information from OPUS reports.

```
Sub finddata()

'1.declare varaiables
'Dim Northing As String
'string is test, integer is a number
Dim finalrow As Integer
'Last row of data, where to stop

Dim i As Integer
'variable

finalrow = Sheets("All_uhjf").Range("A50000").End(xlUp).Row

'2. clear old search results
Sheets("All_uhjf").Range("Q1:V1000").ClearContents


'3.find records that match criteria and pasete them
For i = 1 To finalrow
    If Cells(i, 1) = "Northing" Then
        Cells(i, 4).Copy
        Range("S1000").End(xlUp).Offset(1, 0).PasteSpecial xlPasteFormulasAndNumberFormats
        Cells(i + 1, 4).Copy
        Range("R1000").End(xlUp).Offset(1, 0).PasteSpecial xlPasteFormulasAndNumberFormats
        Cells(i - 5, 4).Copy
        Range("T1000").End(xlUp).Offset(1, 0).PasteSpecial xlPasteFormulasAndNumberFormats
        Cells(i - 4, 4).Copy
        Range("U1000").End(xlUp).Offset(1, 0).PasteSpecial xlPasteFormulasAndNumberFormats
        Cells(i - 21, 8).Copy
        Range("Q1000").End(xlUp).Offset(1, 0).PasteSpecial xlPasteFormulasAndNumberFormats
        Cells(i, 5).Copy
        Range("W1000").End(xlUp).Offset(1, 0).PasteSpecial xlPasteFormulasAndNumberFormats
        Cells(i + 1, 5).Copy
        Range("V1000").End(xlUp).Offset(1, 0).PasteSpecial xlPasteFormulasAndNumberFormats

        End If
Next i

Range("Q1") = "Date"
Range("R1") = "X"
Range("S1") = "Y"
Range("T1") = "EL"
Range("U1") = "OH"
Range("V1") = "X"
Range("W1") = "Y"

End Sub
```